ABSTRACT

MOLECULAR MECHANISMS OF AMYLOID-LIKE FIBRIL FORMATION

by
Sharareh Jalali

Proteins play a critical role in living systems by performing most of the functions inside cells. The latter is determined by the protein's three-dimensional structure when it is folded in its native state. However, under pathological conditions, proteins can misfold and aggregate, accounting for the formation of highly ordered insoluble assemblies known as amyloid fibrils. These assemblies are associated with diseases like Parkinson's and Alzheimer's. Strong evidence suggests that three mechanisms are critical for forming amyloid fibrils. These mechanisms are the nucleation of amyloid fibrils in solution (primary nucleation) as well as on the surface of existing fibrils (secondary nucleation) and the elongation of fibrils. This dissertation aims to provide insights into the complex mechanisms underlying the formation of amyloid-like fibrils at the atomic level, which remains poorly understood. This knowledge will enable the rational design of drugs to treat diseases.

This dissertation is divided into three parts. First, extensive molecular dynamics simulations are performed to show that all-atom models can account for the aggregation of peptides into amyloid-like fibrils. These simulations are conducted using different amino acid sequences at different temperatures. They highlight the importance of hydrophobic interactions in aggregation. This is supported by an increase in the rate of fibril formation with increasing temperature, which is a characteristic behavior of hydrophobic interactions. Moreover, the effect of NaCl on the aggregation of sequences made with non-polar residues that exhibit a low degree of hydrophobicity is investigated. Results provide evidence that screening electrostatic interactions with salts promotes aggregation. Furthermore, the results of this study

demonstrate that peptides made from the same amino acids located at different positions in the sequence form fibrils with different propensity. An analysis of these systems indicates that the propensity to form fibrils in-vitro correlates positively with the propensity to form fibrils in-silico when long simulations (2-3 μs) are conducted.

Second, all-atom simulations are performed to provide new insights into the kinetics of fibril growth and the role played by the fibril surface in this phenomena. Results of this study show that peptides can land on the fibril tip via two pathways: bulk-docking and surface-docking. In bulk-docking, the peptide binds from the bulk solution directly to the tip to elongate the fibril. In the surface-docking, the peptide lands and diffuses on the fibril surface to reach the tip. Peptides are usually assumed to populate the fibril tip via bulk-docking. However, simulation results show that surface-docking can contribute significantly to this phenomena. In particular, changing the temperature and aspect ratio of the fibril affects the relative contribution of these two docking pathways. A continuum model is proposed by collaborators to quantify the effect of fibril surface, length, and temperature in bulk- and surface-docking.

Third, all-atom simulations are performed to provide insights into primary nucleation. An intermediate state is observed to form spontaneously on the pathway to fibril formation, which is made of two laminated β-sheets with peptides oriented perpendicularly to each other. This state remains stable for ~ 0.5 μs after which β-sheets rotate to account for the spine of amyloid fibrils where peptides are aligned with each other. This study also emphasizes the importance of side chain interactions in aligning docked peptides with the fibril template. Docked peptides get trapped in local minima when conformational changes are not driven by side chain interactions at high temperatures. The role played by non-polar patches on the fibril surface in secondary nucleation is also discussed.

MOLECULAR MECHANISMS OF AMYLOID-LIKE FIBRIL FORMATION

by
Sharareh Jalali

A Dissertation
Submitted to the Faculty of
New Jersey Institute of Technology
in Fulfillment of the Requirements for the Degree of
Doctor of Philosophy in Applied Physics

Department of Physics

August 2023

APPROVAL PAGE

MOLECULAR MECHANISMS OF AMYLOID-LIKE FIBRIL FORMATION

Sharareh Jalali

Dr. Cristiano L. Dias, Dissertation Advisor — Date
Associate Professor of Physics, NJIT

Dr. Wenda Cao, Committee Member — Date
Professor of Physics, NJIT

Dr. Keun Hyuk Ahn, Committee Member — Date
Associate Professor of Physics, NJIT

Dr. Junjie Yang, Committee Member — Date
Assistant Professor of Physics, NJIT

Dr. Yuanwei Zhang, Committee Member — Date
Assistant Professor of Chemistry and Environmental Science, NJIT

Dr. Treena Arinzeh, Committee Member — Date
Professor of Biomedical Engineering, Columbia University, New York, NY

Dr. Bradley L. Nilsson, Committee Member — Date
Professor of Chemistry, University of Rochester, Rochester, NY

BIOGRAPHICAL SKETCH

Author: Sharareh Jalali

Degree: Doctor of Philosophy

Date: August 2023

Undergraduate and Graduate Education:

- Doctor of Philosophy in Applied Physics,
  New Jersey Institute of Technology, Newark, NJ, 2023
- Master of Science in Biomedical Engineering,
  AmirKabir University of Technology (Tehran Polytechnic), Tehran, Iran, 2013
- Bachelor of Science in Biomedical Engineering,
  AmirKabir University of Technology (Tehran Polytechnic), Tehran, Iran, 2010

Major: Applied Physics

Presentations and Publications:

S. Jalali, Y. Yang, F. Mahmoudinobar, S M. Singh, B. L Nilsson, C. L. Dias, "Using all-atom simulations in explicit solvent to study aggregation of amphipathic peptides into amyloid-like fibrils," *Journal of Molecular Liquids* Vol.347, Number 118283, 2022.

Y. Yang, H. Distaffen, S. Jalali, A. J. Nieuwkoop, B. L. Nilsson, C. L. Dias, "Atomic insights into amyloid-induced membrane damage," *American Chemical Society Chemical Neuroscience* Vol.13, pp 2766-2777, 2022.

Y. Yang, S. Jalali, B. L. Nilsson, and C. L. Dias,"Binding mechanisms of amyloid-like peptides to lipid bilayers and effects of divalent cations," *American Chemical Society Chemical Neuroscience*, Vol.12, pp 2027-2035, 2021.

C. L. Dias, S. Jalali, Y. Yang and L. Cruz, "Role of cholesterol on binding of amyloid fibrils to lipid bilayers," *Journal of Physical Chemistry B*, vol.124, pp 3036-3042, 2020.

S. Jalali, M. Tafazzoli-Shadpour, N. Haghighipour, R. Omidvar, F. Safshekan, "Regulation of endothelial cell adherence and elastic modulus by substrate stiffness," *Cell Communication Adhesion*, vol. 22, pp.79-89., 2016.

S. Jalali, C. L. Dias,"Atomic insights into fibril elongation: beyond dock-and-lock mechanisms," *Oral presentation, American Physical Society March Meeting*, Las Vegas, Nevada, USA, 2023.

S. Jalali, Y. Yang, F. Mahmoudinobar, C. L. Dias, "Protein aggregation and self-assembly into amyloid-like fibrils," *Oral presentation, Aerican Physical Society March Meeting*, Chicago, Illinois, USA, 2022.

S. Jalali, C.L. Dias,"Using large-scale and long-time all-atom simulations to study the aggregation of amphipathic peptides into amyloid-like fibrils," *35th Gibbs Conference on Biological Thermodynamics, Online*, 2021.

S. Jalali, Y. Yang, F. Mahmoudinobar, S. M. Singh and C. L. Dias,"Protein aggregation and self-assembly into amyloid-like fibrils," *American Physical Society-Mid-Atlantic Section Fall Meeting 2020, Online*, 2020.

This dissertation is dedicated to the love of my life and soulmate, Farbod, my incredible parents Soosan and Parviz, and my beloved sister, Shahrzad.

ACKNOWLEDGMENTS

I would like to thank all the individuals who supported me during this exciting journey.

First and foremost, I would like to express my deepest appreciation to my advisor, Prof. Cristiano Dias for his constant support, encouragement, and guidance throughout this journey. Without your suggestions and expertise, I would not have been able to complete this research. Thank you for providing fantastic opportunities and exciting projects for me. You helped me to become a problem solver, a dedicated researcher, and passionate about science.

I would like to extend a huge thank to my committee members: Prof. Wenda Cao, Prof. Treena Arinzeh, Prof. Bradley Nilsson, Prof. Keun H. Ahn, Prof. Junjie Yang, and Prof. Yuanwei Zhang for taking time and effort to serve as my committee members and provide insightful comments.

I would like to express my appreciation to our collaborates, Prof. Bradley Nilsson, Chris Jones and Hannah Distaffen from University of Rochester and Prof. Shaneen Singh from City University of New York for providing the opportunities for scientific discussions. Through these invaluable collaborations, I have been presented with extensive opportunities to expand my knowledge and expertise.

I am deeply grateful to our collaborators Prof. Mikko Hattaja and Ruoyao Zhang from Princeton University, whose invaluable contributions and support greatly enriched the outcome of the projects in Chapters 3 and 4 of this dissertation.

I would like to thank Physics Department, Mrs. Christine Oertel, Prof. Bin Chen and Prof. Haimin Wang for assisting and guiding me through my academic path and Dr. Sung Maeng for all his supports and opportunities to give me to be a better teaching assistant (TA) and have a chance to experience teaching physics labs to undergraduate students.

The work in Chapter 2 of this dissertation is originally published in the Journal of Molecular Liquids and was supported by the National Science Foundation under Grant Nos. CHE-1904364 and CHE-1904528. Computational resources were provided by Academic and Research Computing Systems (ARCS) at the New Jersey Institute of Technology and by the Pittsburgh Supercomputing Center (PSC). Anton 2 at PSC is supported by the National Institute of General Medical Sciences of the National Institute of Health under Award Number R01GM116961. The Anton 2 machine at PSC was generously made available by D.E. Shaw Research.

Molecular dynamics simulations in Chapter 3 are performed by Sharareh Jalali and prof. Cristiano Dias supported by the National Institute of General Medical Health under Grant No. 1R15GM148982-01. A mesoscale continuum model is proposed by Ruoyao Zhang and prof. Mikko P. Hattaja to quantify the effect of fibril surface, length and temperature in bulk- and surface-docking supported by the National Science Foundation (NSF) Materials Research Science and Engineering Center Program through the Princeton Center for Complex Materials (PCCM) (DMR-2011750). Both Ruoyao Zhang and Sharareh Jalali have equal contributions.

In Chapter 4, Sharareh Jalali and prof. Cristiano Dias were supported by the National Institute of General Medical Health under Grant No. 1R15GM148982-01 and computational resources were provided by the Academic and Research Computing System (ARCS) at New Jersey Institute of Technology. Ruoyao Zhang and prof. Mikko P. Hattaja were supported by the National Science Foundation (NSF) Materials Research Science and Engineering Center Program through the Princeton Center for Complex Materials (PCCM) (DMR-2011750).

I would like to thank Yanxing Yang and Warin Rangubpit, my labmates who make the office fun for me and for all the scientific discussions we had in the lab.

Last but not least, I would like to thank my husband, Farbod, whose unwavering love and support have been my constant source of strength. I am deeply grateful to my

beloved parents Soosan and Parviz, whose support and encouragement have shaped me into who I am today. Moreover, I am thankful to my sister, Shahrzad, for her constant support and encouragement throughout my journey. I am also very grateful for my wonderful in-laws Laleh, Behzad, and my brother in law, Farzad. Your love and support have been a constant source of inspiration. I am very thankful to have such a wonderful family and friends by my side.

TABLE OF CONTENTS

TABLE OF CONTENTS
(Continued)

Chapter **Page**

LIST OF TABLES

Table **Page**

LIST OF FIGURES

Figure **Page**

LIST OF FIGURES
(Continued)

Figure **Page**

Figure **Page**

LIST OF FIGURES
(Continued)

Figure **Page**

LIST OF FIGURES
(Continued)

Figure **Page**

LIST OF FIGURES
(Continued)

Figure **Page**

LIST OF FIGURES
(Continued)

Figure **Page**

LIST OF FIGURES
(Continued)

Figure **Page**

LIST OF FIGURES
(Continued)

Figure **Page**

CHAPTER 1

INTRODUCTION

Under various solvent conditions, soluble proteins and peptides can misfold and aggregate to form highly ordered insoluble assemblies, i.e., amyloid fibrils. The latter can grow for several micrometers in length while preserving the structure of its tips with atomic fidelity. This phenomenon, which determines the fate of almost all amyloid proteins/peptides in diseases like Alzheimer's, remains unclear [5, 6, 7, 8]. Currently, the microscopic mechanisms accounting for fibril nucleation remains also unclear. In this dissertation, we study the aggregation of peptides and the structural transitions accounting for amyloid-like fibril formation with a short amphipathic peptide as a model of amyloid protein using all-atom molecular dynamics simulations. This study addresses important fundamental questions related to the forces driving the nucleation and growth of amyloid-like fibrils. For example, we investigate how the kinetic of fibril growth is affected by external conditions like temperature and the presence of salt. Also, we provide insights into how the fibril nucleus is catalyzed at the surface of existing fibrils in solution.

This dissertation is organized into five chapters and includes the following elements. In Chapter 1, we provide an introduction to amino acids, proteins, fibril formation, and molecular dynamics simulations. Chapter 2 develops the computational framework to study the spontaneous aggregation of amphipathic peptides into amyloid-like fibrils. This framework is then used in Chapter 3 to study different pathways by which peptides dock onto the fibril tip accounting for growth. The role of the fibril surface and temperature are also investigated in this study. Chapter 4 provides insights into the nucleation of the cross-β structures in the

bulk solution, on the surface of the existing fibril, and fibril growth mechanisms. In Chapter 5, we conclude our research and propose new ideas for future direction.

1.1 Amino Acids Structures and Protein

Amino acids are essential biomolecules that comprise proteins. They have a central carbon atom, i.e. , Cα, which is attached to a carboxyl group (COOH), an amino group (NH_2), a hydrogen atom (H), and a side chain (R) – see Figure 1.1. Amino acids are distinguished by their side chain, which gives each one unique properties. Moreover, all amino acids have a chiral carbon atom (C_α) giving rise to L- and D-form, reflecting left and right-handed chemical structures as shown in Figure 1.1a-b [9, 10, 11, 12, 13].

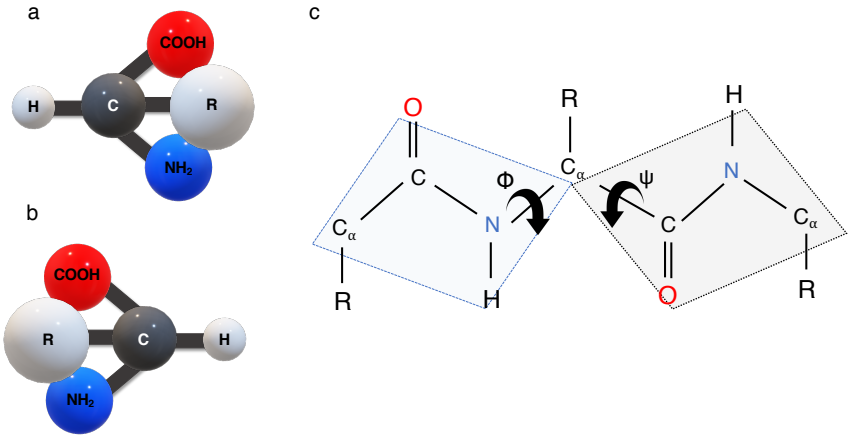

Figure 1.1 Schematic representation of amino acid structure. (a) Left handed amino-acid, (b) right handed amino-acid, and (c) torsion angle between N-Cα bond (ϕ) and Cα -C bond (ψ).

Amino acids are attached to each other via a peptide bond and form proteins, which perform almost every biochemical function in living cells, including metabolism, particle transportation, information processing, and many more. The sequence of amino acids in a protein is called primary structure, which defines its three-dimensional shape.

The primary structure is the first hierarchy level in protein structure and is its linear amino acid sequence. Protein's secondary structure is referred to local conformations of the protein backbone such as α-helices and β-sheets. The latter constitutes the most relevant secondary structure for fibril formation. In particular, β-strands occur when the protein chain is extended completely. Several β-strands can be linked to each other by backbone hydrogen bonds and form β-sheets. The β-strands in a β-sheet can be either parallel or anti-parallel, depending on the direction of protein sequence – see Figure 1.2. If they have the same orientation for N-terminus to C-terminus they form a parallel sheet and if they have the opposite orientation (C-terminus of one strand is close to N-terminus of the other strand), it is called an anti-parallel β-sheet [14, 15].

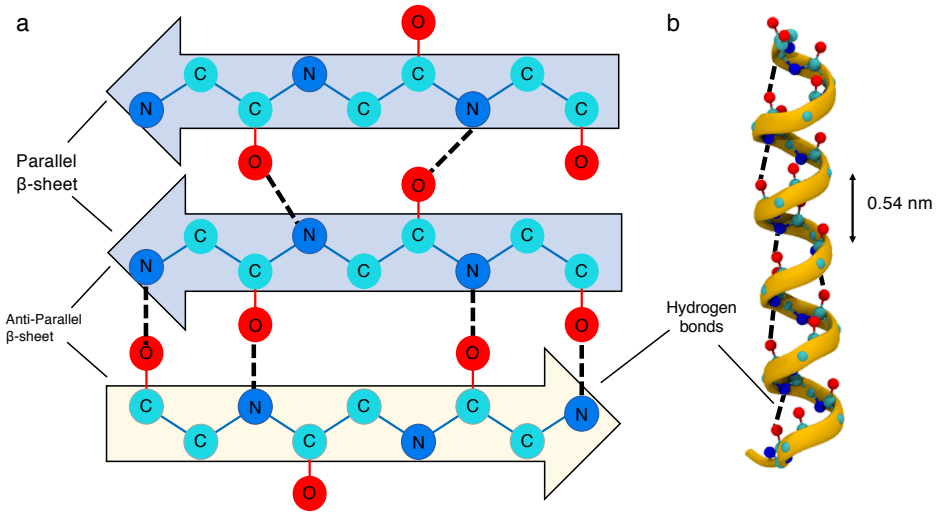

Figure 1.2 Two major types of secondary structures in proteins. (a) β-sheet consisting of β-strands pointing to the same direction (parallel), and β-strands pointing to the opposite direction (anti-parallel). Hydrogen bonds form between oxygen (O) in carboxyl group of one residue and hydrogen (H) of amino group of the other residue. Red, blue and cyan colors are used to represent oxygen, nitrogen and carbon atom. (b) α-helix with the pitch of 5.4 Åand hydrogen bond formation. The structure is obtained from Protein Data Bank (1cdw).

1.2 Biochemical Bonds

Biochemistry is the science that provides insight into the chemistry between living organisms. To explore and better understand the living organisms, we need to know what are the interactions that keep atoms of proteins together as a molecule or how different groups of molecules interact with each other. Biochemical bonds are classified into two major groups: covalent, and non-covalent bonds. Covalent bonds keep atoms of a molecule together and are formed when two atoms share electrons. For example, the two carbons in the backbone of an amino acid, form a covalent bond with a distance of 1.54 Å and bond energy of 85 (kcal/mol). The second type of biochemical bonding is a non-covalent bond. Although they are weaker than covalent bonds, they play a significant role in all biological structures and functions. Non-covalent bonds are separated into four types of bonds and interactions: hydrogen bonds, electrostatic interactions, van der Waals interactions, and hydrophobic interactions [16, 1].

Hydrogen Bonds: Hydrogen bonds are weak in terms of energy , but they play a crucial role in many biological functions and stabilizing proteins. For example, the energy of hydrogen bonds between water molecules can vary from 20 to 42 (kJ/mol) [17]. As shown in Figure 1.3 when a hydrogen atom is shared between two electronegative atoms, especially nitrogen or oxygen, the one linked with the covalent bond to the hydrogen (donor) pulls the electron of the hydrogen atom toward itself and becomes partially negative. As a result, the hydrogen atom becomes partially positive which forms a dipole-dipole attraction between hydrogen atom bonded to the donor and the lone electron pair in the other electronegative atom (acceptor). This results in a hydrogen bond [18].

Intra-peptide hydrogen bonds take place between atoms of the same peptide, while inter-peptide hydrogen bonds form between different peptides. The hydrogen bond length, i.e., the distance between two non-hydrogen atoms involved in a hydrogen bond, is approximately 2.4-3.5 Å [16].

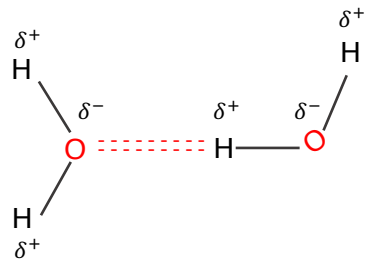

Figure 1.3 Hydrogen bond between two water molecules. The Hydrogen atom, i.e., H, of one molecule is shared among the two Oxygen atoms, i.e., O, in the same molecule and another water molecule [1].

Electrostatic Interaction: The attraction and repulsion between two charged atoms is known as electrostatic (or Coulomb) interaction, and its energy is calculated based on Coulomb's law (Equation (1.1)). This energy is directly proportional to the magnitude of each charge and reversely proportional to the distance between the two atoms.

$$E = \frac{1}{4\pi\epsilon_0}\frac{q_1 q_2}{r} \tag{1.1}$$

where q_1 and q_2 are the charges of the first and second atoms respectively, ϵ_0 is permittivity of vacuum, and r is the distance between two atoms.

Van der Waals interaction: Another weak non-covalent bond is the van der Waals interaction which depends upon the distance between atoms. This force originates when two atoms move toward one another, and a fluctuation takes place in their polarization. As a result, a dipole interaction arises between neighboring atoms. This type of interaction varies from attraction, when two atoms are far from each other, to strong repulsion when atoms are in close proximity. Finally, it stabilizes at a specific distance called the equilibrium distance [16, 19, 1].

Hydrophobic Interaction: Another non-covalent interaction that is important in protein folding and mostly emerges from interaction of proteins with water molecules is hydrophobic interaction. When proteins unfold, their non-polar

residues become exposed to water, push water molecules away from protein and cause water molecules to form ordered structures with lower entropy. However, when proteins fold, non-polar residues become buried away from water. As a result, water molecules have more freedom to interact with polar residues of the protein and become more disordered and thus have higher entropy. This entropic effect of water molecules accounts for a net attraction between non-polar molecules and is known as hydrophobic effect. This non-covalent interaction is thermodynamically favorable and contributes to folding of many proteins [20, 1]. Figure 1.4 shows the formation of the hydrogen bonds around a single molecule and when non-polar residues aggregate.

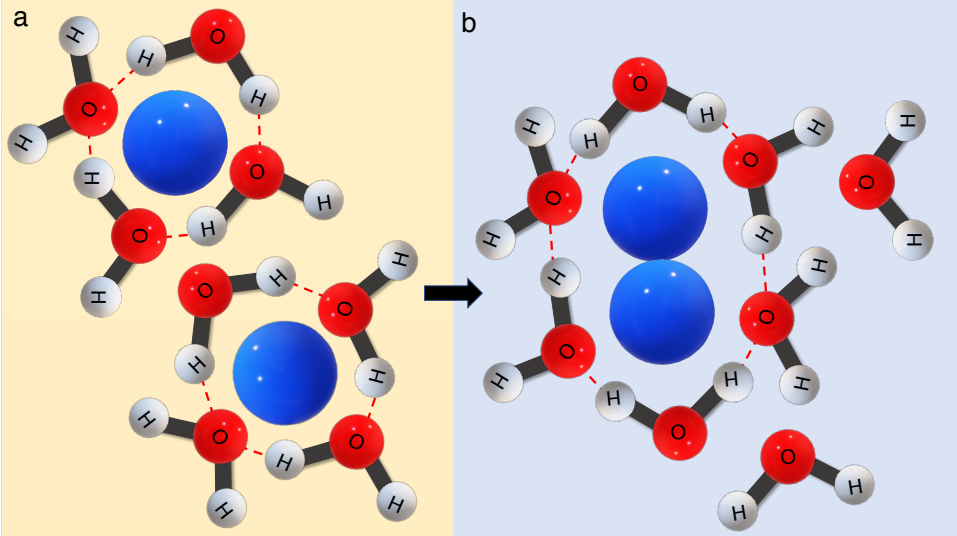

Figure 1.4 Hydrogen bonds form between water molecules around non-polar residues for (a) single molecules interact with water molecules and (b) the interaction between water molecules and two molecules when aggregating. The red bonds represent the formation of hydrogen bonds.

1.3 Formation of Cross β-structures

Prior studies have shown that under specific circumstances, soluble proteins misfold and form insoluble aggregates. These protein aggregates can undergo further structural reorganization and form amyloid fibrils consisting of β-sheets stacked on top of each other which is known as cross-β structure. Such fibrils are observed

extensively in protein misfolding diseases and neurodegenerative conditions including Alzheimer's [21, 22].

The cross-β structure was reported for the first time from X-ray diffraction pattern of stretched poached egg whites proteins in 1935. In that study, he proposed a general molecular arrangement for fibrous, wherein the strands pointed in the same direction and elongated along the fibril axis [23, 21, 24]. In 1951, Pauling and Corey discovered the pleated β-sheet motif arrangement. They found that the hydrogen bonds between the β-strands account for connecting the β-strands and formation of β-sheet [25]. Following this, in 1968, cross-β structures were determined by X-ray diffraction, revealing the atomic details, including an intense ring at 4.75 $\mathring{A}$ overlaying a diffuse halo at 4.3 $\mathring{A}$, and a less intense perpendicular ring at 9.8 $\mathring{A}$ and pleated β-sheet was reported [26]. Advancement of experimental methods, including cryo-electron microscopy (cryo-EM) and solid state Nuclear Magnetic Resonance (NMR) has led to a better understanding of the molecular structure of amyloid fibril cross-β structures.[27, 28, 21, 29].

Cross-β structures of amyloid fibrils were characterized by X-ray diffraction represents the space between two strands, i.e., interstrand space, (4.8 Å) and between the two sheets ($\sim$ 10Å) [21, 22]. These cross-β spines are made from two identical β-sheets. These steric zipper protofilaments can be classified into eight distinct classes [21]. Subsequently, these classes can be divided into two groups based on the arrangement of the strands, i.e., parallel, i.e., or anti-parallel. The orientation of their faces and the strands can determine their classes. For example, they can be face to face, faces to the back, both sheets face up, or one of them face up while the other one face down [21, 30, 31]. The pre-formed fibril studied in Chapters 3 and 4 of this dissertation form anti-parallel β-sheets that pack against each other in class 5 of the Eisenberg classification scheme.

In experimental studies, the kinetics of fibril formation can be monitored using a sigmoidal shape profile corresponding to an increase in fibril mass as shown schematically in Figure 1.5. The process is divided into three phases: lag, growth, and stationary. The lag phase refers to the slow process where the monomers are mostly soluble (no fibril is present), and only initial nucleation of the monomers in the solution emerges, i.e., primary nucleation. Subsequently, after the formation of the nucleus, the fibril mass is detectable, and it can be elongated by adding the monomer at the end of the fibril, i.e., the growth phase. Secondary nucleation, in which a new nucleus emerges on the surface of existing fibrils, may also take place in this phase. Finally, the mature fibril forms in the stationary phase, and the fibril and monomers are in equilibrium [32, 33]. Understanding these three mechanisms accounting for amyloid fibril formation at the atomic level is critical to provide insights into the rational for developing strategies to treat neurodegenerative diseases [34, 35, 36] but also plays a significant role in designing new peptide-based materials that can be used in biomedical applications, e.g., in tissue engineering, matrices for cell adhesion, and anti-cancer drugs with high loading drug capacity [37, 38, 39, 40, 41, 42, 43, 44, 45, 46]. Insights from in-silico simulations provide invaluable information to understand underlying atomic interactions of nucleation, which are beyond the reach of experiments due to their short time scales and length scales involved in the process [47, 48].

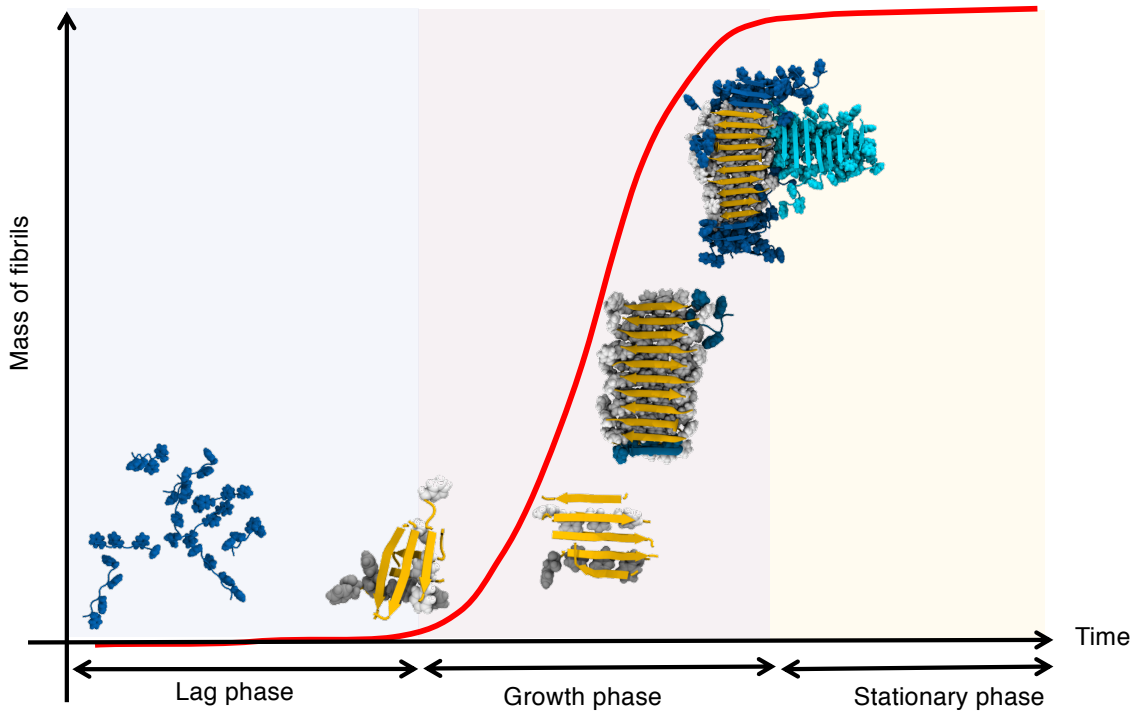

Figure 1.5 Schematic representation of three phases involved in amyloid fibril formation: lag, growth, and stationary.

1.4 Methodology

In this dissertation, we use MD simulations to provide insight into peptide-peptide interactions accounting for spontaneous aggregation of short peptides into amyloid-like fibrils, nucleation and fibril growth. We are going to perform long, unbiased simulations to generate trajectories with details at atomic level under different conditions.

1.4.1 Molecular dynamics simulation

One of the powerful techniques for understanding the details and dynamics of biological macromolecules is molecular dynamics (MD) simulations. It can obtain details at the atomic level and provide insight into interactions between atoms, which is experimentally not easy to obtain. First, it will read the initial coordinates of atoms and boundary conditions of a system with N particles. Second, it will randomly assign the initial velocities to atoms. Third, it computes forces acting on atoms from

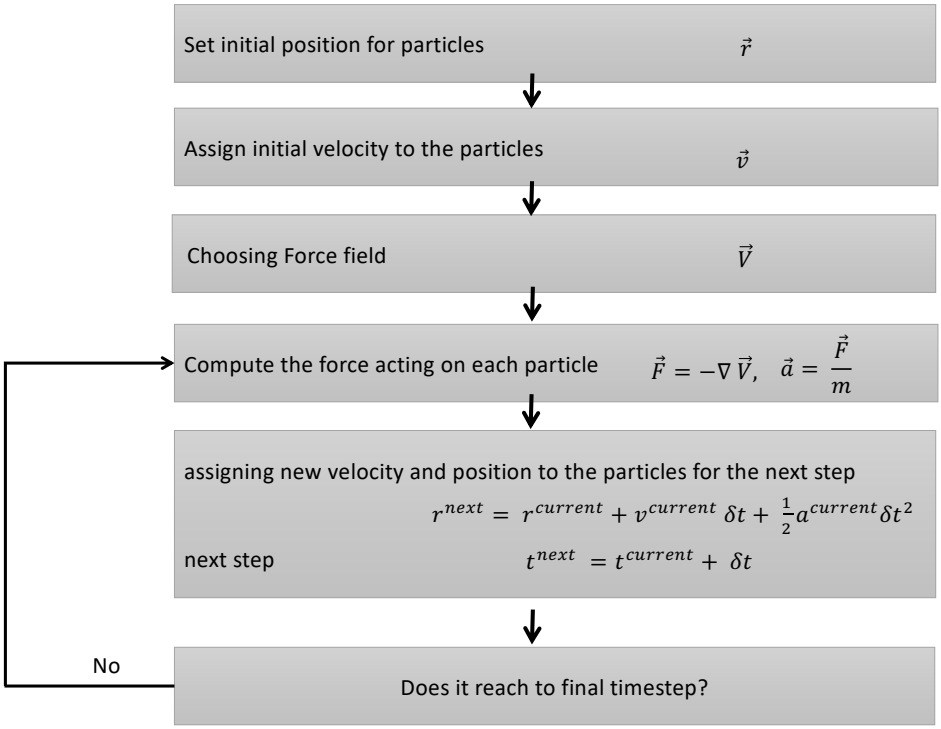

Figure 1.6 Flow chart represents the steps for molecular dynamics.

specific inter-atomic potential energy and finally, by integrating Newton's equation of the motion, accelerations, velocities, and final atoms coordinates are calculated. It will update the coordinates of atoms. The flow chart indicating these steps is shown in Figure 1.6 [49, 50].

Verlet algorithm One of the most common numerical method to integrate Newton's equation of motion in MD simulations is known verlet algorythm. In this method, Taylor expansion of r(t) is used as below:

$$r(t + \Delta t) = r(t) + v(t)\Delta t + \frac{1}{2}a(t)\Delta t^2 + \frac{1}{6}c(t)\Delta t^3 + ... \tag{1.2}$$

$$r(t - \Delta t) = r(t) - v(t)\Delta t + \frac{1}{2}a(t)\Delta t^2 - \frac{1}{6}c(t)\Delta t^3 + ... \tag{1.3}$$

by adding Equations (1.2) and (1.3):

$$r(t + \Delta t) = 2r(t) - r(t - \Delta t) + a(t)\Delta t^2 \tag{1.4}$$

in these equations Δt denotes the duration of the time step, v(t) is the velocity, a(t) represents the acceleration and can be computed by a=F/m, where force can be derived as the gradients of potential with respect to the position:

$$a = \frac{-1}{m}\nabla V(r) \tag{1.5}$$

As shown in Equation (1.4), the coordination of the particles can be calculated without their velocities. However, to compute the system's kinetic energy and assess the energy conservation, velocity is required, which can be obtained by subtracting Equation (1.25) from Equation (1.26) with the error of order Δ^2 [51].

The Leapfrog algorithm Leapfrog integration is alternative numerical technique for Verlet algorithm that was used to solve the equation of the motion [52, 53]. In this integration, the velocities are computed based on half-step:

$$v(t - \frac{1}{2}\Delta t) = \frac{r(t) - r(t - \Delta t)}{\Delta t} \tag{1.6}$$

$$v(t + \frac{1}{2}\Delta t) = \frac{r(t + \Delta t) + r(t)}{\Delta t} \tag{1.7}$$

subsequently, velocity is utilized to compute the new coordinates:

$$r(t + \Delta t) = r(t) + v(t + \frac{1}{2}\Delta t)\Delta t \tag{1.8}$$

$$v(t + \frac{1}{2}\Delta t) = v(t - \frac{1}{2}\Delta t) + a(t)\Delta t \tag{1.9}$$

$$v(t) = v(t - \frac{1}{2}\Delta t) + \frac{1}{2}a(t)\Delta t \tag{1.10}$$

The advantage of the Leap-frog algorithm compared to Verlet is the smaller calculated error for coordinates and velocities. However, the potential issue of simultaneously referring to the coordinate and velocity is still there.

In order to be able to refer coordinate and velocity at the same instant time, Speed Verlet algorithm can be used [54]:

$$v(t + \frac{1}{2}\Delta t) = v(t) + \frac{1}{2}a(t)\Delta t \tag{1.11}$$

$$r(t + \Delta t) = r(t) + v(t)\Delta t + \frac{1}{2}a(t)\Delta t^2 \tag{1.12}$$

after this step, acceleration can be computed by using the new coordinates. Finally, by having the acceleration, and velocity for the second half of the time step, can be calculated below:

$$v(t + \Delta t) = v(t + \frac{1}{2}\Delta t) + \frac{1}{2}a(t + \Delta t)\Delta t \tag{1.13}$$

Energy minimization To minimize the energy of the system before starting the equilibration, an algorithm called steepest descent is applied. This leads the motion of each atom to the direction wherein the energy of the system becomes minimum. In order to link between microscopic behavior of the system and thermodynamic properties in equilibrium, pressure and temperature of the system is computed. Equilibration of the system can take place in two common ways: NVT and NPT ensembles. In NVT ensembles (canonical ensembles), numbers of particles (N), volume (V), and temperature (T) are constant. In NPT ensembles, numbers of particles, pressure, and temperature are remain unchanged. To control and keep the temperature of the system at a specific value, temperature coupling should be applied [55, 50]. The thermostat we applied in our MD simulations will be explained here:

Thermostat The temperature is drived from total kinetic energy of a system with N particle:

$$K = \sum_{i=1}^{N} \frac{|P_i|^2}{2m_i} = \frac{N_{df} k_B T}{2}, \tag{1.14}$$

where p represents linear momentum, N_{df} denotes the number of degrees of freedom, k_B is the Boltzmann constant, and T is the temperature. To perform simulations at constant temperature, NVT ensembles is required [49].

Velocity-rescaling temperature coupling This thermostat can be considered as an extension to Berendsen thermostat by an additional term to keep the temperature of the system constant. The time averaged kinetic energy of each particle can be obtained by:

$$< K >= \frac{1}{2} < \sum_{i=1} m_i v_i^2 > \tag{1.15}$$

or

$$< K >= \frac{N_{df}}{2} k_B T \tag{1.16}$$

by integrating the Equations (1.15) and (1.16), we can drive:

$$\frac{1}{2} < \sum_{i=1} m_i v_i^2 >= \frac{N_{df}}{2} k_B T \tag{1.17}$$

,where instantaneous temperature of the system can be derived as:

$$T(t) = \frac{1}{N k_B} < \sum_{i=1} m_i v_i^2 > \tag{1.18}$$

In this method by re-scaling the velocity for temperature T, the total kinetic energy can maintain constant. The factor to be employed to re-scale the velocity is defined as:

$$\lambda = \sqrt{T_0 / T(t)}, \tag{1.19}$$

, where T_0 is the target temperature of the system and T(t) is the real time temperature.

$$\Delta T = \frac{\sum_{i=1} m_i (\lambda v_i)^2}{N k_B} - \frac{\sum_{i=1} m_i v_i^2}{N k_B} \tag{1.20}$$

$$\Delta T = (\lambda^2 - 1) T(t) \tag{1.21}$$

The advantage of this thermostat is reaching first order decay of temperature deviations without oscillations [56].

Periodic Boundary Conditions The behavior of the infinite and finite systems is not similar. Modeling infinite systems with computational modeling is extremely expensive. On the other hand, considering finite systems with solid walls will result in the collision of adjacent atoms with the wall and cause boundary effects. Applying periodic boundary conditions, i.e., PBC, allows us to resemble an infinite system by just replicating a unit cell of the system in three direction and minimizing the boundary effects. Under this situation, if one particle crosses the top boundary of the unit cell, it can appear from the opposite side (bottom edge).[52, 57, 50, 55].

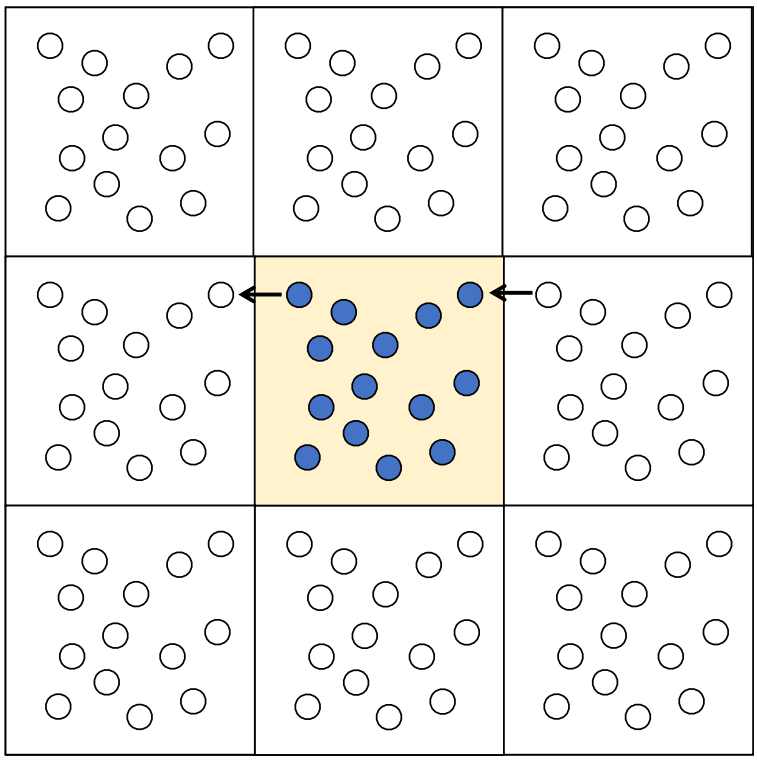

Figure 1.7 Schematic of periodic boundary condition in a unit cell containing fourteen particles in two dimensions [2].

1.4.2 Force fields

The potential energy between all atoms in the space can be related to their coordinates by force field equations. Force filed or potential function can describe the interactions between any atoms of the systems. It contains two terms: bounded interactions and non-bounded [58].

Bonded interaction Atoms bonded with the covalent bond can have interactions due to their bonds length, i.e., 2 body, angles, i.e., 3 body, and torsions, i.e., 4 body. Potential energy related to these interactions is called bonded interaction and is relative to their equilibrium positions [59].

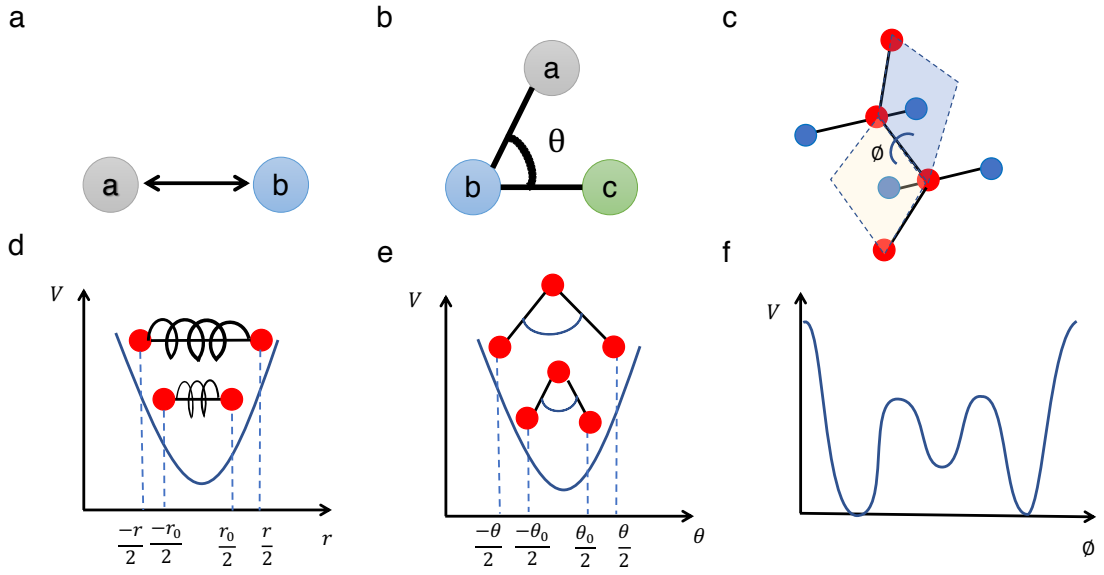

Figure 1.8 Bonded interactions: (a) bond length between two bodies (b) angles between three bodies and (c) dihedral angles between four bodies. Potential energy is related to (d) bond extensions between two bodies, (e) angles distortions between three bodies, and (f) dihedral angles change between four bodies [3, 4].

As shown in Figure 1.8, length of the bond between pair of atoms in covalent bonding can be described by simple harmonic motion and can be resembled by a spring that connects these two atoms. Angle distortion is shown by bending an angel, and it follows the angular vibrational motion. The last one is related to the

distortion of the dihedral angle. The dihedral angle is a four-body interaction. If you consider four atoms in sequence, the first and the last three atoms can form a plane. The angle between these two planes is described by dihedral angles and rotation can occur around this angle [60, 3, 4].

Harmonic potential The length of the bond between pair of atoms (i and j) can be describe by simple harmonic potential (Figure 1.8-panel d):

$$U_b = \frac{1}{2} k_{ij}^b (r_{ij} - b_{ij})^2 \tag{1.22}$$

where b_{ij} denotes the equilibrium bond length and k_{ij}^b represents the force constant.

Angle potential The angle potential between three atoms of i, j, and K can be represented by harmonic potential of the angels (Figure 1.8e):

$$U_a(\theta_{ijk}) = \frac{1}{2} k_{ijk}^\theta (\theta_{ijk} - \theta_{ijk}^0)^2 \tag{1.23}$$

where θ_{ijk}^0 represents equilibrium angle.

Dihedral torsional potential Torsion angle can be obtained by rotation of four covalently bonded atoms, i.e., ijkl, with respect to the central bond. The energy change due to rotation of the bond i-j and bond k-l around the covalent bond j-k represents dihedral torsional energy.

$$U_d(_{ijkl}) = k(cos(n\phi + \delta) + 1) \tag{1.24}$$

where n denotes the periodicity and δ represents the phase.

Ramachandran plot The backbones of the polypeptide chains can have two dihedral angles, which are ϕ and ψ . Different combinations of these two angles can lead to different conformations. The ramachandran plot is a tool to visualize the conformation preference. It will show the statistical distribution of these two angles. As shown in Figure 1.9, two regions for the conformations shown in the plot: allowed regions (lighter colors) and favorable regions (darker colors) [3, 50].

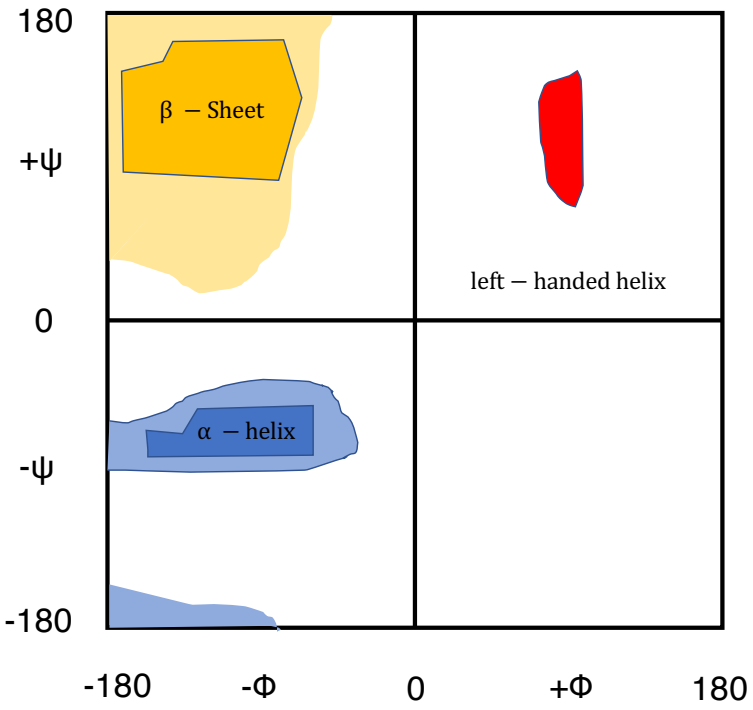

Figure 1.9 Schematic representation of ramachandran plot to visualize torsional angles of ϕ and ψ of the amino-acids.

Non-bonded interaction Non-bonded interaction is any interaction between unbonded atoms within a certain distance from each other. As shown in Equation (1.25), non-bonded interaction has two terms: Lennard-Jones potential and Coulomb interaction–see Equation (1.26).

$$U_{nonbonded} = U_{LJ} + U_C \tag{1.25}$$

$$U_{unbonded} = \frac{1}{2}\sum_i \sum_{j \neq i} 4\epsilon_{ij}\left((\frac{\sigma_{ij}}{r_{ij}})^{12} - (\frac{\sigma_{ij}}{r_{ij}})^{6}\right) + \frac{kq_iq_j}{r_{ij}} \tag{1.26}$$

where ϵ denotes Lennard-Jones well depth and σ represents the distance where the potential energy is zero. The parameters of the force field are optimized by fitting the energy computed from the force field to the experimental measurement or ab initio quantum data [58]. In this dissertation, we used Amber99SB-ILDN force field [61].

CHAPTER 2

USING ALL-ATOM SIMULATIONS IN EXPLICIT SOLVENT TO STUDY AGGREGATION OF AMPHIPATHIC PEPTIDES INTO AMYLOID-LIKE FIBRILS.

Originally published in the **Journal of Molecular Liquids**:
Jalali, S., Yang, Y., Mahmoudinobar, F., Singh, S. M., Nilsson, B. L., Dias, C. (2022). *Using all-atom simulations in explicit solvent to study aggregation of amphipathic peptides into amyloid-like fibrils.* Journal of Molecular Liquids, 347, 118283.

In this chapter, we perform all-atom molecular dynamics simulations in explicit solvent to study the aggregation of amphipathic peptides into amyloid-like fibrils. We use large simulation boxes containing more than 200,000 atoms and including 50 peptides to account for peptide concentrations of the order of 30 mM. Six different peptide sequences are studied in this work. We show that when long simulations (2-3 μs) are performed, a positive correlation is observed between experiments and simulations. In particular, peptide sequences that do not form fibrils in experiments show a low propensity to form inter-peptide hydrogen bonds and β-structures, and vice-versa. Simulations are also performed at different temperatures and NaCl concentration to highlight the importance of hydrophobic and electrostatic interactions on aggregation. The rate of fibril formation in our simulations increases with increasing temperature for amphipathic peptides made from highly hydrophobic amino acids. This phenomena is related to the strength of hydrophobic interactions that enhances with increasing temperature. Electrostatic interactions may be responsible for the preference of anti-parallel β-sheets in our simulations. However, screening these interactions with NaCl favors aggregation of amphipathic peptides made from less hydrophobic amino acids. The sequence of events leading to fibril growth in our simulations is also discussed.

2.1 Introduction

The self-assembly process by which peptides organize themselves into one-dimensional structures is ubiquitous in nature. It is related to several neurodegenerative diseases including Alzheimer's and Parkinson's, and to functional biomaterials used by different organisms to gather food and/or for protection, e.g., silk in spiderwebs and silkmoth eggshells [62, 5]. In recent years, considerable effort has been dedicated to fine-tune the properties of these materials to make them suitable for different biotechnological applications including drug delivery systems and tissue engineering [40, 41, 42, 43, 35, 44, 45, 46]. These properties emerge from the supramolecular one-dimensional structure of the peptide assembly, which is characterized by the stacking of long β-sheets on top of each other accounting for the cross-β signature of amyloid-like fibrils [28, 63]. Currently, our understanding of the forces driving this self-assembly process and the critical events on pathway to fibril formation remains incomplete [48, 64]. It requires probing peptide structures with atomic precision over micro- to millisecond timescales, which is beyond reach of most experimental methods but is becoming accessible to all-atom simulations in explicit solvent. This type of knowledge is expected to improve our understanding of amyloids in biological organisms as well as enable the development of better sequence-structure predictive tools.

Strictly amphipathic peptides are often used as a starting point in the design of new amyloid-like fibril structures [65, 66]. Consecutive residues in these peptides alternate between non-polar (**X**) and polar (Y and Z) amino acids, i.e., $(\mathbf{X}\mathrm{Y}\mathbf{X}\mathrm{Z})_n$. Of particular interest to this work are neutral amphipathic peptides with $n = 2$ and where polar residues are positively and negatively charged lysine (Y=K) and glutamic acid (Z=E), respectively. Each of the two β-sheets that accounts for fibrils from these peptides have one of their faces decorated with non-polar side chains of **X** residues and the other face with charged K and E side chains–see Figure 4.4. These β-sheets are

anti-parallel in nature to provide the proper alignment for the interaction between positive K and negative E residues in neighboring strands [67]. In the fibril, side chains of polar K and E residues are exposed to the solvent whereas non-polar faces of β-sheet are buried against each other forming a stable dry core–see Figure 4.4. This type of cross-β structure formed by strictly amphipathic sequences correspond to the symmetry class 5 in the Sawaya/Eisenberg classification scheme of fibrils [68, 69].

One of the challenges of studying fibril formation is that the aggregation process is strongly sensitive to experimental conditions. Thus, it is important to compare experiments performed under the same conditions when studying the effect of the peptide sequence. Experimental studies have explored the role of hydrophobicity in fibril formation by probing different non-polar amino acids at position **X** of the (**X**K**X**E)$_2$ sequence [70, 71]. For the least hydrophobic amino acid, i.e., alanine (X=A), peptides did not self-assembly up to a concentration of 8 mM [72, 70]. In contrast, peptides made from the more hydrophobic amino acids, i.e., phenylalanine (F), leucine (L) or valine (V), formed amyloid fibrils already at concentrations of 0.2 mM [72, 70]. The net hydrophobicity is, however, not the only factor accounting of a sequence's propensity to form fibrils as amphipathic sequences in which pairs of non-polar residues are flanked by charged residues, i.e., (K**FF**E)$_2$, did not form fibrils at concentrations up to 1 mM as opposed to KE**FFFF**KE or the strictly amphipathic (**F**K**F**E)$_2$ sequence [67]. This profound influence of the sequence pattern on fibril formation was related to its effect on the propensity of a peptide to form β-sheets and its ability to enable non-polar and charged side chains to segregate to different faces of a β-sheet [67].

All-atom simulations in explicit solvent have the potential to provide a more complete picture of the aggregation process by characterizing the sequence of events and the molecular mechanisms accounting for fibril formation [64, 73]. However, simulations starting with peptides randomly distributed in space which aggregate into

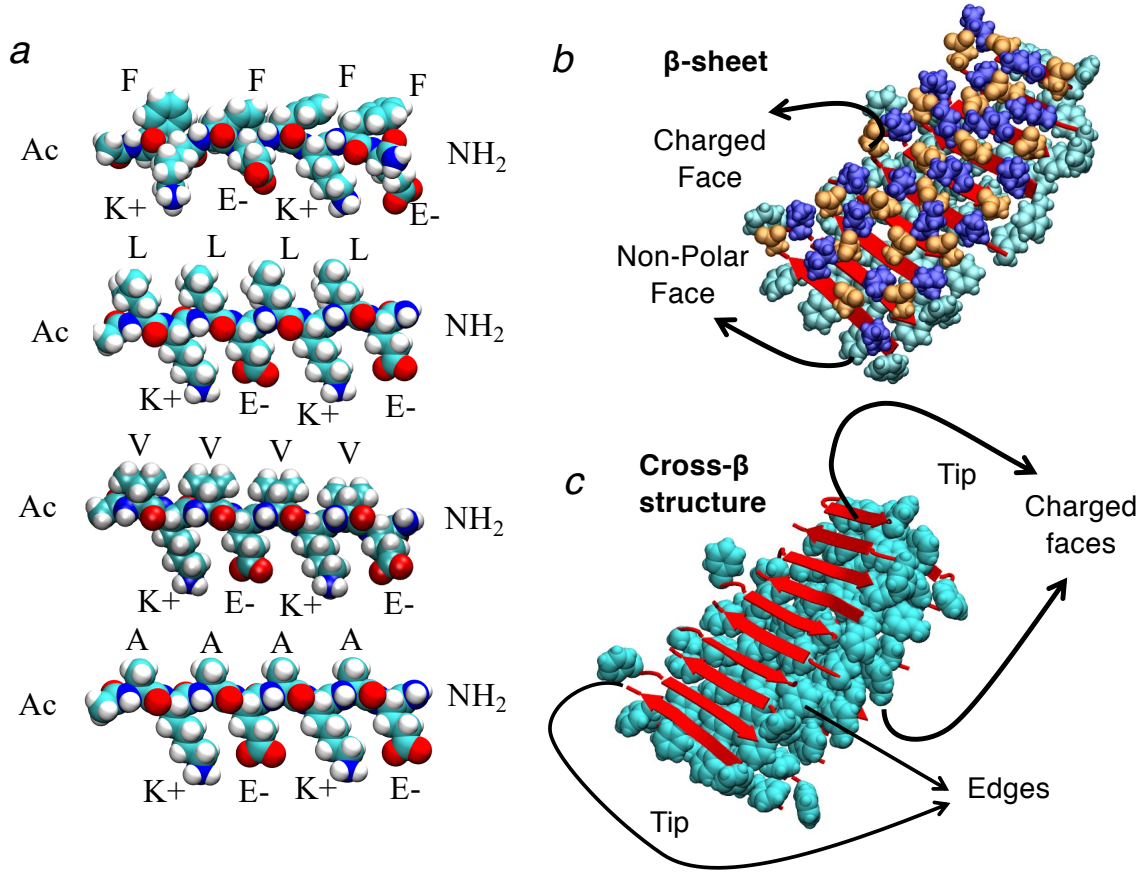

Figure 2.1 Cross-β structure of strictly amphipathic sequences Ac-(**X**K**X**E)$_2$-NH$_2$, where K and E represent positively and negatively charged lysine and glutamic acid, respectively. (a) Atomic structures of peptides in which the non-polar residue **X** is phenylalanine (F), leucine (L), valine (V), or alanine (A). (b) β-sheet from strictly amphipathic sequences wherein charged and non-polar residues are exposed to different faces of the sheet. Non-polar side chains are depicted in cyan. Purple and orange colors are used for lysine and glutamic acid, respectively. (c) Packing of two β-sheets into a cross-β structure wherein the dry core is formed by non-polar side chains in cyan.

amyloid fibrils are very time consuming as they require tracking a large number atoms (e.g., $> 200,000$ atoms to account for peptide concentrations of the order of 10 mM) for a long time ($> 1\mu$s). Moreover, it is not possible to fully reproduce experimental conditions [48] and the ability of force fields to account for fibril formation remains a question of debate [74, 75]. Accordingly, simulations of spontaneous aggregation using all-atom models have been performed for only a small number (< 10) of short peptides, which mostly do not self-assemble into stable cross-β structures. Nonetheless, promising results have recently been obtained for the Aβ_{16-22} sequence, suggesting that, at least for short peptide sequences, all-atom simulations will soon reach a state where they can work hand-in-hand with experiments complementing each other [74]. Regarding the amphipathic (K**FF**E)$_1$ sequence, recent all-atom simulations of tetramers have illustrated the challenge of interconverting disordered aggregates into ordered ones [76]. Short femtosecond-long all-atom simulations of (**F**K**F**E)$_2$ peptides have also been performed to test the stability of different fibril structures varying in the hydrogen bond pattern of their β-sheets [77, 78].

Here, we expand on these computational studies by performing large-scale (50 peptides in a simulation box containing more than ∼200,000 atoms) and long-time simulations to provide insights into the aggregation process of six peptide sequences at different conditions of temperature and salt-concentration. Some of our simulations are more than one order of magnitude (10-14 μs) longer than the length of most all-atom molecular dynamics studies of aggregation (0.5–1 μs). We show that, in most cases, the latter timescale is not enough to enable the formation of cross-β structures or to discriminate the aggregation process of different amphipathic peptide sequences. However, when longer ($>$ 2-3 μs) simulations are performed, we observe a positive correlation between aggregation *in silico* and *in vitro* wherein sequences that do not form fibrils in experiments have a low propensity to form inter-peptide hydrogen bond and β-structures in our simulations. Moreover, we show that increasing

temperature causes aggregation to take place faster for highly hydrophobic amino acids, which we relate to the enhanced strength of hydrophobic interactions with increasing temperature. A preference for the formation of anti-parallel β-sheets is also observed in fibrils that formed spontaneously in our simulations. Whereas electrostatic interactions are expected to drive this preference, these interactions may also be unfavorable to fibril formation [79]. In our simulations, screening these interactions by adding salt to the solution increased the preference for fibril formation.

2.2 Methodology

System Design, Equilibration and Simulation. Four strictly amphipathic peptides with sequences alternating between non-polar (represented by the letter **X**) and charged (represented by letters **E** and **K** for the negatively and positively charged glutamic acid and lysine residues, respectively) residues were investigated in this study. These eight-residue peptides were capped with an acetyl group (Ac) at the N terminus and an amide group (NH_2) at the C terminus, i.e., Ac-(**X**K**X**E)$_2$-NH_2. The four peptides studied here differ in the degree of hydrophobicity of their non-polar residue, which is either phenylalanine (F), leucine (L), valine (V), or alanine (A)–see Figure 4.4. We will refer to these strictly amphipathic sequences as F-, L-, V-, and A-peptides. Experimentally, the more hydrophobic F-, L-, and V-peptides were shown to form fibrils as opposed to the less hydrophobic **A**-peptide [70]. We also performed simulations of two sequences that are amphipathic but they do not have alternating hydrophilic/hydrophobic sequence order , i.e., Ac-(KE**FFFF**KE)-NH_2 and Ac-(K**FF**E)$_2$-NH_2. Self-assembly into amyloid fibrils was observed in experiments using the former peptide sequence at concentrations of 1 mM but not the latter [67].

Simulations in this work were prepared in two steps. First, 50 peptides were randomly place in a cubic box of length 8 nm, which was then solvated and the energy of the system minimized followed by a 4 ns equilibration in the NVT ensemble.

Second, to avoid creating a self-assembly process in which an elongated aggregate interacts with itself through periodic boundary conditions, the size of the simulation box was increased to 13.5 nm and solvated accounting for a peptide concentration of 37 mM. The energy of the system was minimized and equilibrated in the NVT ensemble.

Software, Hardware, and parameters. MD simulations were performed with the Amber99sb-ILDN force field [61] and the TIP3P water model by applying periodic boundary conditions in the isothermal-isobaric (NPT) ensemble. The leapfrog algorithm was used to integrate the equations of motion with a 2 fs time-step [55]. The Parrinello-Rahman barostat ($\tau_p = 2.0$ ps) was used to maintain the pressure of the system at 1 bar [80]. Temperature was controlled by coupling protein and solvent separately to the velocity-rescale thermostat ($\tau_t = 0.1$ ps). The cut-off for short range van der Waals and electrostatic interactions was 1.0 nm. The smooth Particle Mesh Ewald algorithm was used to compute long range electrostatic interactions [81]. For all systems, the production run started with a 100 ns simulation in the NPT ensemble using GROMACS [82]. Some of these simulations were then extended either on Anton 2 supercomputer [83] or on our local cluster using GROMACS–see Table 3.1 for a list of all simulations performed here.

Table 2.1 Details of all Simulations

Peptides	Temperature (K)	NaCl (mM)	Length of Simulations
Ac-$(FKFE)_2$-NH_2	300	-	1 μs
	350	-	10 μs (Anton2)
	370	-	1 μs
	450	-	1 μs
Ac-$(VKVE)_2$-NH_2	350	-	14 μs (Anton2)
	370	-	1 μs
	450	-	1 μs
Ac-$(LKLE)_2$-NH_2	350	-	1 μs
	450	-	1 μs
Ac-$(AKAE)_2$-NH_2	300	-	1 μs
	350	-	1 μs
	350	40	1 μs
	350	80	1 μs
	350	160	1 μs
	450	-	0.5 μs
Ac-$(KFFE)_2$-NH_2	350	-	3 μs (Anton2)
	450	-	0.627 μs
Ac-KEFFFFKE-NH_2	350	-	3 μs (Anton2)
	450	-	0.627 μs

Analysis. To quantify the extent of by which peptides self-assemble into β-sheets in our simulations, we track the number of hydrogen bonds (N_{HB}) between backbone atoms over time [84]. This quantity is also decomposed into contributions from intra- (intra-N_{HB}) and inter-backbone (inter-N_{HB}) hydrogen bonding. We consider that an hydrogen bond forms when the distance between donor and acceptor atoms is less than or equal to 0.35 nm and the angle between hydrogen, donor and acceptor atoms is less than or equal to 30 degree. Contact maps (CM) were used to provide insights into inter-peptide interactions formed during the self-assembly process. For that purpose, two residues are considered to be in contact if the distance between any pair of their respective atoms is less than or equal to 0.4 nm. The sum of inter-peptide contacts was normalized to account for a probability of contacts. The python scripts provided by the Strodel group [85] was used for that purpose with the required libraries [86, 87, 88]. Secondary structures are defined using the DSSP (*Define Secondary Structure of Proteins*) algorithm [89].

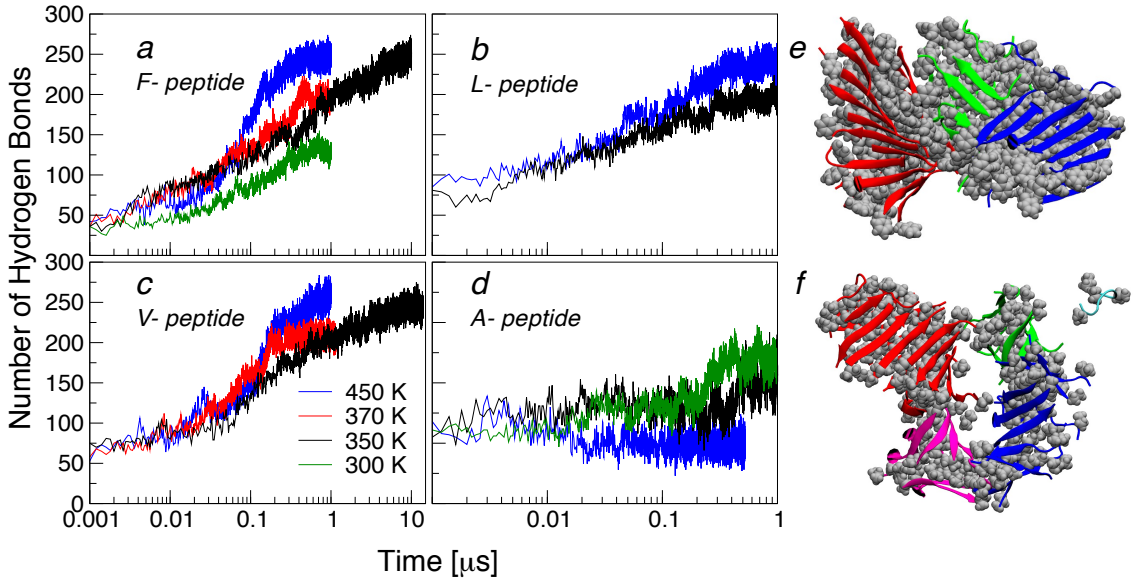

Figure 2.2 Effect of temperature on self-assembly. Backbone hydrogen bond formation in our simulations using strictly amphipathic (a) F-, (b) L-, (c) V-, and (d) A-peptides at different temperatures. Last configuration in our simulations performed at 350 K using (e) F- and (f) V-peptides. van der Waals representation is used to depict non-polar side chains in gray and secondary-structures are shown using a cartoon representation where β-sheets are shown by arrows. Different colors are used for cross-β structures that are not (or are loosely) connected to each other via hydrogen bonds.

2.3 Results and Discussion

2.3.1 Role of hydrophobic interactions on fibril formation.

In Figure 2.2, we show the time dependence of the total number of backbone hydrogen bonds, i.e., N_{HB}, for simulations performed using strictly amphipathic sequences in pure water. A logarithmic scale is used for the x-axis to highlight the aggregation process at short timescales when N_{HB} is subjected to large changes. Panel a shows that, for the F-peptide at 350 K (black line), N_{HB} increases with time and it starts saturating after approximately 4 μs. At 300 K (green line), N_{HB} increases at a significantly slower pace than at 350 K suggesting that increasing temperature accelerates the self-assembly process that leads to fibril formation. Note that recent experimental studies have reported a similar effect for elastin-based peptides over the temperature range 293–353 K [90]. To further highlight this effect of temperature, we perform additional simulations at extreme temperatures of 370 and 450 K. Simulations

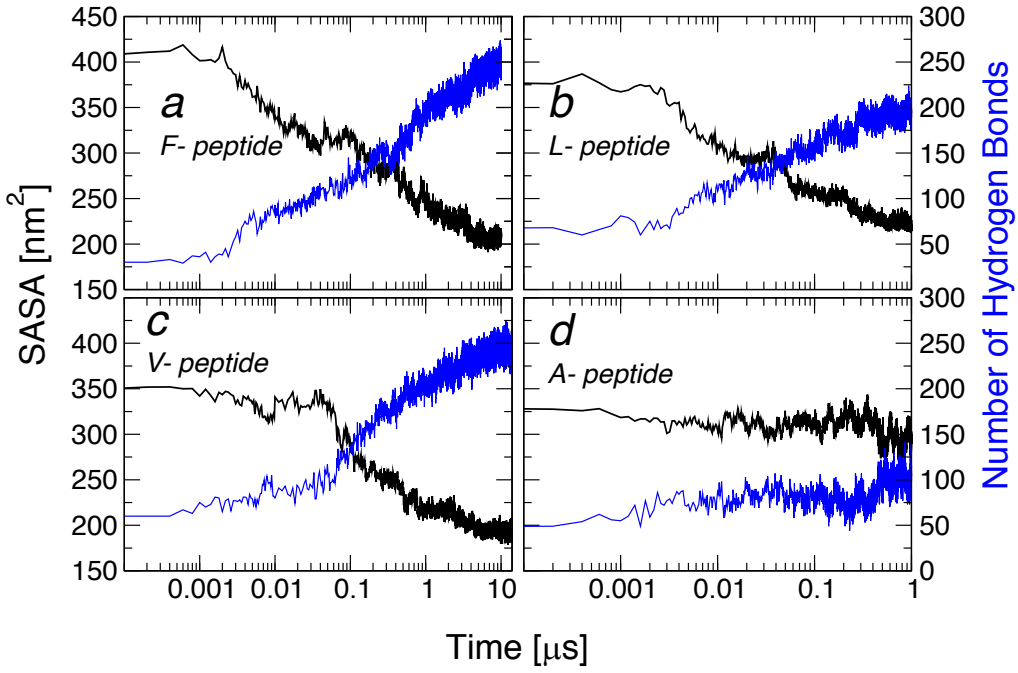

Figure 2.3 Burial of non-polar side chains. The time-dependence of the solvent accessible surface area (SASA) of non-polar residues is shown for (a) F-, (b) L-, (c) V-, and (d) A-peptides from simulations performed at 350 K. The number of backbone hydrogen bonds is also shown in blue.

at these extreme temperatures should, however, be taken with caution and they are only used here to highlight the trend observed at 300 and 350 K. The increase in N_{HB} at 370 K occurs at approximately the same rate as in our simulations at 350 K but it takes place significantly faster at 450 K saturating after only 0.6 μs. Temperature has a similar effect on N_{HB} for the L- and V-peptides in panels b and c. In particular, for the L-peptide, N_{HB} increases significantly faster at 450 K than at 350 K. For the V-peptide at 450 K, N_{HB} saturates after only 0.6 μs whereas 10 μs are required for this to happen at 350 K. For the less hydrophobic A-peptide, N_{HB} does not increase in a significant manner at any temperature–see panel d. This is consistent with experimental studies highlighting the importance of hydrophobic interaction in the formation of stable aggregations [70, 72]. Moreover, at any time during the simulation, this less hydrophobic peptide forms less hydrogen bonds at the higher temperature (450 K) than at lower temperatures, i.e., 300 K and 350 K.

At first sight the faster aggregation of F-, L-, and V-peptides with increasing temperature is counterintuitive as temperature favors states with higher entropy wherein peptides would be dispersed in the simulation box. However, hydrophobic interactions play an important role in the attraction between amphiphilic peptides and the strength of these interactions increases with increasing temperature to maximize the entropy of the solvent [91, 92, 93, 94, 95]. Hydrophobicity is therefore expected to be the force driving peptide self-assembly in our simulations of F-, L-, and V- peptides, as it can explain the increased rate of aggregation with increasing temperature in panels a-c. This is consistent with studies showing that amyloid fibrils that have a non-polar core become more stable with increasing temperature [96, 90, 97, 98, 99]. In the same vein, the inability of the A-peptide to self-assemble and form fibrils in simulations (see panel d) and experiments [70, 72] can be explained by the reduced hydrophobic nature of this peptide.

Final structures of simulations performed using F- and V-peptides at 350 K are shown in Figure 2.2 e-f. In these structures, peptides form cross-β structures with most non-polar side chains (in gray) buried away from the solvent. A different color is used to represent cross-β structures that are not connected to each other through backbone hydrogen bonds highlighting different unit blocks. Notice that solvent exposed non-polar side chains are located either at the tip or at the edge of cross-β structures. Burial of these exposed non-polar side chains away from the solvent drives packing of cross-β units in our simulations. Because phenylalanine has a bulkier side chain than valine, edges of cross-β structures from F-peptides have more exposed non-polar surface area than for V-peptides–see Figure 2.2e-f. Accordingly, non-polar side chains at edges and tip of cross-β structures in our simulations of the F-peptide are buried against each other–see blue and green as well as red and green cross-β structures in Figure 2.2e. For the V-peptide, the different cross-β structures are connected to each other mostly through the "tip" which has exposed non-polar

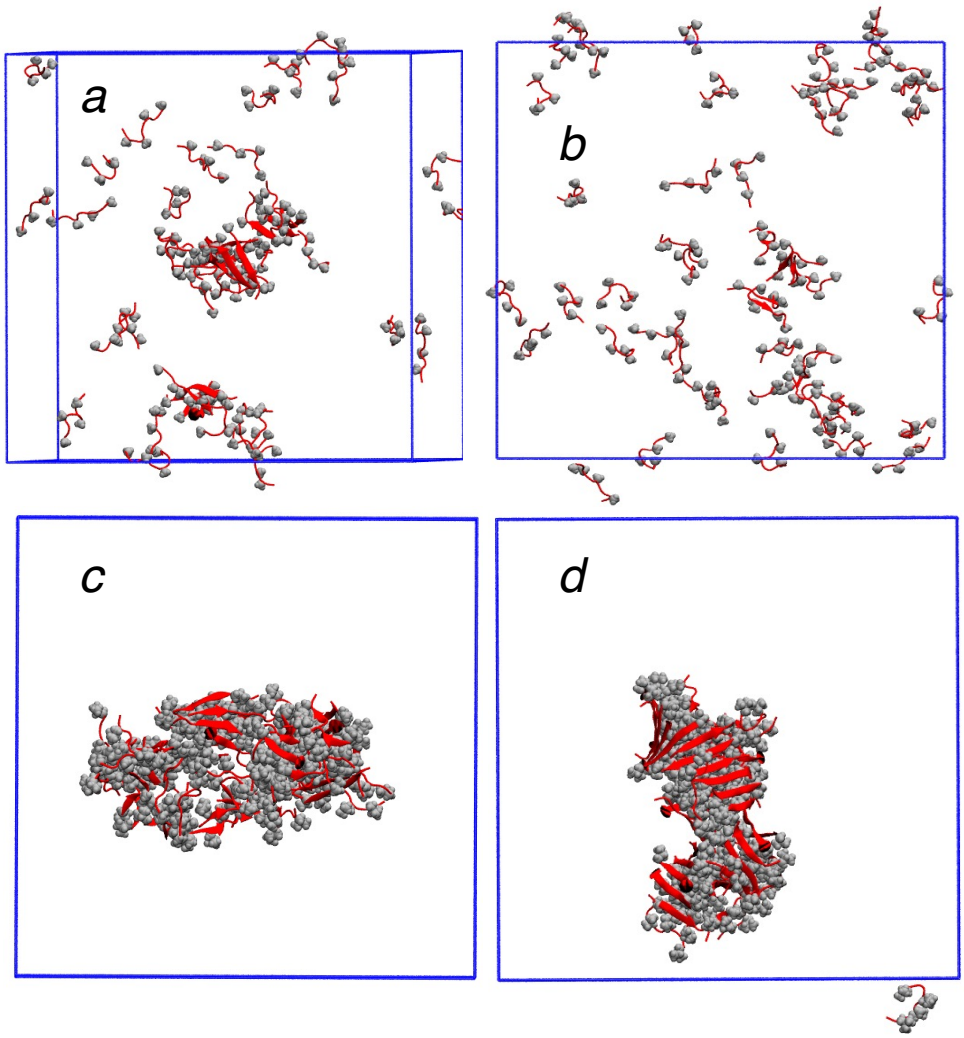

Figure 2.4 Last configurations of A-peptides at (a) 350K, (b) 450K, and L-peptides at (c) 350K, and (d) 450K. Van der Waals and new-cartoon representation are used to depict non-polar residues and β-sheet, respectively.

side chains. Last configurations of L- and A-peptides in our simulations at 350 K and 450 K are shown in Figure2.4.

To further highlight the importance of non-polar burial, we show in Figure 2.3 the time dependence of both the solvent accessible surface area (i.e., SASA) of non-polar side chains and N_{HB}. For F-, L-, and V-peptides, SASA (black lines) and N_{HB} (blue lines) decreases and increases, respectively, with time as hydrophobic interactions between non-polar side chains and hydrogen bonds between backbone atoms form during fibrilization. This shows strong correlation between non-polar

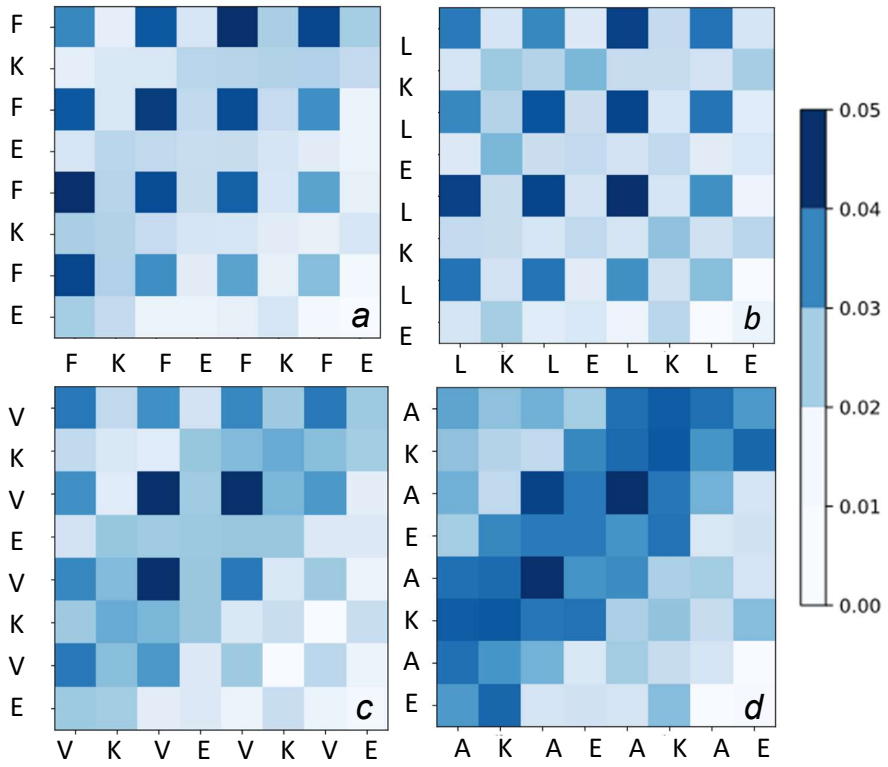

Figure 2.5 Contact maps computed for strictly amphipathic a) F-, (b) L-, (c) V-, and (d) A-peptides in simulations performed at 350 K. Only the last 500 ns of our simulations are used in the calculation of contact maps.

burial and β-sheet formation. For the A-peptide (panel e), SASA and N_{HB} change only modestly due to the lack of cross-β structure formation. Contact maps (i.e., CM) computed during the last 500 ns in our simulations at 350 K are shown in Figure 4.8 to depict pairs of residues involved in interpeptide interactions. Contacts between non-polar residues for F-, L-, and V-peptides occur at least twice more frequently than between charged K and E residues. These non-polar contacts are formed with neighboring residues on the same β-sheet as well as with residues on the other sheet of the cross-β structure. Conversely, charged residues, which are facing the solvent, can only form contacts with neighboring residues on the same β-sheet. Notice that because of the absence of a dry core for the A-peptide, both non-polar and charged residues interact with approximately the same probability in our simulations. Figure 4.8 also depicts a tendency of peptides to form antiparallel contacts wherein the first residue interacts preferentially with the last or second to last non-polar residue. Accordingly, 72% and 65% of all pairs of neighboring strands for F- and V- peptides in Figure 2.2e-f form anti-parallel β-sheets. Electrostatic interactions between charged side chains can be used to discriminate parallel and anti-parallel β-sheets[70]. In a parallel setup, like-charged residues (K–K or E–E) of neighboring strands face each other whereas, in anti-parallel β-sheets, opposite-charged pairs of residues (K–E) of neighboring strands face each other optimizing electrostatic interactions.

2.3.2 Growth of cross-β structures.

Figure 4.9 depicts the time evolution of secondary structures in our simulations. Initially, peptides are mostly disordered and, thus, residues adopt preferentially coil (see panel b) or bend/turn (see panel c) conformations. As the simulation evolve in time, the fraction of residues adopting β conformations increases from 0.1 to 0.5 for F- and V- peptides and from 0.1 to 0.3 for L-peptides. Congruently, the number of disordered residues (coil and bend/turn in panels b and c) decreases proportionally.

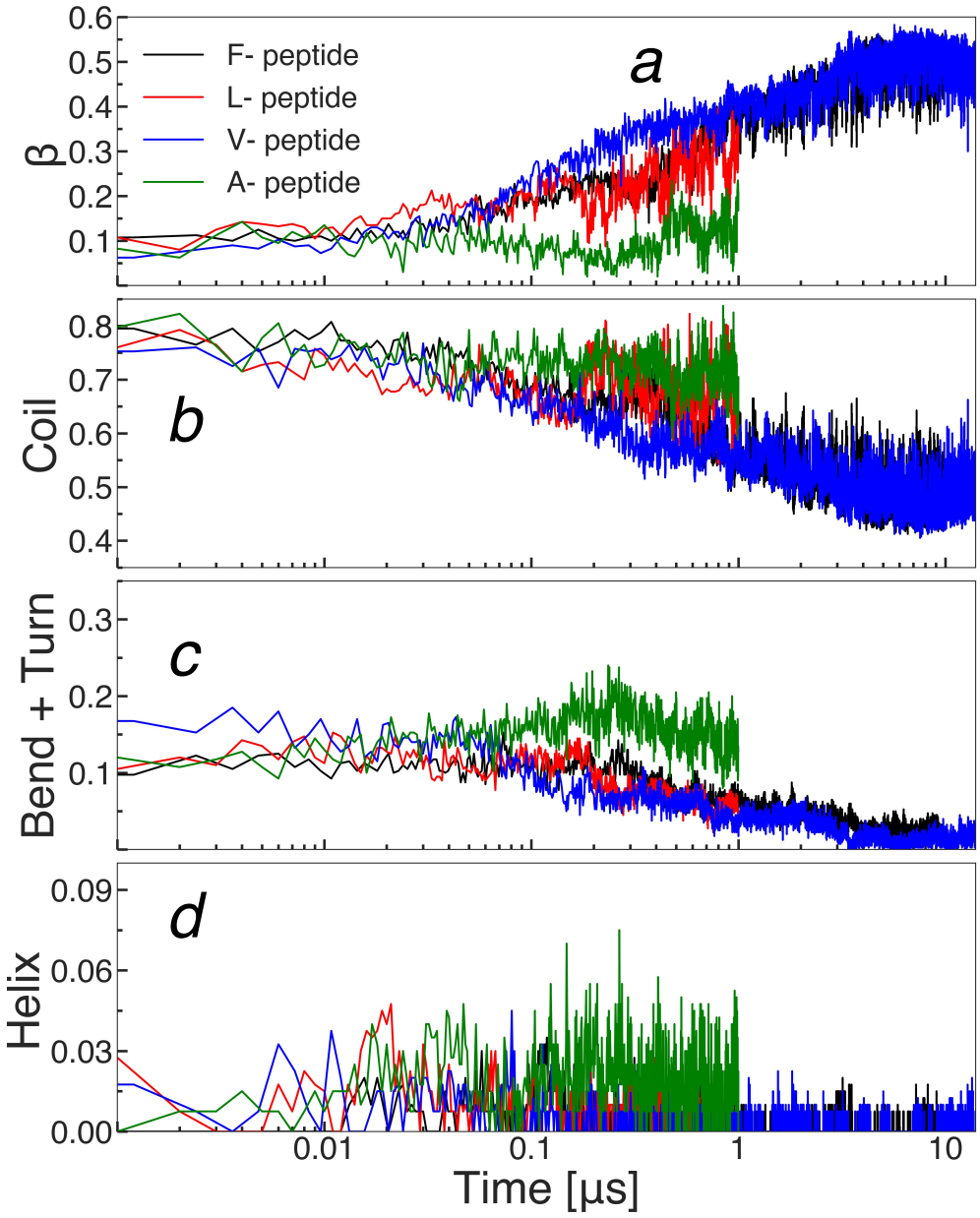

Figure 2.6 Secondary structures of strictly amphipathic peptides in simulations performed at 350 K. Fraction of all residues adopting (a) β, (b) coil, (c) bend+turn, and (d) helical conformations as a function time.

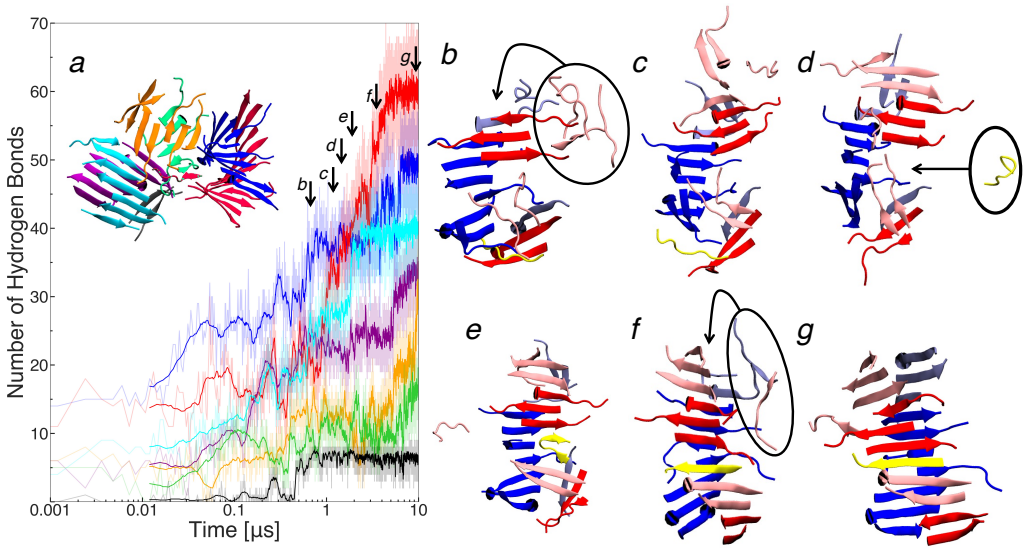

Figure 2.7 Growth of the seven β-sheets that formed spontaneously in our simulation performed using F-peptides at 350K. (a) Number of backbone hydrogen bonds of each β-sheet as a function of time. Thick lines are a guide to the eye and they correspond to moving averages over 25 ns. Panels b, c, d, e, f, and g correspond to the configurations of two sheets at time 0.7 μs, 1.1 μs, 1.5 μs, 1.9 μs, 3.5 μs and 10 μs, respectively. Disordered monomers in the vicinity of the sheets are drawn in light red and light blue.

For the A-peptide, the fraction of residues adopting β conformations increases only marginally from 0.1 to 0.2. Similarly the number of disordered residues for the A-peptide, i.e., coil and bend/turn conformations, does not decrease significantly as in the case of the more hydrophobic sequences. This is consistent with this peptide not forming fibrils in the 1 μs time-frame in our simulations. The fraction of residues in helical conformations is not significant for the more hydrophobic peptides and it is small (but not zero) for the A-peptides consistent with the high propensity of alanine to form α-helices [100].

To provide insights into the formation of cross-β structures in our simulations, we identify the peptides that are part of the different β-sheets at the end of our simulations and compute separately the number of backbone hydrogen bonds between these peptides as a function of time. For the F-peptide, seven β-sheets varying in size from two (black color in Figure 4.10a) to eleven (red color) peptides are present at the end of our 350 K simulation. The two β-sheets with the highest number of

hydrogen bonds (red and blue lines) at the end of the simulation are part of the same cross-β structure. Similarly, sheets with the third and fourth highest number of hydrogen bonds (light blue and purple) are part of the same cross-β structure. The smallest cross-β structure in our simulation is made from the β-sheets with fifth and sixth highest number of hydrogen bonds (yellow and green lines in Figure 4.10). This suggests a correlation between the growth of the two sheets that are part of the same cross-β structures.

Figure 4.10b-g illustrates the growth of the largest cross-β structure represented by red and blue β-sheets in panel a. At 0.7 μs (panel b), a β-sheet extending over seven peptides (in blue) has already formed on top of which two small β-sheets (in red) are deposited at the extremity of its non-polar face. Non-polar side chains of these "blue" and "red" sheets are packed against each other forming stable dry cores. Growth of both red and blue β-sheets occur concurrently via displacement of peptides located in their vicinity towards the tip–see arrows in panel b-g. Also, peptides are being deposited in the space between the two red sheets. This is illustrated in panels d-g where yellow and light red peptides land in between the two red β-sheets forming hydrogen bonds with both of them. Initially, the yellow peptide is folded into a β-hairpin–panel e. Unfolding of the β-hairpin enables this yellow peptide to become extended where it forms hydrogen bonds with just one of the red sheets without interacting with the other red sheet–see panel f. Displacement of red sheets along the main axis of the cross-β structure allows the yellow peptide to connect the two red sheets via hydrogen bonds–see panel g. This depicts the formation of a cross-β structure wherein one sheet behaves as the substrate on top of which peptides are being deposited.

In Figure 4.11, we show the growth of different β-sheets in simulations performed using the V-peptide at 350 K. At the end of the simulation, we identify eight sheets that are not (or are only loosely) connected to each other via backbone hydrogen

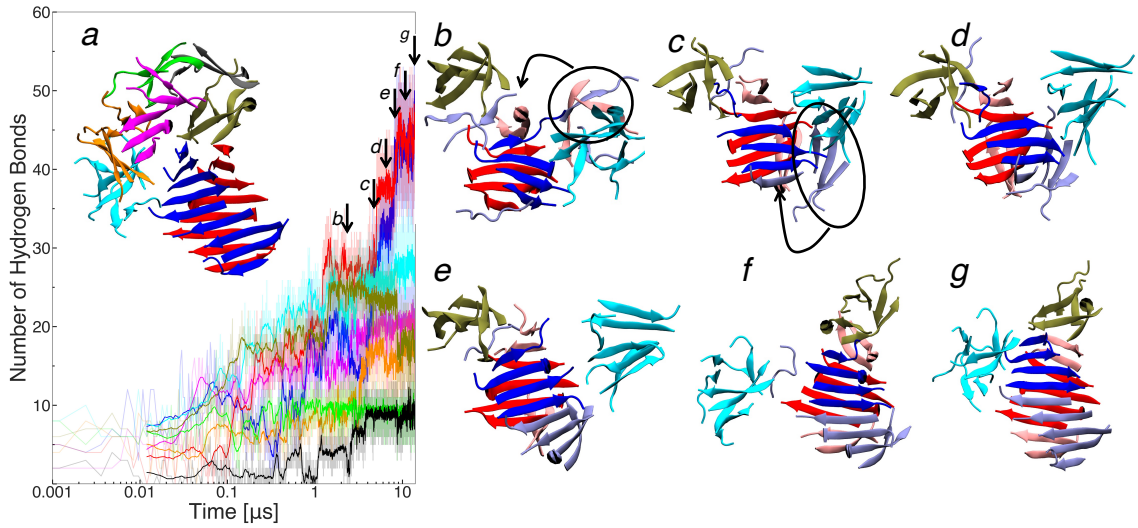

Figure 2.8 Growth of the eight β-sheets that formed spontaneously in our simulation performed using V-peptides at 350K. (a) Number of backbone hydrogen bonds of each β-sheet as a function of time. Thick lines are a guide to the eye and they correspond to moving averages over 25 ns. Panels b, c, d, e, f, and g correspond to the configurations of two sheets at time 2.1 μs, 5.6 μs, 6.4 μs, 8.1 μs, 11.5 μs and 14 μs, respectively. Disordered monomers in the vicinity of the sheets are drawn in light red and light blue.

bonds. The two largest sheets (represented in red and blue) in panel a are part of the same cross-β structure. At 2.1 μs (panel b), each of these sheets contain four peptides. As for the F-peptide, the growth of these sheets occurs mainly via the displacement of peptides that are located in their vicinity towards the tip–see arrows in panels b-e. In addition to this cross-β structure, six β-sheets that are only loosely connected to each other through hydrogen bonds are present at the end of our simulation. These sheets are highly distorted enabling the formation of a dry core within themselves where valine side chains are buried away from water. The evolution of two of those β-sheets is depicted in light blue and brown colors in panels b-g. They correspond to sheets with the third and fourth largest N_{HB} in panel a. These sheets form early and they remain stable throughout the simulation. The absence of distorted β-sheets in our simulations using the F-peptide may be explained by the bulky side chain of phenylalanine, which imposes steric constrains on compact conformations.

2.3.3 Role of the amino acid sequence pattern on fibril formation

The net hydrophobicity of amphipathic sequences is an important factor determining the ability of peptides to form amyloid-like fibrils. However, experimental studies have also highlighted the importance of the sequence pattern on the self-assembly process [101, 65, 102]. In particular, peptides composed of identical amino acids as the F-peptides but with non-polar and charged residues located at different positions in the sequence have been tested for fibril formation [67]. Two such peptides are amphipathic Ac-(K**FF**E)$_2$-NH$_2$ and Ac-KE**FFFF**KE-NH$_2$ sequences that have non-polar segments made from two and four consecutive phenylalanines, respectively, flanked by charged residues. Compared to the F-peptide, which forms fibrils at concentrations of 0.2 mM and 1 mM, Ac-KE**FFFF**KE-NH$_2$ only formed fibril at 1 mM, and Ac-(K**FF**E)$_2$-NH$_2$ does not self-assemble at both concentration [67]. A possible explanation for this sequence pattern effect may come from the low propensity of K and E residues to form β-sheets [100]. The less fibril-prone sequences have patches with two consecutive charged residues, i.e., EK or KE, which may reduce the propensity of peptides to form β-strands specially when located in the middle of the sequence–as in the case of the Ac-(K**FF**E)$_2$-NH$_2$ peptide [67]. Also, the inability of non-polar and charged residues to be segregated into different faces of a β-sheet for Ac-(K**FF**E)$_2$-NH$_2$ and Ac-KE**FFFF**KE-NH$_2$ peptides is expected to contribute to their reduced propensity to form fibrils [67].

To provide insights into effects of sequence pattern on the self-assembly process of the F-peptide, we performed additional 3 μs simulations using Ac-(K**FF**E)$_2$-NH$_2$ and Ac-KE**FFFF**KE-NH$_2$ peptides. All simulations were performed under the same conditions described in the methodology section for the F-peptide. Figure 2.9a compares the evolution of the total number N_{HB} of backbone hydrogen bonds for these peptides over time. The F-peptide forms hydrogen bonds much faster than the other two peptides, consistent with its higher experimental propensity to form fibrils.

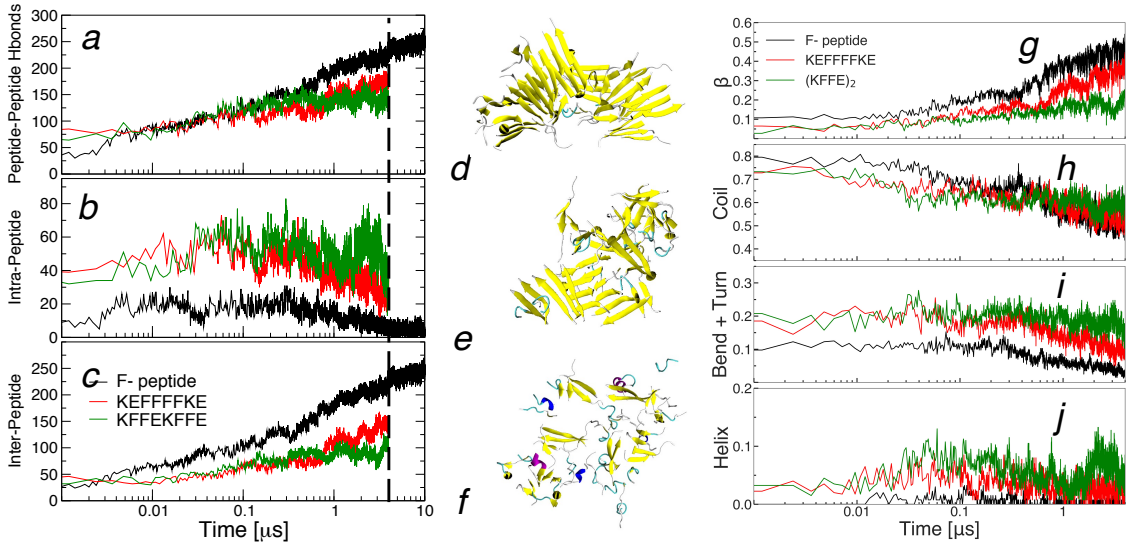

Figure 2.9 Effect of sequence pattern on fibril formation.Time evolution of the number of (a) total,(b) intra-, and (c) inter-peptide backbone hydrogen bonds for F- (black), Ac-KE**FFFFF**KE-NH_2 (red), and Ac-(K**FF**E)$_2$-NH_2 (green) peptides. Peptide configurations at 4 μs from simulations of (d) F-, (e) Ac-KE**FFFFF**KE-NH_2, and (f) Ac-(K**FF**E)$_2NH_2$ peptides. Yellow, cyan, white, purple and blue colors are used to represent β-structures, turn, coil, α-helix and 3-10 helix structures. Fraction of all residues adopting (g) β, (h) coil, (i) bend+turn, and(j) helical structures.

Moreover, after 3 μs most F-peptides in our simulations adopt β-sheet structures–see Figure 2.9d. The time evolution of N_{HB} is very similar for Ac-KE**FFFFF**KE-NH_2 and Ac-(K**FF**E)$_2$-NH_2 sequences although their final structures are significantly different–see Figure 2.9e-f. A cross-β structure and several large β-sheets comprising 4-5 peptides are observed in simulations using Ac-KE**FFFFF**KE-NH_2 peptides (panel c) while Ac-(K**FF**E)$_2$-NH_2 peptides (panel d) adopt mostly coil and turn structures with high propensity. These structural differences are in line with experiments showing that the Ac-KE**FFFFF**KE-NH_2 sequence has a greater probability of forming fibrils compare to Ac-(K**FF**E)$_2$-NH_2.

The similarity in the time dependence of N_{HB} for Ac-KE**FFFFF**KE-NH_2 and Ac-(K**FF**E)$_2$-NH_2 sequences can be understood by decomposing this quantity into intra- and inter- peptide backbone hydrogen bonding, i.e., intra-N_{HB} and inter-N_{HB}, respectively. These quantities are shown in Figure 2.9b-c. The F-peptide (black line) forms less intra-N_{HB} than the other two sequences and after 0.3 μs this quantity

decreases continuously in the simulation (see panel b) while inter-N_{HB} increases over time (see panel c). This characterizes the F-sequence as having a high propensity to interact with neighboring peptides via backbone hydrogen bonds. Although the initial intra-N_{HB} for the Ac-KE**FFFFF**KE-NH_2 sequence (red line) is much larger than for the F-peptide, this quantity also decreases after 0.3 μs (panel b) while inter-N_{HB} increases continuously but modestly throughout the simulation (see panel c). Thus, this peptide also has a preference for interacting with neighboring peptides via backbone hydrogen bonds although this preference is smaller than for the F-peptide. The initial intra-N_{HB} for the Ac-(K**FF**E)$_2$-NH_2 sequence (green lines) is comparable to the one for the Ac-KE**FFFFF**KE-NH_2 peptide but this quantity does not decrease significantly during the simulation (panel b) and inter-N_{HB} remained constant during the last 2 μs of our simulations (see panel c). This highlights the lack of propensity of the Ac-KE**FFFFF**KE-NH_2 sequence to interact with neighboring peptides and aggregate.

In Figure 2.9g-j, we show the time evolution of the fraction of residues in different secondary structures for F-, Ac-(K**FF**E)$_2$-NH_2 and Ac-KE**FFFFF**KE-NH_2 sequences. These peptides are highly disordered in the beginning of the simulations with the fraction of all residues adopting coil and bend+turn structures being 0.7-0.9 and 0.1-0.2, respectively–see panel h-i. As the simulation progresses, peptides become more ordered. In particular, disordered structures are replaced with β-conformations at a rate that increases in the following sequence order: F-peptide > Ac-KE**FFFFF**KE-NH_2 > Ac-(K**FF**E)$_2$-NH_2, which corroborates the experimental sequence propensity to form fibril. Note that the number of β-structures does not change for the Ac-(K**FF**E)$_2$-NH_2 peptide in the last 2 μs of the simulation, consistent with the lack of formation of new inter-peptide hydrogen bonds in panel c. Interestingly, a residual number of α-helices is observed in the reversed order of fibril propensity, i.e., Ac-(K**FF**E)$_2$-NH_2 > Ac-KE**FFFFF**KE-NH_2 >> F-peptide. Thus, sequences that do not

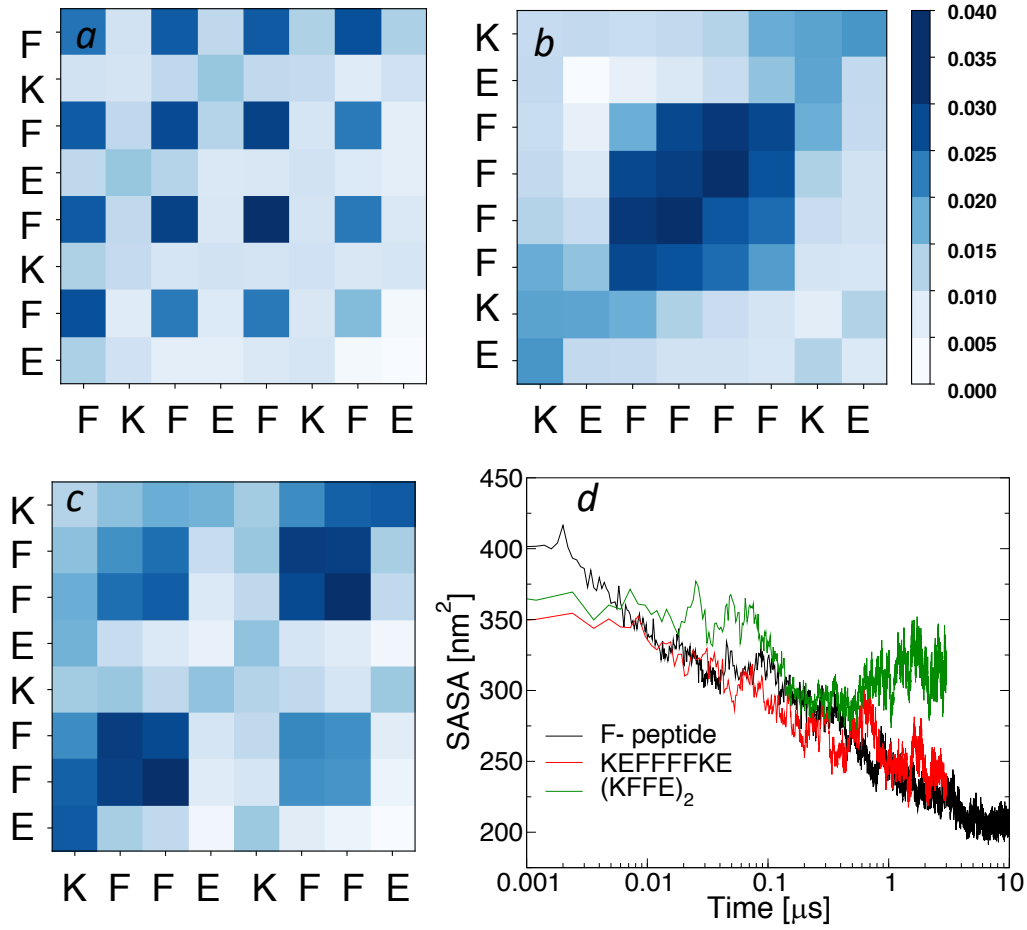

Figure 2.10 Effect of sequence pattern on contact map and SASA. Contact maps computed within 2.5-3 μs in our simulations using (a) F-peptide, (b) KE**FFFF**KE, and (c) (K**FF**E)$_2$. (d) Solvent accessible surface area of non-polar residues (SASA) for simulations performed using F-peptide (black), KE**FFFF**KE (red), and (K**FF**E)$_2$ (green).

form fibril in our simulations exhibit a non-negligible propensity to adopt helical structures. This includes the A-peptide (see Figure 4.9) and Ac-(K**FF**E)$_2$-NH$_2$.

Figure 4.5a-c shows contact maps of the three peptides studied here computed during the time-frame 2.5-3 μs. For all sequences, interactions are formed with higher probability between pairs of non-polar residues accounting for the dark pattern color in panels a-c. Contacts between charged amino acids occur with a significantly lower probability, which is consistent with the reported low propensity of K and E amino acids for β-structures [100]. In the case of the Ac-(K**FF**E)$_2$-NH$_2$ peptide, charged residues in the middle of the sequence make it difficult for β-structures

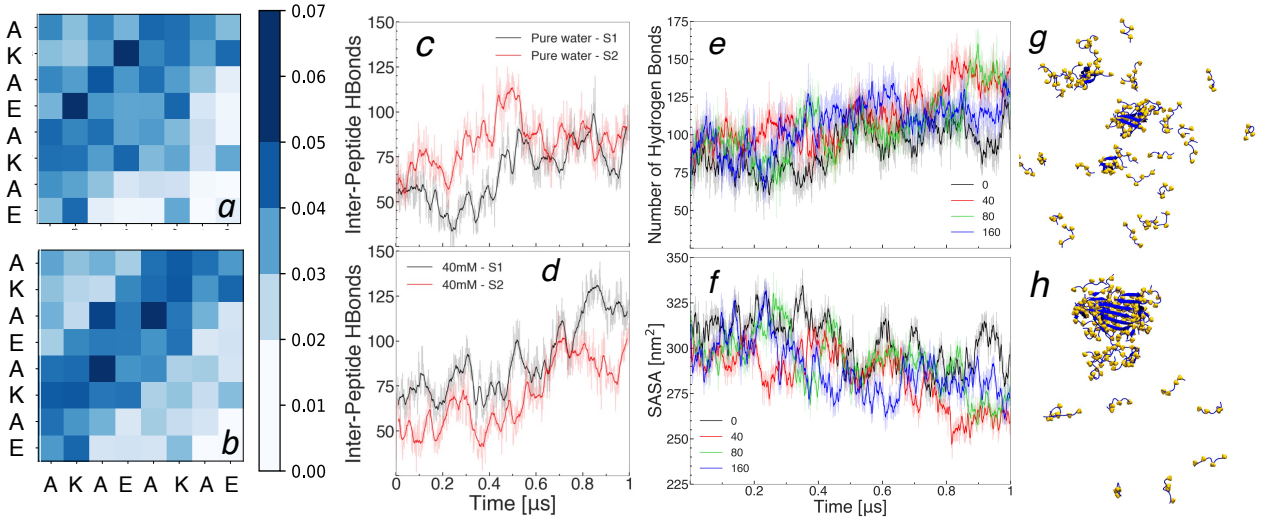

Figure 2.11 Effects of NaCl on aggregation of A-peptides. Contact maps computed within the (a) first and (b) last 500 ns in simulations performed in pure water for trajectory 1 (S_1). Number of inter- hydrogen bonds for trajectory 1 (S_1) in black and trajectory 2 (S_2) in red for simulations performed in (c) pure water and (d) 40 mM NaCl. (e) Number of hydrogen bonds and (f) SASA in simulations performed in different NaCl concentrations for S_1. Final conformations of peptides in simulations performed in (g) pure water, (h) 40 mM NaCl in S_1.

to extend all the way from the N- to the C-terminus. Accordingly, we observe several short β-strands made of only two residues in Figure 2.9f. The solvent accessible surface area (SASA) of non-polar residues for the three-peptides studied here is shown in Figure 4.5d. This quantity decreases continuously for F- and Ac-KE**FFFF**KE-NH_2 sequences as non-polar side chains are buried away from the solvent during the formation of cross-β structures. For the Ac-(K**FF**E)$_2$-NH_2 sequence, SASA decreases during the first 0.4 μs and then it increases during the remaining of the simulation. Combined with results from Figure 2.9, this shows that the Ac-(K**FF**E)$_2$-NH_2 sequence does not form cross-β structure as the number of inter-peptide hydrogen bonds and β-structures is not maximized in the simulation, and SASA is not minimized.

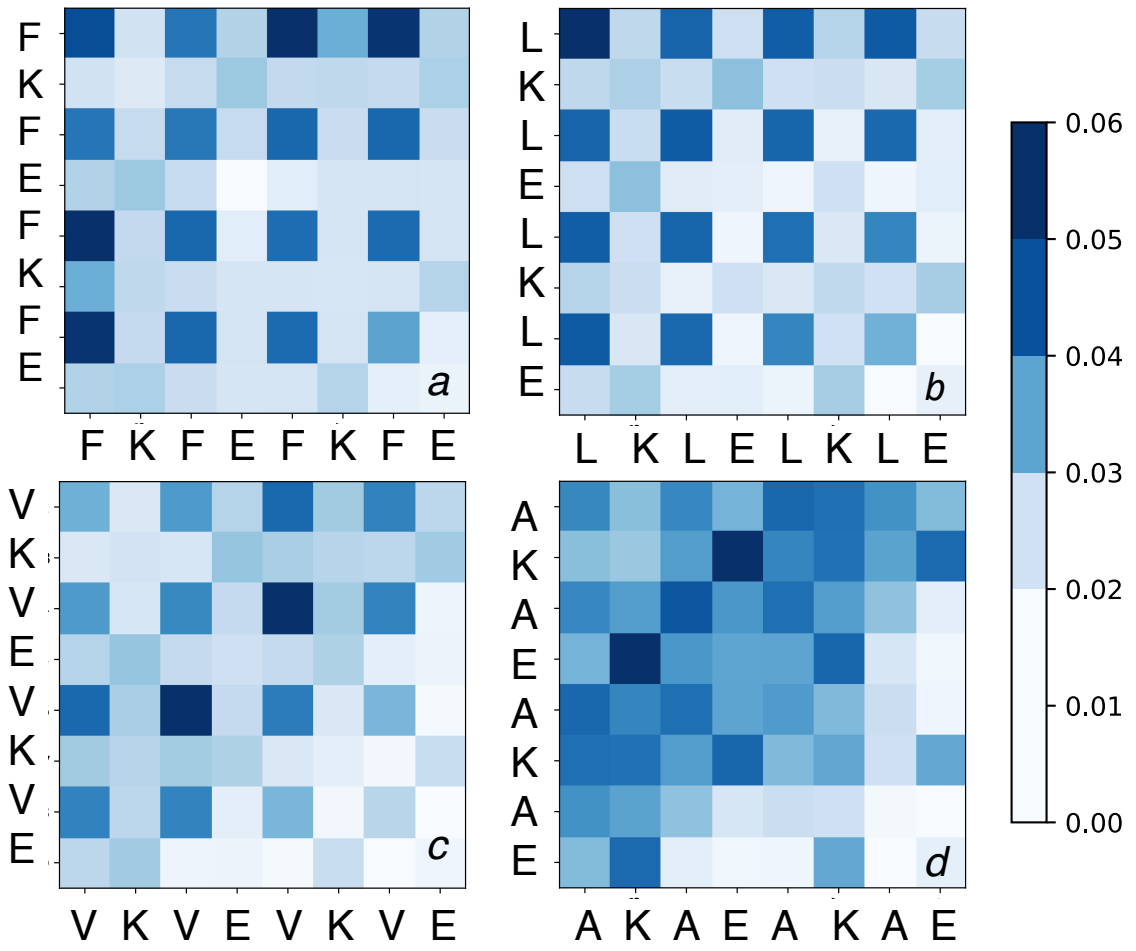

Figure 2.12 Contact maps computed for strictly amphipathic (a) F-, (b) L-, (c) V- and (d) A-peptides in simulations performed at 350K. Only the first 500 ns of the simulations are used in the calculation of contact maps.

2.3.4 Role of electrostatic interactions on fibril formation.

To provide additional insights into the lack of aggregation of the A-peptide, we show in Figure 2.11 contact maps computed over the first (panel a) and the last (panel b) 500 ns in simulations performed at 350 K. These maps show a strong preference for contacts between charged residues in the beginning of the simulation (panel a) and a strong preference for non-polar contacts at the end of the simulation (panel b).

Since, for the more hydrophobic peptides non-polar contacts dominate both the beginning (Figure 2.12) and the end of our simulations (see Figure 4.8), this made us wonder if screening electrostatic interactions for the A-peptide would favor

aggregation. To test this hypothesis, additional simulations of the A-peptide were performed in the presence of NaCl at concentrations of 40, 80, and 160 mM. In panels c and d, we shown the time evolution of the number of inter-peptide hydrogen bonds (i.e., inter-N_{HB}) and SASA in these simulations. Whereas these quantities are subjected to large fluctuations, they highlight a trend in which the addition of NaCl to the solution accounts for a modest increase in inter-N_{HB} and a reduction in SASA, which is consistent with an increase in the propensity of peptides to aggregate. This propensity does not, however, increase monotonically with increasing NaCl concentration as effects of NaCl on aggregation are less pronounced at 160 mM NaCl than at 40 or 80 mM. Nevertheless, at all non-zero NaCl concentrations, inter-N_{HB} and SASA are higher and lower, respectively, compared to simulations performed in pure water solution. Final structures obtained from our simulations in the absence and presence of NaCl are shown in panels e-h. The presence of aggregates is significantly more pronounced in solutions containing 40 or 80 mM NaCl (panels f and g) than at 160 mM (panel h) or 0 mM (panel e). These aggregates consist mainly of β-sheets wherein one face is mostly populated with alanine side chains and the other with charged side chains. In the absence of NaCl, aggregates are mostly nonexistent.

In Figure 2.13, we show contact maps computed for the first 500 ns in simulations performed in pure water, 40, 80, and 160 mM of NaCl. The probability of forming contacts between charged residues is high under conditions in which A-peptides do not form large aggregates, i.e., pure water (panel a) and solution containing 160 mM NaCl (panel d). In contrast, contacts between charged residues are significantly reduced in 40 and 80 mM NaCl solutions where A-peptides form β-sheet aggregates. This is consistent with our hypothesis that electrostatic contacts between side chains contribute to deter the formation of aggregates for A-peptides. Our results are aligned with a previous study on the AEAKAEAKAEAKAE peptide, also known

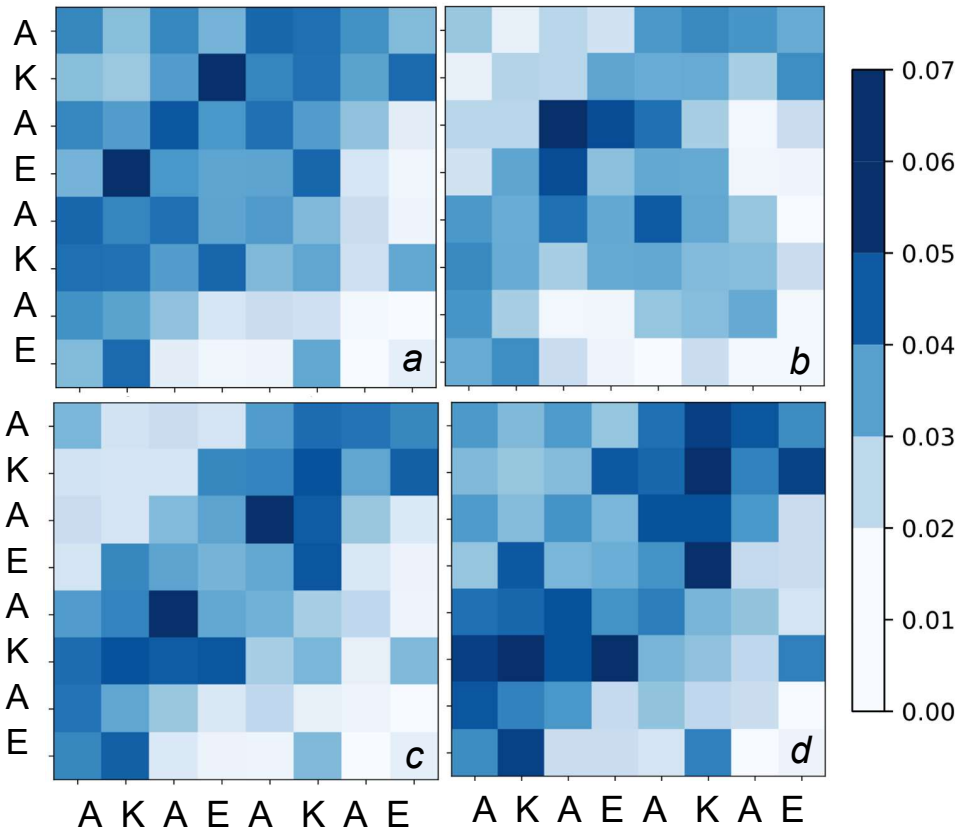

Figure 2.13 Contact maps computed within the first 500 ns of simulations performed using the A-peptide in (a) pure water, (b) 40 mM, (c) 80 mM, and (d) 160 mM NaCl.

as EAK16-I. In this study, the addition of NaCl to the solution at concentrations below 20 mM was shown to promote the self-assembly process into fibrils [79].

2.4 Discussion and Conclusion

In summary, we performed extensive all-atom simulations of strictly amphipathic sequences to study their aggregation into amyloid fibrils. We found that this self-assembly process occurs faster with increasing temperature and the formation of fibrils does not take place if non-polar residues are weakly hydrophobic. This latter result is consistent with experimental studies and points to the important role played by hydrophobic interactions in fibril formation [70, 72]. Moreover, the faster formation of amyloid fibrils with increasing temperature in our simulations can be attributed to the strength of hydrophobic interactions, which increases with increasing temperature [91, 92, 93]. Another important interaction contributing to fibril formation is hydrogen bonding between backbone atoms. As expected, the formation of β-sheets leads to an increase in the number of backbone hydrogen bonds in our simulations. However, if hydrogen bonds were the main (or only) interaction driving fibril formation, all sequences studied here would form fibril as they have identical backbone atoms and, thus, the same potential to form hydrogen bonds [95]. This is consistent with other computational studies wherein the formation of one peptide-peptide hydrogen bonds was shown to be compensated by the rupture of two peptide-water hydrogen bonds and the formation of one water-water hydrogen bond [103, 104]. Also, hydrogen bonds become unstable with increasing temperature [92, 93], which cannot explain the temperature dependent rate of fibril formation in our simulations.

We also found a preference of the peptides studied for the formation of anti-parallel β-sheets. Electrostatic interactions between charged side chains may be responsible for this preference as they can discriminate between parallel and anti-parallel β-sheets. While in simulations where the non-polar residue is only

weakly hydrophobic, i.e., the A-peptide, electrostatic interactions did not contribute favorably to aggregation: screening these interactions by adding salt to the solution produced a modest increase in aggregation. This is consistent with experimental studies on the AEAKAEAKAEAKAE peptide wherein the addition of NaCl to the solution at concentrations below 20 mM was shown to promote fibril formation [79]. In the same vein, in a recent all-atom simulation study of the Aβ protein, the addition of salt to the solution was shown to screen interactions between charged residues in the middle of the protein [96]. This was shown to destabilize the formation of a β-sheet between the central-hydrophobic-core and the central-hydrophilic-core of this protein enabling the formation of the turn region observed in some Aβ fibril structures. This could explain the increased rate of fibril formation of this peptide in the presence of salts [105, 106, 107].

Fibril growth in our simulations proceeded through the displacement of peptides located in the vicinity of the fibril to the tip. Most peptides were extended, e.g., formed a β-strand, when deposited on the fibril tip. This is consistent with another computational study on the aggregation of KFFE peptides in which the formation of β-sheets was suggested to occur in an orderly manner from the beginning to the end of the simulation [76]. However, we also observed the deposition of a peptide that was folded into a β-hairpin. Within 1 μs, this hairpin unfolded to adopt a conformation consistent with the fibril template, i.e., a β-strand. Thus, fibril growth may also take place in a more disordered manner given enough time for conformational defects to relax.

As suggested in previous studies, the sequence pattern determines both the propensity of a peptide to form β-strands as well as its ability to segregate non-polar and charged residues into difference faces of the β-sheet [67]. These two properties of a sequence are prerequisites for the formation of fibrils while the net hydrophobicity is required to stabilize packing of β-sheets into cross-β structures [108, 71, 72, 70]. Here,

we also performed simulations using KE**FFFF**KE and (K**FF**E)$_2$ sequences which are made of the same amino acids as the F-peptide but have different propensity to form β-structures as well as segregate non-polar and charged residues to different faces of a β-sheet. The propensity of these sequences to form β-structures and inter-peptide hydrogen bonds in our simulations correlate with their experimental tendency to form cross-β structures, i.e., F-peptide > KE**FFFF**KE > (K**FF**E)$_2$. This suggests that all-atom simulations could become a powerful method to predict a sequence's propensity to form amyloid fibrils, at least for amphipathic sequences. However, simulations have to be performed for much longer (2–3 μs) than most current all-atom studies (0.5–1 μs) to be able to differentiate between the aggregation propensity of (K**FF**E)$_2$ and KE**FFFF**KE peptides–see Figure 2.9. Note that bioinformatics tools to predict the propensity of peptides to form amyloid fibrils are not always reliable for designed sequences [109, 110]. For example, the order of aggregation predicted using *AGGRESCAN* [111] and *Tango* [112] are KE**FFFF**KE > F-peptide = (K**FF**E)$_2$ and (K**FF**E)$_2$ > KE**FFFF**KE > F-peptide, respectively. The latter predicts the reverse order of aggregation compared to experiments, and AGGRESCAN predicts the same aggregation propensity for (K**FF**E)$_2$, which does not form fibrils in experiments, and the F-peptide that is highly aggregation prone.

CHAPTER 3

GROWTH KINETICS OF AMYLOID-LIKE FIBRILS: AN INTEGRATED ATOMISTIC SIMULATION AND CONTINUUM THEORY APPROACH

Zhang, R., **Jalali, S.**, Dias, C. L., Hattaja M. P., *Growth kinetics of Amyloid-like Fibrils: An Integrated Atomistic Simulation and Continuum Theory Approach*, **equal contributions**, ready for submission.

Amyloid fibrils have long been considered to be closely related to many neurodegenerative diseases. The conventional understanding of the formation and proliferation of the fibrils from unfolded proteins comprises primary and secondary nucleation, elongation and fragmentation. However, the effects of fibril surfaces during these processes are often overlooked, and it is still unclear how surfaces might impact the overall growth kinetics. In Chapter 2 of this dissertation, we showed that MD simulations can reproduce fibril formation of short amphipathic peptides in a realistic manner and provide results that are consistent with experiments. In this chapter, we explore the pathways involved in fibril elongation through collaborative work to quantify the effects of fibril surface, length, diffusion, and attachment kinetics during elongation. In this investigation, we perform all-atom molecular dynamics simulations, while our collaborators established a mesoscale continuum model.

We observe that peptides in the bulk solution can attach and then diffuse on the fibril surface freely, which sometimes leads to fibril elongation via either bulk or surface-mediated docking mechanisms. A mesoscale continuum model is formulated by our collaborators to facilitate the analysis of such events by incorporating bulk-mediated surface diffusion and attachment kinetics during fibril-peptide interactions. By considering physical parameters such as aspect ratio, diffusion coefficients, surface binding rate, residence time, etc., our collaborators explore different regimes of the continuum model in steady state, including diffusion-limited and attachment rate-limited growth. The steady-state bulk and surface peptide density profiles reveal the

boundary layer effects at fibril tips, which can be decoupled from fibril length. Our collaborative results from MD simulations and continuum model provide quantitative evidence that the overall fibril growth rate is determined by both bulk and surface peptide flow rates, enriching our understanding of the growth kinetics of amyloid-like fibrils.

3.1 Introduction

Amyloid fibrils are supramolecular structures formed during the self-assembly of β-sheet rich proteins like amyloid-β, tau, amylin, and α-synuclein [113, 114]. Their presence in human tissues is often indicative of diseases such as Alzheimer's, Parkinson, and type 2 diabetes [115, 116]. At least three mechanisms have been related to the formation of these structures, which are the nucleation of fibril seeds via primary and secondary mechanisms, and the growth of these seeds into micrometer long fibrils [117, 118]. Almost all proteins are incorporated into fibrils via the latter process where they bind to the fibril-ends one peptide at the time [119]. This phenomenon has therefore been a source of intensive interest aimed at controlling the fibril load in diseases [120]. However, the atomic mechanisms and pathways enabling fibril growth are not well understood and require complementary methods that can bridge multiple length scales [121, 122]. In particular, effects of the fibril surface (which plays a critical role in secondary nucleation) remains mostly unknown at the atomic level [123].

The mechanism by which a peptide binds to the fibril ends accounting for its growth is often described by a two-step dock-and-lock process [120]. The dock phase describes the process by which proteins promptly land on the fibril tip, and the lock phase accounts for how they undergo the structural rearrangement enabling them to slowly adopt the conformation established by the fibril template. Two pathways have been envisaged for the locking process wherein docked proteins change their

conformations randomly (constrained only by steric interactions with the tip) or driven by side chain interactions with the fibril [124, 125]. In regards to docking, almost all studies assume that proteins land onto the fibril tip from the solution, i.e., bulk-docking [126, 127, 128]. This assumption is, however, almost never tested as it requires long unbiased simulations whereas most molecular dynamics studies are performed starting with peptides already docked (or even locked) onto the fibril tip.

In recent years, it has been increasingly evident that the fibril surface plays an important role in accounting for the kinetics of the fibril load. In particular, most oligomers that are on pathway to fibril formation are catalyzed at the fibril surface via secondary nucleation [118]. This may emerge from non-specific binding of proteins in solution with the fibril surface [129, 125, 130]. Also, in implicit solvent simulations, Aβ proteins were shown to promptly diffuse on the fibril surface [131]. The latter diffusion could account for an alternative docking pathway where proteins would adsorb onto the fibril surface and diffuse on it until reaching its extremities. Since diffusion on the fibril surface takes place in one-dimension (instead of three-dimension in the bulk), this docking pathways could contribute significantly to fibril elongation. However, to the best of our knowledge, there has never been a direct observation of this pathway or a quantitative estimation of its relevance compared to bulk-docking.

Here, docking pathways are investigated using unbiased all-atom simulations of large systems comprising an amyloid fibril, a peptide, and water molecules. We use a short amphipathic peptide to mimics the alternating stretches of non-polar and polar amino acids in the sequence of amyloid proteins. Independently of the initial position of the peptide in the simulations, we find that it binds and unbinds to the fibril several times before docking to one of its extremity either from the solution or after diffusing on its surface. To guide the interpretation of these simulations and provide a quantitative picture of the growth kinetics of a single fibril, our collaborators formulate a continuum model which incorporates

the essential phenomena observed in our all-atom simulations. This model is used to investigate how relevant physical parameters affect the kinetics of fibril growth. Effects of temperature on these parameters are obtained from all-atom simulations and incorporated into the continuum model to make predictions. Steady-state solutions of the continuum model are consistent with a picture where surface-docking and bulk-docking dominate at low and high temperatures, respectively. Moreover, contributions of the surface-docking pathway to the kinetics of fibril growth at low temperatures are significantly more pronounced for long fibrils compared to small ones. This is due to the capacity of the fibril surface to *store* peptides, which can promptly diffuse to tip. It can be anticipated that determining the cross-over temperature where surface-docking and bulk-docking contribute equally to growth for different amyloid proteins will be critical to identify the pathway that needs to be targeted by drugs to control fibril growth.

3.1.1 Bulk and surface-mediated fibril elongation: Molecular Dynamics simulations

To investigate the different pathways accounting for docking, all-atom simulations were performed with a peptide initially located randomly in space at a distance larger than 2 nm from a pre-formed fibril. The latter consist of two laminated anti-parallel β-sheets made of 10 peptides each–Figure 3.1A. Due to the stochastic nature of fibril elongation, five replicas were studied for each of the conditions studied here. Figure 3.1A provides a schematic representation of the two docking pathways observed in our simulations. In the bulk-docking pathway, the peptide lands on the fibril tip after diffusing in solution. In the surface-docking pathway, the peptide lands on the non-polar surface of the fibril and diffuses on it to reach the fibril tip. Independently of the docking pathway, the peptide is able to lock itself onto the fibril tip reproducing its structure.

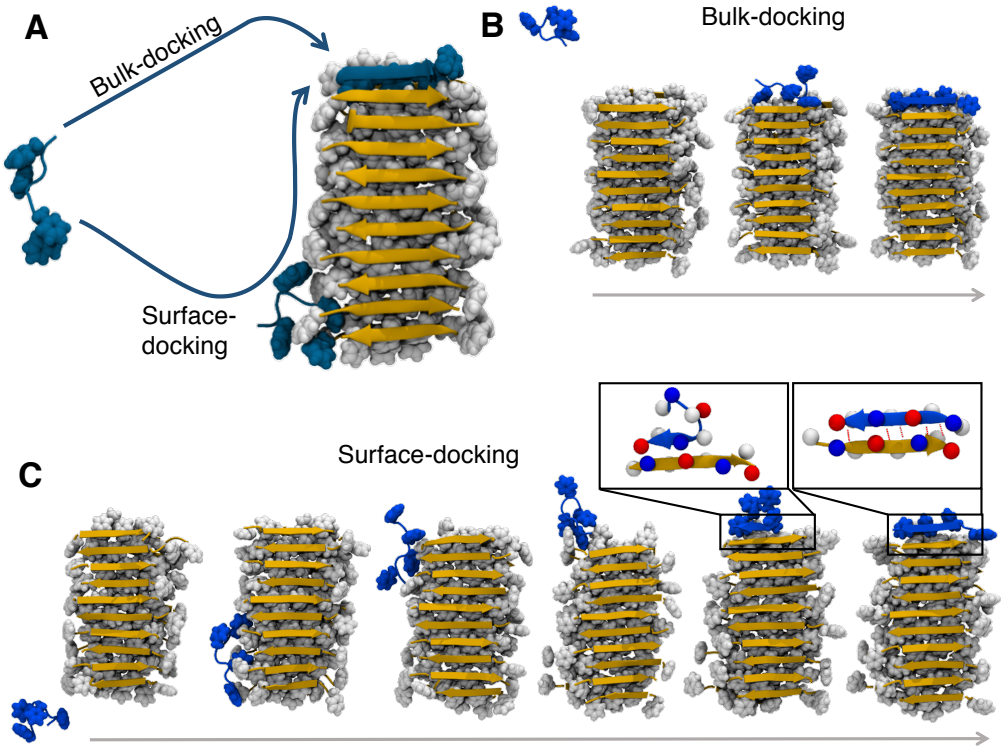

Figure 3.1 A) Schematic representation of the pathways involved in the fibril elongation. Representative trajectories of (B) bulk- and (C) surface-docking pathways where the peptide (in blue) initially in solution binds to fibril tip and surface, respectively. Panel C depicts the diffusion of the peptide along the fibril in the surface-docking pathway. Locking is represented in zoomed regions of panel C where lysine and glutamic acid residues are represented by blue and red beads, respectively. Phenylalanine and backbone of peptides in the fibril are represented in white and orange, respectively.

The peptide locked onto the fibril tip in three out of the five simulations performed at 325 K remaining there without detaching itself until the end of the trajectory–i.e., for $\sim 1\mu$s. In one of these trajectories, the peptide landed on the fibril tip via the bulk-docking pathways. Conformations of the peptide in one of these trajectories is shown in panel B. In two of the trajectories (panel C), the peptide landed on the fibril surface and diffused on it before reaching the tip where it became locked, i.e., the peptide followed the surface-docking pathway.

Our simulations show that non-polar interactions are critical to enable the diffusion-docking pathway. In particular, the peptide interacted with the non-polar edge of the fibril by burying at least one of its non-polar residues away from the solvent while polar faces of the fibril remained depleted of peptides. In the same vein, diffusion on the fibril surface took place via the consecutive formation and rupture of non-polar contacts between peptide and fibril. At the fibril tip, the peptide ended up adopting the structure established by the fibril template, which is an anti-parallel β-sheet with ~ 7 backbone hydrogen bonds formed between peptide and fibril–see panel F. At 325 K, the latter process (independently of the docking pathway) always started with the alignment of either N- or C-terminals of the peptide with the fibril–second to last snapshot in Panel C. This process was driven by the formation of electrostatic interactions between charged side chains, i.e., alignment of positive lysine (in blue) and negative glutamic acid (in red) side chains. Subsequently, the other terminal of the peptide stretched out to also become aligned with the fibril–last snapshot in Panel C.

Surface-docking also emerged as a pathway in fibril elongation in simulations performed at higher temperature, i.e., 350 K–see Figure 3.12c. Similarly for simulations performed using shorter and longer pre-formed fibrils made with 5 and 15 peptides per β-sheet, respectively. We observe that, when the peptide lands on the fibril surface not too far from the tip, docking via surface diffusion takes

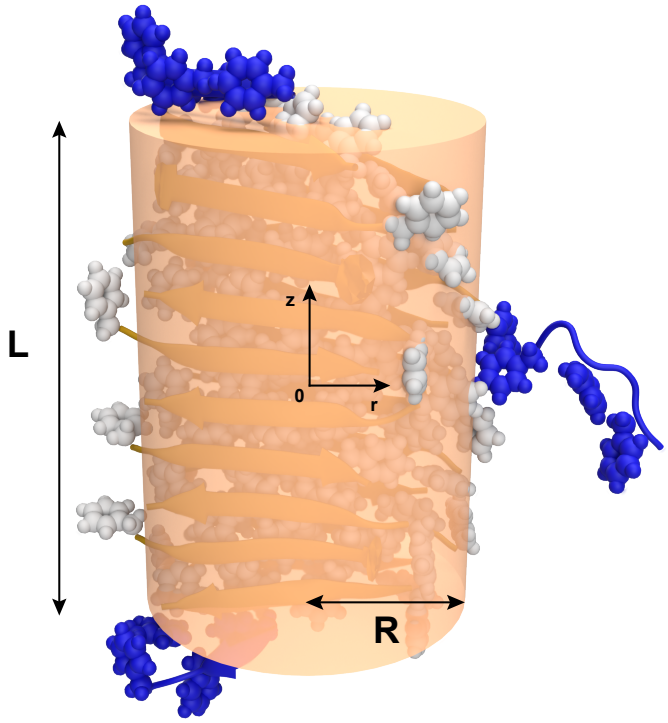

Figure 3.2 Schematic illustration of the geometry of the system. Three peptides (blue) originally in the bulk solution interact with an existing fibril (white and orange). One peptide (right) shows adsorption on fibril surface, and two other peptides are attached to both top and bottom ends of the fibril. The fibril is approximated as a cylinder (orange) to facilitate the theoretical analysis.

place in one step. However, in most cases, docking emerges from a combination of surface and bulk diffusion in which the peptide approaches the tip via consecutive binding-diffusion-unbinding events. Thus, our simulations suggest that the surface-docking pathway, which is currently not appreciated in the literature, could play a significant role in fibril elongation. The importance of this pathway could be even more significant than suggested by our simulations since the fibril surface could behave as a reservoir of peptides accounting for their constant presence close to the tip. To provide a quantitative assessment of the surface-docking pathway and guide the

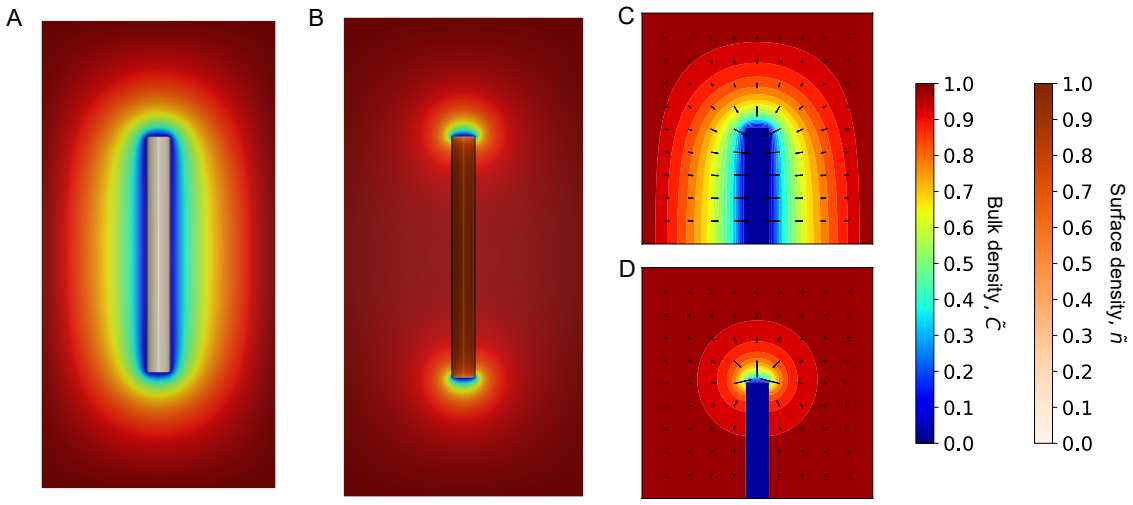

Figure 3.3 Steady-state bulk and surface peptide densities for fibril aspect ratio $\epsilon = 20$. (A) 3D rendering of a slice of $\tilde{C}_{ss}(\tilde{r}, \tilde{z})$ with the cylindrical surface colored with local value of $\tilde{n}_{ss}(\tilde{z})$ for $\Delta = 0.001$. (B) 3D rendering for $\Delta = 1000$. (C) Contour plot of $\tilde{C}_{ss}(\tilde{r}, \tilde{z})$ around the fibril tip in panel (A). (D) Contour plot of $\tilde{C}_{ss}(\tilde{r}, \tilde{z})$ around the fibril tip in (B). Local negative gradients in $\tilde{C}_{ss}(\tilde{r}, \tilde{z})$ are indicated using black arrows.

interpretation of MD simulations, our collaborators now study docking via continuum theory calculations.

3.1.2 Mesoscale model for bulk and surface-mediated fibril growth

The kinetics of fibril growth is traditionally modeled using rate equations [124, 132, 133, 134]. While such models readily yields predictions for size distributions of fibrils during aggregation in homogeneous solutions, all spatial dependence of monomer and oligomer concentrations and the effects of fibril surfaces during growth are ignored. Thus, a more microscopically-informed model is needed to properly incorporate surface effects and quantify how these alter the overall growth kinetics of amyloid fibrils. When considering free peptides that can diffuse in the bulk and intermittently adsorb to a surface on which they can undergo further surface diffusion, the problem belongs to the category of bulk-mediated surface diffusion (BMSD) [135, 136]. In the biological context, such models have been applied to study transcription factors such as the *lac* repressor, which undergoes a diffusional search along DNA to find its specific binding site [137, 138]. Studies have also suggested that the ability to diffuse

on the surface may enhance the rate of adsorbates in finding their target [139]. These theories provide a continuum interpretation to the kinetic processes at atomic level, showing the possibility of bridging the multi-scale processes.

In the continuum model provided by our collaborators, the geometry of a single fibril is approximated by a cylinder with radius R and length L as depicted in Figure 3.2; they return to the merits and deficiencies of this simple approximation in the discussion section. The center of the fibril is positioned at the origin of a cylindrical coordinate system. The fibril is immersed in a bulk solution which has freely diffusing protein peptides quantified by the bulk density, $C(r, z, t)$. On the curved cylindrical surface, assuming axial symmetry, the concentration of adsorbed protein peptides is characterized by the surface density, $n(z, t)$. The time evolution of $C(r, z, t)$ is governed by the diffusion equation

$$\frac{\partial C(r,z,t)}{\partial t} = D_b \left[\frac{1}{r} \frac{\partial}{\partial r} \left(r \frac{\partial}{\partial r} \right) + \frac{\partial^2}{\partial z^2} \right] C(r,z,t), \tag{3.1}$$

where D_b denotes the bulk diffusion coefficient. The peptides on the fibril surface are described by a one-dimensional diffusion equation containing a flux emanating from the bulk [135]:

$$\frac{\partial n(z,t)}{\partial t} = D_s \frac{\partial^2 n(z,t)}{\partial z^2} + 2\pi R D_b \frac{\partial C(r,z,t)}{\partial r}\bigg|_{r=R}, \tag{3.2}$$

with D_s denoting the surface diffusion coefficient. They consider a system with a constant bulk density $C = C_0$ far away from the fibril such that

$$\lim_{r\to\infty} C(r,z,t) = \lim_{z\to-\infty,\infty} C(r,z,t) = C_0. \tag{3.3}$$

The bulk density is in turn coupled to the surface density via a reactive boundary condition [135]

$$\lim_{r\to R,\ -\frac{L}{2}<z<\frac{L}{2}} C(r,z,t) = \mu n(z,t), \tag{3.4}$$

with the coupling constant $\mu = 1/(2\pi R k_b \tau_{\text{off}})$, where k_b denotes the binding rate of peptides from the bulk to the surface while τ_{off} is the average time for adsorbed peptides to unbind from the surface. Furthermore, at the fibril ends, to account for the interplay between diffusive transport of peptides and finite attachment kinetics, our collaborators impose mixed boundary conditions of the form

$$k^b_{\text{on}} C \mp D_b \left.\frac{\partial C}{\partial z}\right|_{r<R, z=\pm\frac{L}{2}} = 0; \tag{3.5}$$

and

$$k^s_{\text{on}} n \pm D_s \left.\frac{\partial n}{\partial z}\right|_{z=\pm\frac{L}{2}} = 0, \tag{3.6}$$

with k^b_{on} and k^s_{on} denoting the attachment rates of peptides from the bulk and surface to the tips, respectively. While there have been reports that show the binding rates at two ends of the fibril may not be identical [127, 140], they ignore any such possible asymmetries and impose reflective boundary conditions at midpoint: $\left.\frac{\partial C(r,z,t)}{\partial z}\right|_{z=0} = \left.\frac{\partial n(z,t)}{\partial z}\right|_{z=0} = 0$. Finally, with the initial conditions $C(r,z,0) = C_0$ and $n(z,0) = n_0$, they have the complete description of a system that incorporates BMSD and the kinetics of specific bindings at the ends of a fibril. The peptides originally in the bulk solution have two pathways to the fibril ends, one via direct binding from the bulk and another via adsorption and surface diffusion. To study the interplay between bulk diffusion, adsorption/desorption, surface diffusion and fibril growth,

our collaborators analytically and numerically explore the steady-state solutions of the coupled transport problem.

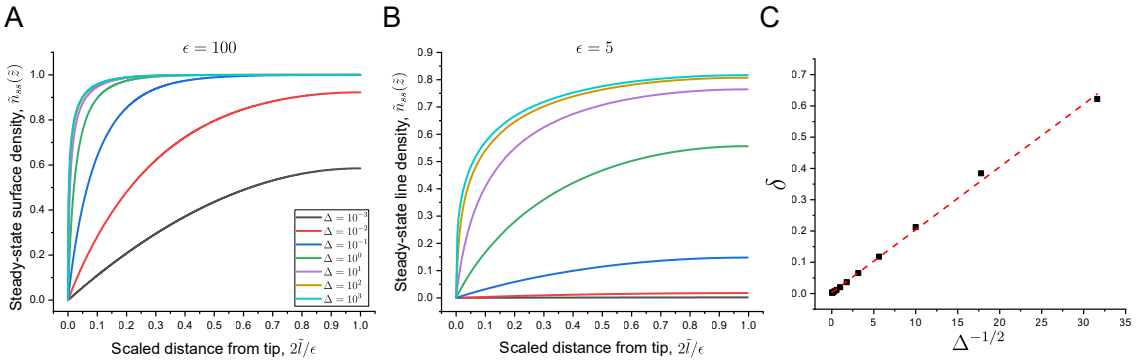

Figure 3.4 Steady-state surface densities for fibril aspect ratios $\epsilon = 100$ (A) and $\epsilon = 5$ (B) over a range of Δ values. (C) Scaled boundary layer width δ vs. $\Delta^{-1/2}$ for $\epsilon = 100$. Red dashed line is a linear fit.

Governing equations in non-dimensional form To solve Equations (3.1) and (3.2) with the corresponding initial and boundary conditions, the model is first non-dimensionalized by defining $\tilde{r} = r/R$, $\tilde{z} = z/R$ and $\tau = D_b t/R^2$. They also define $C_0 = \mu n_0$ such that the dimensionless bulk and surface densities become $\tilde{C}(\tilde{r}, \tilde{z}, \tau) = C(r, z, t)/C_0$ and $\tilde{n}(\tilde{z}, \tau) = n(z, t)/n_0$, respectively. Equations (3.1) and (3.2) in turn become

$$\frac{\partial \tilde{C}(\tilde{r}, \tilde{z}, \tau)}{\partial \tau} = \left[\frac{1}{\tilde{r}}\frac{\partial}{\partial \tilde{r}}\left(\tilde{r}\frac{\partial}{\partial \tilde{r}}\right) + \frac{\partial^2}{\partial \tilde{z}^2}\right]\tilde{C}(\tilde{r}, \tilde{z}, \tau), \tag{3.7}$$

$$\frac{\partial \tilde{n}(\tilde{z}, \tau)}{\partial \tau} = \frac{D_s}{D_b}\frac{\partial^2 \tilde{n}}{\partial \tilde{z}^2} + \frac{R}{k_b \tau_{\text{off}}}\frac{\partial \tilde{C}}{\partial \tilde{r}}\bigg|_{\tilde{r}=\tilde{R}}. \tag{3.8}$$

Our collaborators next define two dimensionless parameters, the fibril aspect ratio $\epsilon = L/R$ and $\Delta = \frac{RD_b}{D_s k_b \tau_{\text{off}}}$, with Δ controlling the interplay between the peptide fluxes along the surface and to/from the surface as will be discussed in more detail shortly. Now, the dimensionless radius of the fibril is scaled to $\tilde{R} = 1$ such that

the dimensionless fibril length $\tilde{L} = \epsilon$. The boundary conditions in turn become $\lim_{\tilde{r}\to\infty} \tilde{C}(\tilde{r},\tilde{z},\tau) = \lim_{\tilde{z}\to-\infty,\infty} \tilde{C}(\tilde{r},\tilde{z},\tau) = 1$, $\lim_{\tilde{r}\to 1,\ -\frac{\epsilon}{2}<\tilde{z}<\frac{\epsilon}{2}} \tilde{C}(\tilde{r},\tilde{z},\tau) = \tilde{n}(\tilde{z},\tau)$, $\tilde{C} = \pm\zeta_b \left.\frac{\partial\tilde{C}}{\partial\tilde{z}}\right|_{\tilde{r}<1,\ \tilde{z}=\pm\frac{\epsilon}{2}}$, and $\tilde{n} = \mp\zeta_s \left.\frac{\partial\tilde{n}}{\partial\tilde{z}}\right|_{\tilde{z}=\pm\frac{\epsilon}{2}}$, where $\zeta_m = \frac{D_m}{k_{\mathrm{on}}^m R}$ denote dimensionless parameters that describe the interplay between attachments kinetics and diffusive transport. Based on reported data on various protein systems that can form amyloid fibrils [134, 141, 142, 143], they estimate that ζ_b varies from $\sim 10^{-1}$ to $\sim 10^6$, thus encompassing both bulk diffusion-limited ($\zeta_b \ll 1$) and attachment kinetics-limited ($\zeta_b \gg 1$) fibril growth regimes.

Now, as briefly alluded to above, the parameter Δ is key in determining the role of the fibril surface on fibril growth kinetics. More specifically, at fixed aspect ratio (or fibril length) ϵ, in the asymptotic limit $\Delta \to 0$, Equation (3.8) together with the boundary conditions at the tip and fibril midpoint imply that, in steady state, $\tilde{n} = 0$ along the fibril surface. In this limit, the whole fibril surface effectively acts as a sink, and hence the surface-mediated peptide flux to the fibril tips scales as L. On the other hand, for finite Δ, boundary layers of width $\delta \sim \Delta^{-1/2}$ are expected to develop at both fibril ends such that $\tilde{n} \to 1$ outside the boundary layers; in this limit, the surface-mediated peptide flux to the fibril tips becomes length-independent. Therefore, at finite $\Delta \ll 1$ they expect a crossover in surface-mediated fibril growth kinetics when the boundary layers become non-overlapping corresponding to $\epsilon^*\Delta^{1/2} \sim 1$. Finally, with regard to bulk-mediated fibril growth, they expect it to be only weakly dependent on Δ via its effect on $\tilde{C}$ through the boundary condition along the fibril surface.

Steady-state behavior I: Diffusion-limited growth To verify and further elucidate the emerging physical picture of the coupled bulk and surface-mediated fibril growth, our collaborators solve Equations 3.7 and 3.8 numerically for the steady-state bulk and surface densities, $\tilde{C}_{\mathrm{ss}}(\tilde{r},\tilde{z})$ and $\tilde{n}_{\mathrm{ss}}(\tilde{z})$, as discussed in *Materials and Methods*.

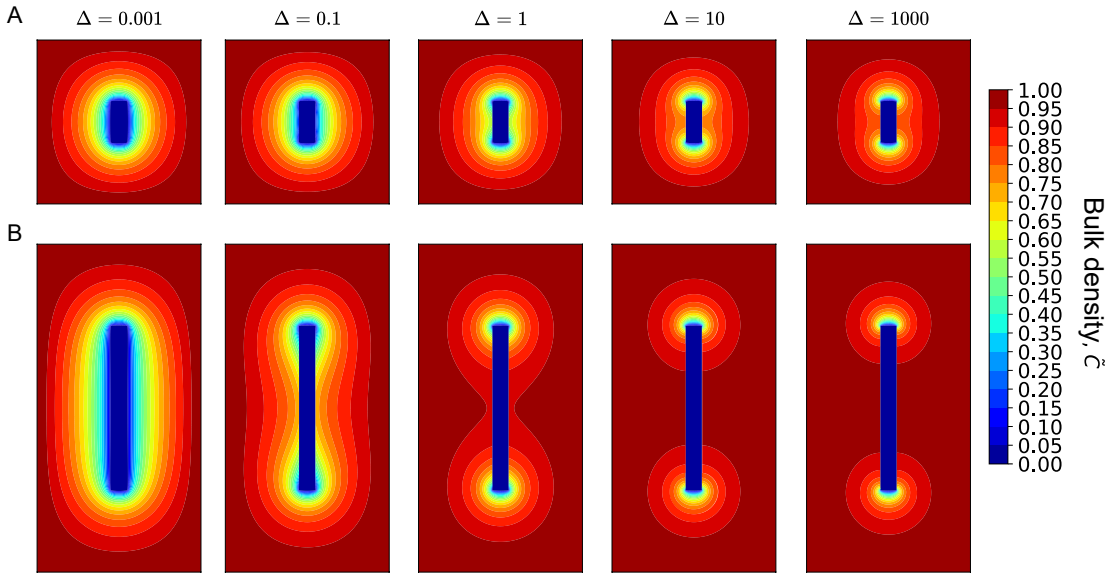

Figure 3.5 Parametric study of the steady-state $\tilde{C}$ profiles for different values of ϵ and Δ at the limit of $\zeta_b = \zeta_s = 0$. (A) $\epsilon = 5$. (B) $\epsilon = 20$. At low Δ values, the fibril surface acts as a sink for peptides, while at high Δ values, surface acts as a reservoir for bound peptides.

They first focus on the diffusion-limited case ($\zeta_b = \zeta_s = 0$), such that any contact between a peptide and the tips leads to the immediate incorporation of the peptide to the growing fibril. This is equivalent to imposing absorbing boundary conditions at the fibril ends: $\tilde{C}(\tilde{r} < 1, \tilde{z} = \pm\frac{\epsilon}{2}) = \tilde{n}(\tilde{z} = \pm\frac{\epsilon}{2}) = 0$. Figures 3.3A and B show three-dimensional renderings of the steady-state solutions for fibrils of length $\epsilon = 20$. A vertical slice of $\tilde{C}_{\text{ss}}(\tilde{r}, \tilde{z})$ through the center of cylinder is illustrated on the plane, while $\tilde{n}_{\text{ss}}(\tilde{z})$ is mapped to the cylindrical surface. For $\Delta = 0.001$ (Figure 3.3A), the bulk density approaches zero at the fibril surface. This case corresponds to the scenario where the entire fibril surface effectively acts as a sink for peptides. Indeed, the local gradients of the bulk density in the vicinity of the fibril tip (Figure 3.3C) imply significant fluxes to both the tip and the surface. For $\Delta = 1000$ (Figure 3.3B), on the other hand, the solution depicts the conventional view of the problem, in which the bulk density only shows variations in regions close to the fibril ends. The gradient field in Figure 3.3D implies that the flux is negligible along the fibril surface, and hence the surface does not significantly contribute to the fibril growth.

The effect of Δ on peptides along fibril surface are further quantified by plotting the steady-state surface density profiles against the scaled distance away from tip, $\tilde{l} \in [0, \epsilon/2]$. For a fibril with high aspect ratio $\epsilon = 100$ (Figure 3.4A), the surface density converges to 1 away from the tip for large Δ values. Also, the slope of the surface density at the tip rapidly increases at large Δ values, approaching a Heaviside step function. Indeed, the gradient of surface density at the tip shows diverging behavior as Δ increase. The dashed line indicates $\tilde{n} = 0.5$, above which indicates leaving the boundary layer close to the tip. The surface density profiles have lower plateau values for shorter fibrils with $\epsilon = 5$ (Figure 3.4B), indicating fewer peptides on the surface during steady-state growth. Different from longer fibrils, the surface density in this case depletes to zero for small Δ. As a result, for $\Delta < 1$, the boundary layer encompasses the entire fibril, while for $\Delta \geq 1$, they will see the variations in surface density. They verify in Figure 3.4C that the boundary layer width δ, here operationally defined as the point at which $\tilde{n}$ reaches 0.5, is indeed proportional to $\Delta^{-1/2}$ for long fibrils, consistent with our scaling argument.

They next discuss the combined effects of the fibril aspect ratio ϵ and Δ on steady-state bulk density profiles. In Figure 3.5, they show contour plots of the steady-state bulk density for two fibrils with different aspect ratios, and compare them for a wide range of Δ values. For $\epsilon = 5$ (Figure 3.5A), the bulk density at the fibril surface is close to zero for small Δ, indicating that the surface acts an effective conduit for transporting peptides to the ends. For $\Delta \gtrsim 1$, the boundary layer effects begin to emerge along the fibril surface, consistent with the transition shown in Figure 3.4B. This effect is amplified for longer fibrils ($\epsilon = 20$ in Figure 3.5B), for which the variations in bulk density are more sensitive to changes in Δ. The contour plot at $\Delta = 0.001$ is similar to the short fibril case, while the boundary layer starts to develop at $\Delta \sim 0.1$, implying less efficient transport of peptides along the fibril surface. Further increasing Δ leads to smaller δ, and the contour lines start

to converge at the two ends. An even longer fibril with $\epsilon = 100$ exhibits similar decoupling behavior at a lower value of $\Delta = 0.001$ (Figure 3.7).

Fibril growth rate I Our collaborators now turn to the implications of the above observations on the fibril growth rate. Specifically, they focus on the net amount of peptides transported to the fibril ends per unit time. Under diffusion-limited conditions considered above, the peptide flux emanating from the bulk to one end of the fibril is given by $j_b(r) = D_b \left.\frac{\partial C}{\partial z}\right|_{z=L/2}$ such that the total amount of peptides incorporated to the growing fibril per unit time ("flow rate") can be determined from $J_b = 4\pi \int_0^R j_b \; r dr$. In steady state, the net amount of peptides that diffuse to the ends along the fibril surface equals the amount of bulk peptides that get adsorbed to the surface, and thus the flow rate of peptides from fibril surface to the fibril ends, J_s, can be readily calculated via $J_s = 2\pi R \int_{-L/2}^{L/2} j_s \; dz$, where $j_s(z) = D_b \, \partial C/\partial r|_{r=R}$. To illustrate how the flow rates change in the parametric study, they focus on the dimensionless flow rates $\tilde{J}_b = J_b/(RD_bC_0)$ and $\tilde{J}_s = J_s/(RD_bC_0)$, as well as the total flow rate $\tilde{J}_{\text{total}} = \tilde{J}_b + \tilde{J}_s$. These flow rates are shown in Figure 3.6 for several representative values of ϵ and Δ. For a short fibril with $\epsilon = 5$ (Figure 3.6A), the trend shows that $\tilde{J}_s$ decreases with increasing Δ, whereas $\tilde{J}_b$ increases. $\tilde{J}_s$ is the main source for the total flow rate at small Δ values, which agrees with our prior understanding that peptides on the fibril surface are instantly transported to the ends. As Δ increases, the discrepancy between $\tilde{J}_s$ and $\tilde{J}_b$ diminishes, and then $\tilde{J}_b$ becomes the main contribution to the total flow rate. For longer fibrils with $\epsilon = 20$ (Figure 3.6B) or $\epsilon = 100$ (Figure 3.6C), $\tilde{J}_s$ is at least one order of magnitude higher than $\tilde{J}_b$ at small Δ. They observe that for distinct ϵ values, $\tilde{J}_s$ consistently intersects with $\tilde{J}_b$ at around $\Delta = \sqrt{10}$, suggesting that the main mechanism for fibril growth switches from surface to bulk diffusion.

The value of $\tilde{J}_b$ is almost insensitive to any change in ϵ (Figure 3.6D), showing a consistently increasing behavior as Δ increases. Unlike $\tilde{J}_b$, as illustrated in

Figure 3.6E, the flow rate from the fibril surface is highly dependent on both ϵ and Δ. In the low Δ regime, the extra surface areas of long fibrils can amplify the peptide adsorption rate from the bulk and efficiently transport the surface peptides to the fibril ends, thus the longer the fibril, the higher the flow rate. $\tilde{J}_s$ becomes length-independent in the regime $\Delta \geq 1$, as the curves of various aspect ratios collapse into one. They observe that for each Δ, there exists a critical aspect ratio ϵ^*, above which the fibril experiences a constant flow rate from the surface. For example, for $\Delta = 10^{-2}$, the surface flow rate starts to saturate for $\epsilon > 50$, thus a critical aspect ratio of $\epsilon^* = 50$ (green). For $\epsilon < \epsilon^*$, the fibril has an increasing flow rate, indicating accelerated growth. The inset shows that as Δ approaches zero, ϵ^* goes to infinity, and as Δ increases, ϵ^* goes to zero. To further highlight the transition from accelerated to constant growth velocity, they illustrate in Figure 3.6F that for small $\Delta = 10^{-2.5}$ (red), a short fibril will grow with acceleration due to the increasing surface flow rate as the fibril gets longer; for $\Delta = 10^{-1}$ (yellow dashed line), the fibril will only grow with acceleration for a brief moment and reach steady state once the fibril length exceeds $\epsilon^* = 10$; for $\Delta \geq 1$, which is not shown in the figure, the fibril reaches steady state during the very early stage of growth, because the growth is completely determined by bulk diffusion. The steady-state velocity of the fibril increases with decreasing Δ values, as longer fibrils have higher flow rate from the fibril surface, especially in the low Δ regime. Studies have shown that the short and soluble oligomers produced by both primary and secondary nucleation processes exhibit more toxicity than the long and insoluble fibrils [144, 145], suggesting the important role of early-stage growth kinetics in the spreading of the pathology. If in the low Δ regime, the accelerated growth of oligomers with $\epsilon < \epsilon^*$ may lead to rapid depletion of the surrounding peptides, potentially affecting biological functions in cells.

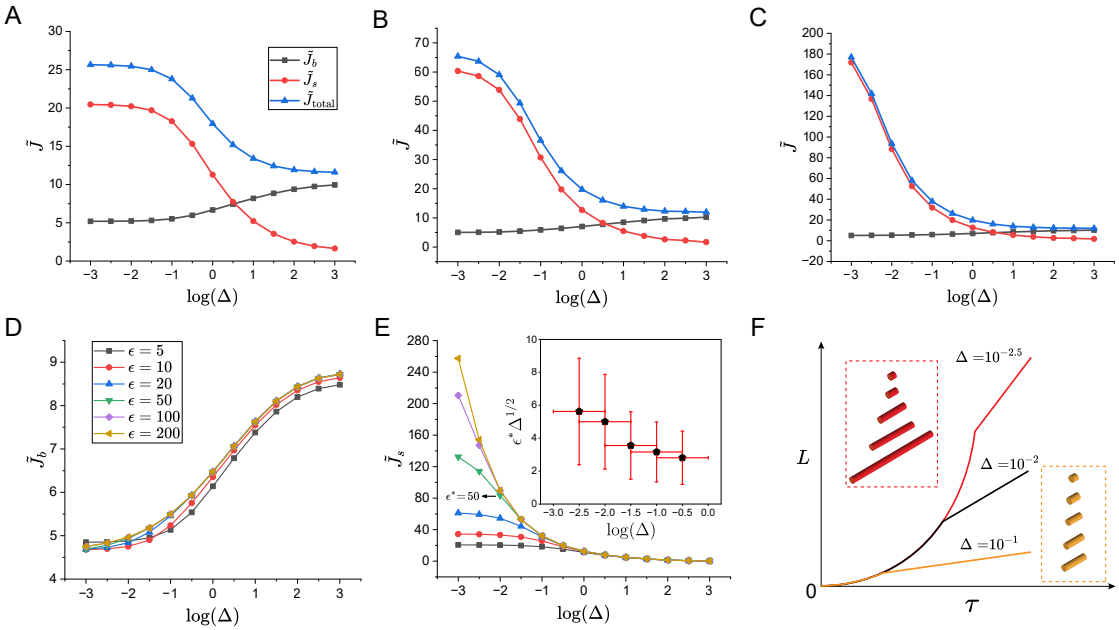

Figure 3.6 Steady-state flow rate of protein peptides to the fibril ends via bulk and surface diffusion for different values of ϵ and Δ. (A) $\epsilon = 5$. (B) $\epsilon = 20$. (C) $\epsilon = 100$. (D) Flux to the ends of the fibril from bulk diffusion. $(Inset)$ Critical aspect ratio (ϵ^*) for different Δ values. (E) Flux to the ends of the fibril from surface diffusion. (F) Total flux to the ends of the fibril with schematic showing different growth kinetics at $\Delta = 10^{-2.5}$ and $\Delta = 10^{-1}$.

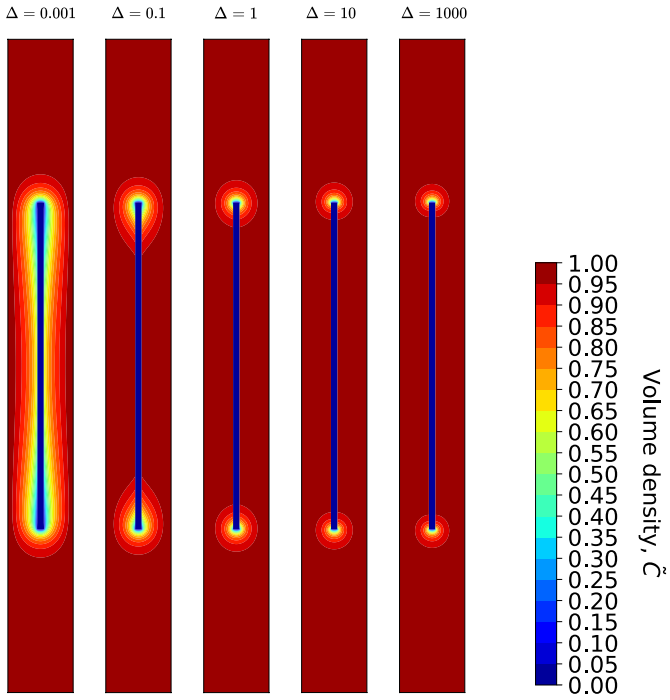

Figure 3.7 Steady-state $\tilde{C}$ profiles for $\epsilon = 100$ for different values of Δ.

Steady-state behavior II: Attachment rate-limited growth from bulk; diffusion-limited growth from surface They now discuss the scenario where the binding of bulk peptides is attachment rate-limited ($\zeta_b \to \infty$) while the binding of surface peptides remains diffusion-limited ($\zeta_s \to 0$), corresponding to the boundary conditions $\partial\tilde{C}/\partial\tilde{z}\,|_{\tilde{r}<1,\tilde{z}=\pm\epsilon/2} = 0$ and $\tilde{n}(\tilde{z} = \pm\epsilon/2) = 0$. They first show the combined effects of the fibril aspect ratio ϵ and Δ on steady-state bulk density profiles in Figure 3.8. At the fibril tips, there is now a finite bulk density of peptides, and the bulk density always increases with increasing Δ. Similar to the diffusion-limited case, the bulk density approaches zero at the fibril surface for small Δ, indicating the effective transport of surface peptides to tips. At $\Delta = 1$, the boundary layer effects start to show in the bulk density for fibril with $\epsilon = 5$. For a longer fibril ($\epsilon = 20$ in Figure 3.8B), the same effects emerge at $\Delta \lesssim 0.1$, showing the length-dependent surface property in steady-state growth.

Fibril growth rate II While the steady-state surface flow rate J_s can be calculated by the same definition as in the diffusion-limited case, the flow rate at the tips from bulk peptides is now redefined as $J_b = 4\pi \int_0^R k_{\text{on}}^b C r\, dr$, showing attachment-rate dependence. When plotting the non-dimensional flow rates $\tilde{J}_b = \frac{J_b}{k_{\text{on}}^b C_0 R^2}$ and $\tilde{J}_s$ together, they observe that in the small Δ regime, $\tilde{J}_b$ is eight times greater than $\tilde{J}_s$ for short fibrils with $\epsilon = 5$ (Figure 3.9A), showing the dominance of bulk attachments of peptides comparing to surface diffusion in fibril growth. As Δ increases, $\tilde{J}_b$ increases in a sigmoidal curve, while $\tilde{J}_s$ declines to zero, and $\tilde{J}_{\text{total}}$ increases monotonically overall. For a very long fibril (e.g. $\epsilon = 200$), $\tilde{J}_s$ becomes slightly greater than $\tilde{J}_b$ as $\Delta \to 0$. As a result, there is a crossover of bulk and surface flow rate at low Δ, and $\tilde{J}_{\text{total}}$ is not monotonically increasing or decreasing with greater Δ values. They observe that $\tilde{J}_b$ stays almost invariant at different aspect ratios, similar to the diffusion-limited case but with a 40-fold increase in magnitude (Figure 3.6D). Moreover, $\tilde{J}_s$ in Figure 3.9C

shares the same behavior as the diffusion-limited case (Figure 3.6E), as the governing equation and boundary conditions for surface peptides remain unmodified.

They note that the crossover behaviors shown in both this limit and the diffusion-limited case are not necessarily indicative of changes in growth mechanisms in a real system due to non-dimensionalization. In order to gain more understanding in the growth kinetics of amyloid-like fibrils in a particular system, one should determine the dimensional bulk and surface flow rates J_b and J_s, respectively, and make comparisons.

Steady-state behavior III: Attachment rate-limited growth from bulk and surface Finally, let us discuss the case for which the fibril growth is attachment rate-limited from both bulk and surface. In this case, the bulk density is always at C_0 while the surface density equals C_0/μ in steady state. The total flow rate to the tips can be easily obtained as $J_{\text{total}} = k_{\text{eff}} C_0$, where $k_{\text{eff}} = 2\pi R^2 k^b_{\text{on}} + 2k^s_{\text{on}}/\mu$. They note that J_{total} is independent of fibril length.

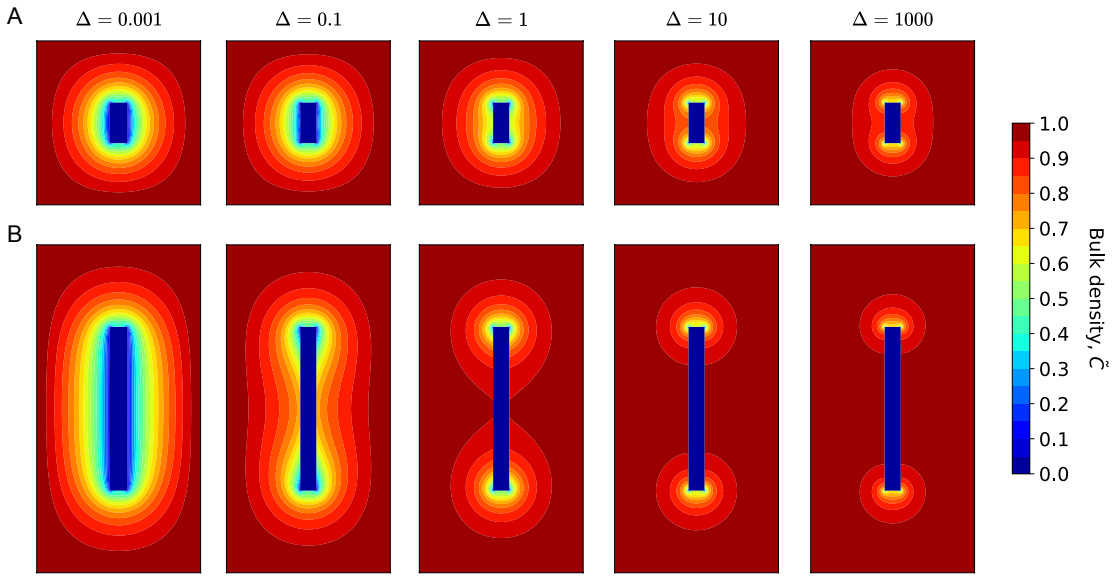

Figure 3.8 Parametric study of the steady-state $\tilde{C}$ profiles for different values of ϵ and Δ at the limit of $\zeta_b \to \infty$ and $\zeta_s = 0$. (A) $\epsilon = 5$. (B) $\epsilon = 20$.

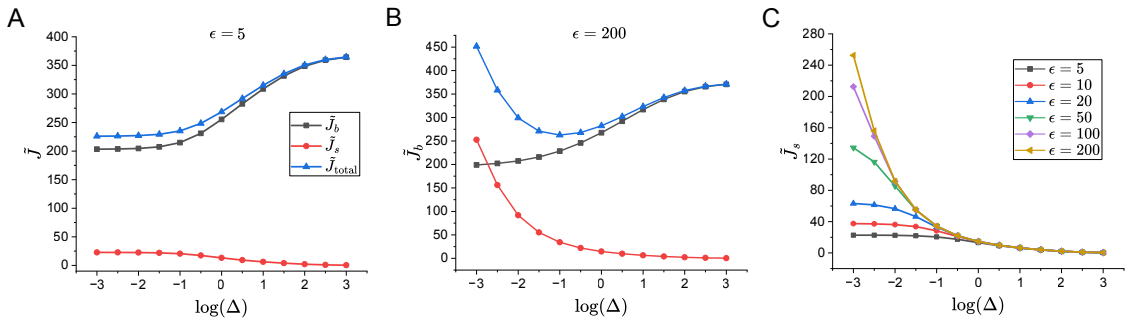

Figure 3.9 Bulk and surface flow rates for different values of ϵ and Δ at the limit of $\zeta_b \to \infty$ and $\zeta_s = 0$. (A) $\epsilon = 5$. (B) $\epsilon = 200$. (C) Surface flow rate to the tips for different aspect ratios.

3.2 Results

3.2.1 Estimation of physical quantities from MD simulations

Simulation setup The pre-formed fibril is made by packing non-polar faces of two antiparallel β-sheets against each other. The peptide is inserted randomly in the simulation box at a distance greater than 2 nm from the fibril. The peptide sequence consists of a strictly alternating pattern of non-polar (phenylalanine F), and polar (glutamic acid E, and lysine K) amino acids, i.e., Ac-$(FKFE)_2$-NH_2–see Figure 3.11.

To investigate different scenarios of fibril growth, simulations are performed at three temperatures (i.e., 298 K, 325 K, and 350 K) and using fibrils differing in their length. Short, medium, and long fibrils are made with β-sheets containing 5, 10, and 15 peptides. This accounts for ϵ values of 1.79, 3.86, and 5.29, respectively. For each temperature and fibril length, simulations are repeated at least five times due to stochastic nature of the dock-and-lock mechanism. Table 3.1 provides a summary of the simulations carried out in this study.

Determining the state of the peptide The peptide in the simulation box can be found solvated, bound to the fibril at its surface or at its tip. To distinguish between solvated and fibril-bound states, the minimum distance between pairs of peptide-fibril atoms is computed for each trajectory. This quantity is shown in red in Figure 3.12.

A

Model Parameters	298 K	325 K	350 K
$k_b\,(\mathrm{ms}^{-1})$	6.32 ± 1.00	$7.72^{+3.70}_{-1.23}$	$9.05^{+1.59}_{-2.20}$
$k^b_{\mathrm{on}}\,(\mathrm{ms}^{-1})$	0.0042	0.01	$0.011^{+0.006}_{-0.005}$
$k^s_{\mathrm{on}}\,(\mathrm{ms}^{-1})$	–	0.0024 ± 0.00028	$0.018^{+0.011}_{-0.0048}$
$\tau_{\mathrm{off}}(\mathrm{ns})$	$41.56^{+47.74}_{-20.38}$	$16.22^{+27.13}_{-10.42}$	$10.00^{+7.78}_{-8.44}$
$D_s\,(\mathrm{m}^2\mathrm{s}^{-1})$	$(4.32 \pm 1.38) \times 10^{-12}$	$(2.00 \pm 0.46) \times 10^{-11}$	$(3.04 \pm 0.87) \times 10^{-11}$
$D_b\,(\mathrm{m}^2\mathrm{s}^{-1})$	$(5.52 \pm 0.27) \times 10^{-10}$	$(8.20 \pm 0.10) \times 10^{-10}$	$(1.10 \pm 0.03) \times 10^{-9}$
Δ	$0.71^{+1.74}_{-0.52}$	$0.46^{+1.55}_{-0.36}$	$0.56^{+6.25}_{-0.36}$
ζ_b	$93.88^{+4.59}_{-4.59}$	58.57 ± 0.71	$71.43^{+63.10}_{-26.58}$
ζ_s	–	$5.96^{+2.34}_{-1.86}$	$1.21^{+0.90}_{-0.67}$

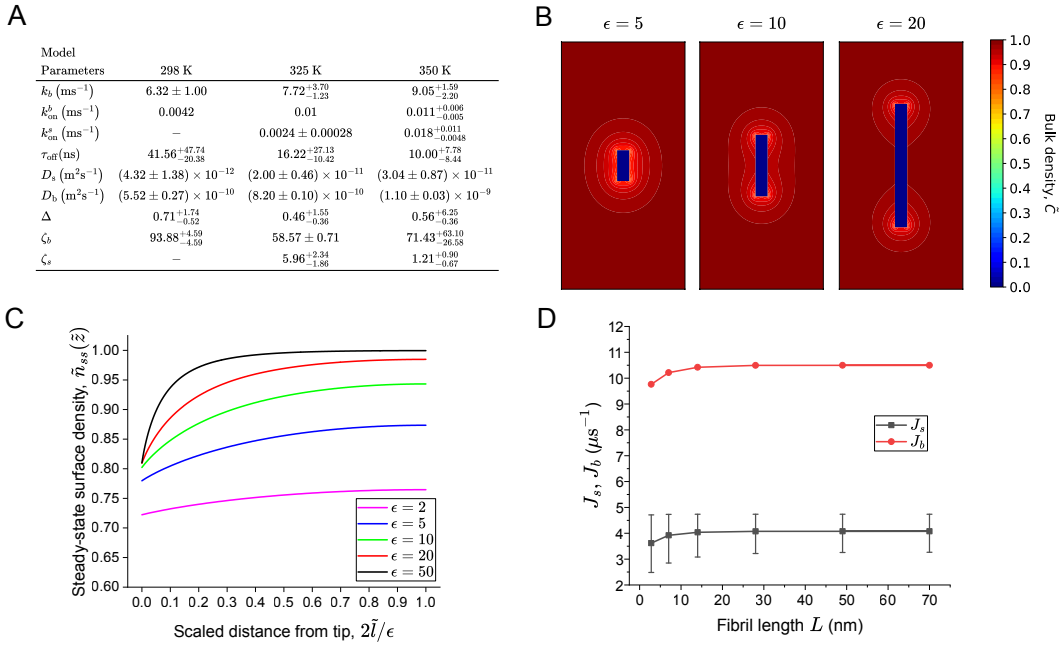

Figure 3.10 (A) Computed physical quantities from MD simulations for fibril with $\epsilon = 3.86$ at 298 K, 325 K and 350 K, from which we compute the corresponding dimensionless parameters Δ, ζ_b and ζ_s. (B) Steady-state bulk density contour plots at the limit of $\zeta_b \to \infty$ and $\zeta_n \to 0$ for ϵ= 5 (left), ϵ=10 (middle) and ϵ=20 (right) using Δ measured at 325 K. (C) Steady-state surface density for the fibril with $\epsilon = 2$, 5, 10, 20 and 50. (D) Steady-state bulk and surface flow rates to tips when the fibril elongates from 2.8 to 70 nm.

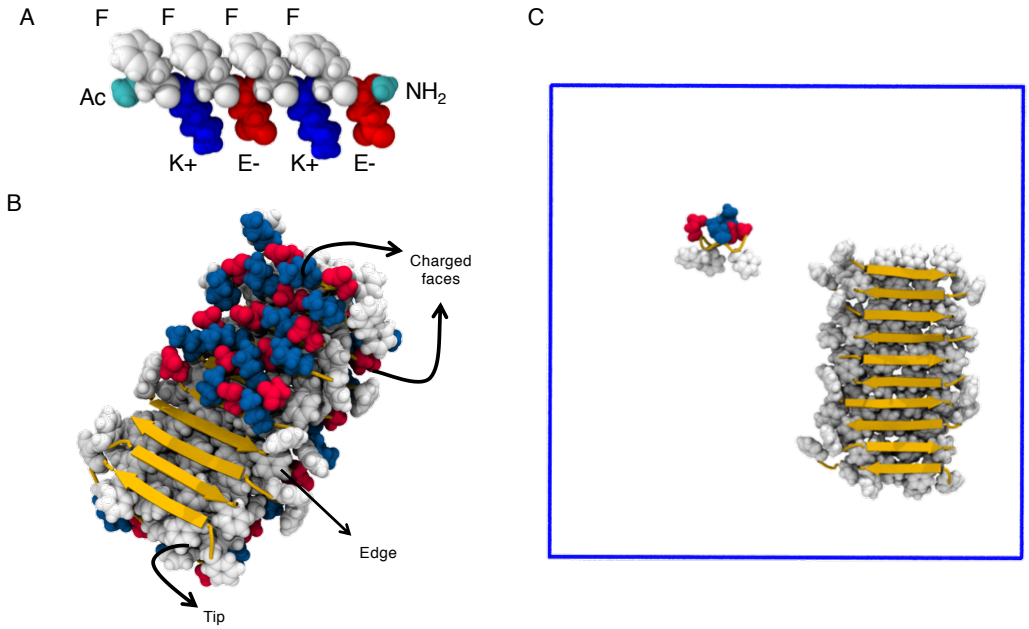

Figure 3.11 (*A*) Schematic representation of the atomic structure of the strictly alternating amphipathic Ac-(FKFE)$_2$-NH$_2$ peptide. (*B*) Cross-β structure made of two laminated β-sheets with a dry core and two solvent exposed polar faces. White, red, and blue colors are used to indicate phenylalanine, i.e., F, glutamic acid, i.e., E, and, lysine, i.e., E, respectively. (*C*) Simulation box containing a pre-formed fibril and a peptide. Water molecules are not shown for clarity.

A cut-off distance of 0.3 nm is used to determine if the peptide is bound to the fibril or solvated. To distinguish between edge- and tip-bound states, the minimal distance between center-of-mass (COM) of fibril and atoms of the peptide is also computed and it is shown in blue in Figure 3.12. Whenever the peptide is bound to the medium-length fibril with a COM-distance greater than 2 nm (see dashed lines), it is found to be bound to its tip. For all other COM-distance in which the peptide is bound to the fibril, it is defined as surface-bound.

The two distances computed in Figure 3.12 allows us to determine the state of the peptide at any given time. Accordingly, we find that one, three, and all trajectories simulated at 298 K, 325 K, and 350 K end up with the peptide locked onto the fibril–see Figure 3.12. Note that trajectories in which the peptide does not lock onto the tip were extended to more than 2.5 μs. Minimal and COM distances also

Table 3.1 Number of Simulations Performed at Different Temperatures and for Fibrils with Different Aspect Ratio, i.e., $\epsilon = L/R$. The Approximate Time of the Simulations is Indicated in Microseconds.

Temp. / ϵ	298 K	325 K	350 K
1.79	—	5 ×0.5 μs	5 ×0.5 μs
3.86	5 ×4 μs	5 ×1.5 μs	7 × 1.5 μs
5.29	—	5 ×1 μs	5 ×1 μs

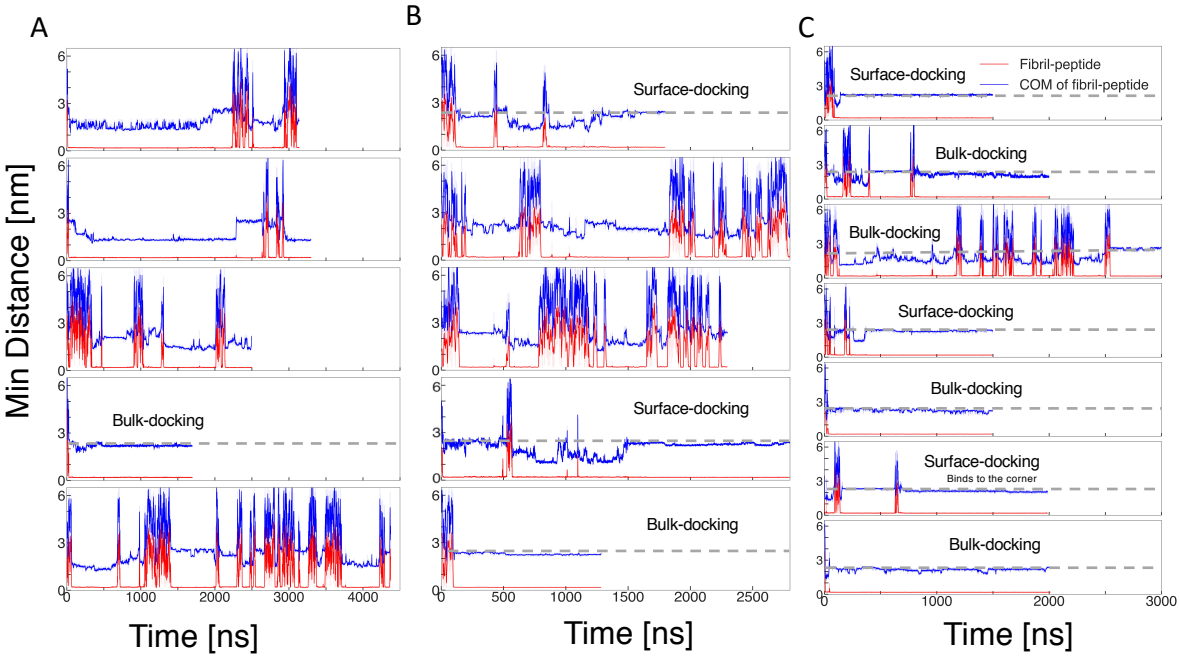

Figure 3.12 Simulations performed with medium-length fibril, i.e., $\epsilon = 3.86$. Minimal distance between peptide-fibril atoms (in blue) and minimal distance between COM of the fibril and atoms of the peptide (in red) computed at a) 298 K, b) 325 K, and c) 350 K. Dashed lines indicate tip-bound states.

allow us to determine the path taken by the peptide to reach the tip. For example, in the first trajectory at 325 K, the peptide lands on the fibril surface at ∼750 ns (i.e., its COM distance is smaller than 2 nm). This is followed by the diffusion of the peptide, which does not detach itself from the fibril surface, until it reaches the fibril tip. This characterizes the surface-docking pathway. The last trajectory at 325

K provides an example of bulk-docking pathway. Distances for short and long fibrils are depicted in Figures 3.14–3.13.

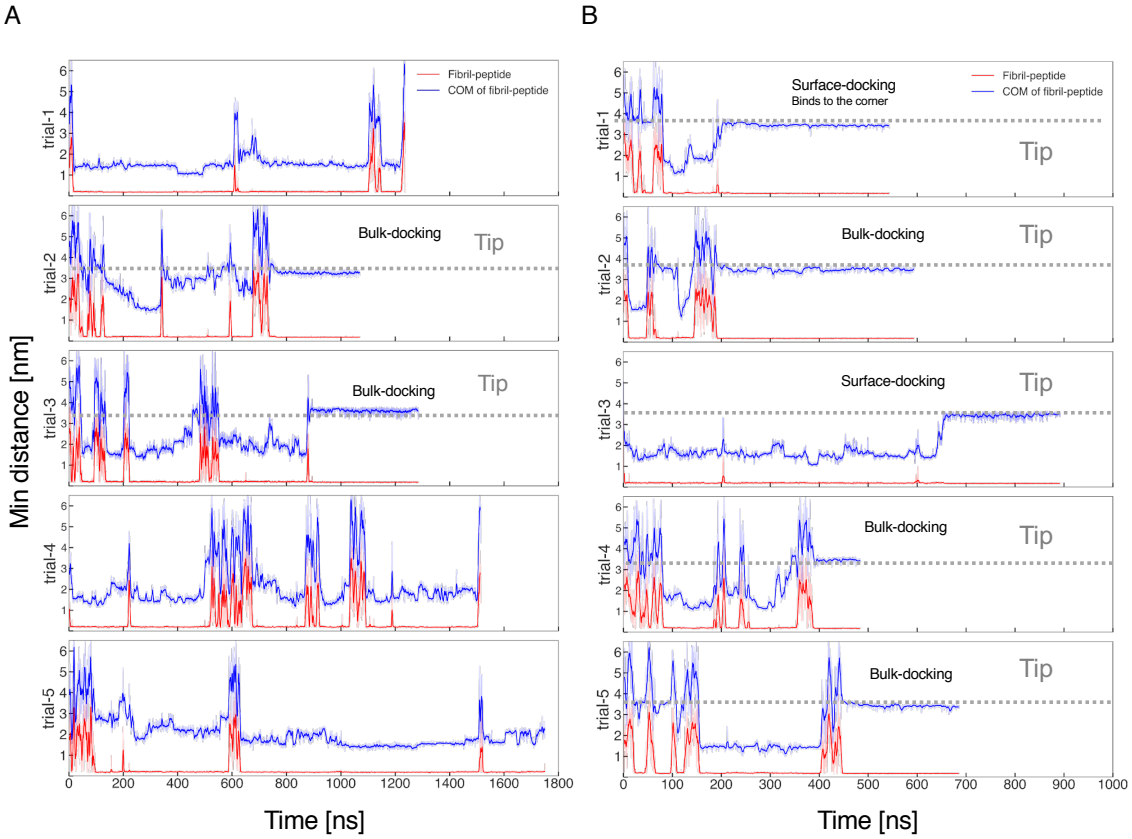

Figure 3.13 Simulations performed with long fibrils, i.e., $\epsilon = 5.29$. Minimal distance between peptide-fibril atoms (in blue) and minimal distance between COM of the fibril and atoms of the peptide (in red) computed at (A) 325 K, and (B) 350 K. Dashed lines indicate tip-bound states.

Table 3.2 summarizes the number of trajectories in which the peptide locks onto the tip via a bulk- and surface-docking pathway. This table shows that, at almost all temperatures, surface-docking is as an important pathway as bulk-docking.

The average time between consecutive binding and unbinding events to the fibril surface accounts for τ_{off}, i.e., the residence time. The average value of τ_{off} was evaluated over each trajectory. Finally, the average values of multiple trajectories and the corresponding standard deviations were reported at each temperature.

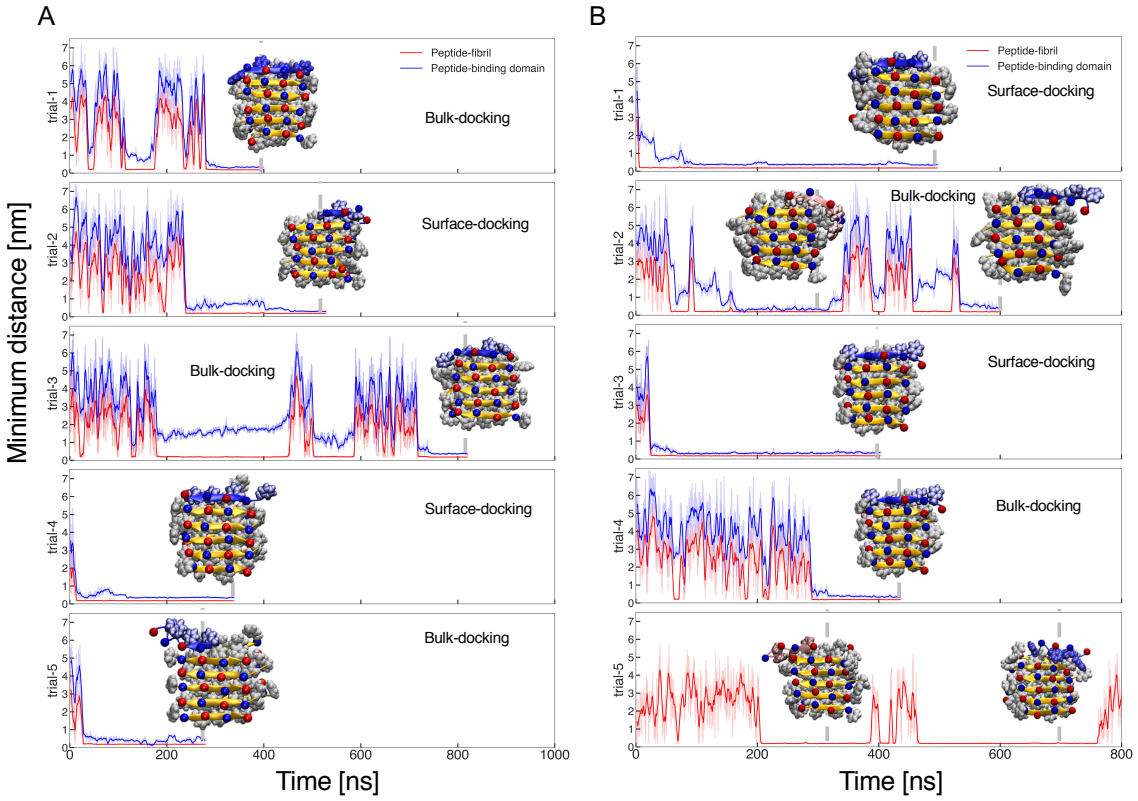

Figure 3.14 Simulations performed with short fibrils, i.e., $\epsilon = 1.79$. Minimal distance between peptide-fibril atoms (in red) and minimal distance between the peptide and targeted tip, i.e., final binding spot (in blue) computed at (A) 325 K, and (C) 350 K. The locked conformation of the peptide with lysine and glutamic acid represented by blue and red balls, respectively, are shown.

Diffusion coefficient computed from MD simulations The diffusion coefficient D_b is estimated in our simulations from the mean square displacement (MSD) of the peptide's COM via Einstein's relation

$$D_b = \frac{1}{2d} \lim_{t\to\infty} \langle (\vec{r}(t) - \vec{r}(0))^2 \rangle,$$

where d denotes the dimensionality of the system, and $\vec{r}$(t) corresponds to the position of the center-of-mass (COM) of the peptide at time t. Independent segments of our trajectories in which the peptide is adsorbed onto the fibril surface are used to compute D_s. To obtain D_b, three additional simulations were performed in large

Table 3.2 Number of Trajectories in Which the Peptide Followed Bulk- and Surface-docking Pathways before Locking onto the Tip.

Temp. / ϵ	298 K		325 K		350 K	
	Bulk-	Surface-	Bulk-	Surface-	Bulk-	Surface-
1.79	—	—	3	2	2	2
3.86	1	0	1	2	4	3
5.29	—	—	2	0	3	2

solvated boxes without the presence of a fibril. Figure 3.15 shows the MSD of the peptide in simulations performed with medium-length fibril at 298 K, 325 K, and 350 K. The average MSD is shown in red and the black dashed line corresponds to the line of best fit of this average [146, 147, 85]. Figure 3.16 shows D_{s} computed for the long fibril at 325 K and 350 K. The computed diffusion coefficients from our simulations is shown in Figure 3.10A.

Rate constants from MD simulations The rate with which the peptide locks onto the tip from bulk is defined as

$$k_{\mathrm{on}}^{b} = \frac{V_b}{A_{\mathrm{tip}} t_b},$$

where V_b corresponds to the relevant bulk volume around the tip shown by hemispheres in Figure 3.17A, A_{tip} is the area of both tips, and t_b is the total time the peptide spends in the hemispheres before locking onto the tip. A radius of 2 nm is used to compute the relevant bulk volume and the area of the tip. In the same vein, the rate with which the peptide locks onto the tip from the surface is defined as

$$k_{\mathrm{on}}^{s} = \frac{l_b}{t_s},$$

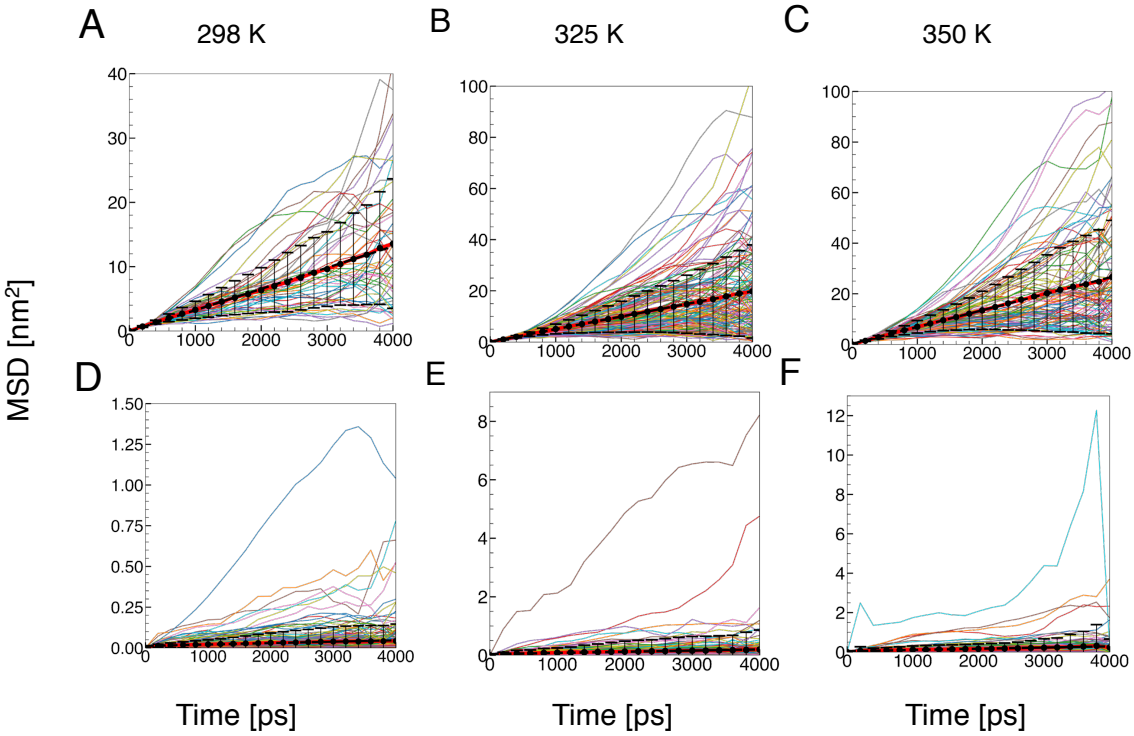

Figure 3.15 Mean square displacement (MSD) of the peptide's COM in bulk solution at A) 298 K, B) 325 K, and 350 K. The MSD of the peptide's COM as it diffuses on the fibril surface is shown at D) 298 K, E) 325 K, and F) 350 K. The mean MSD is shown in red and the error bars denote the standard deviation. The linear fit of the average MSD is represents using black dashed lines.

where l_b denotes distance from the tip (see Figure 3.17A), and t_s is the total time the peptide spends on the fibril and within the range.

All trajectories in which the peptide locks onto tip were used to compute k^b_{on} and k^s_{on} values. For the medium-length fibril, this includes seven trajectories at 350 K, three at 325 K, and one at 298 K–see Table 3.2.

The binding rate of the peptide to the fibril surface, i.e., k_{b}, is computed by

$$k_{\text{b}} = \frac{N}{tA_{surface}C},$$

where N is the number of binding events to the surface, t corresponds to the time the peptide spends close to the fibril (i.e., the cylinder surrounding the fibril

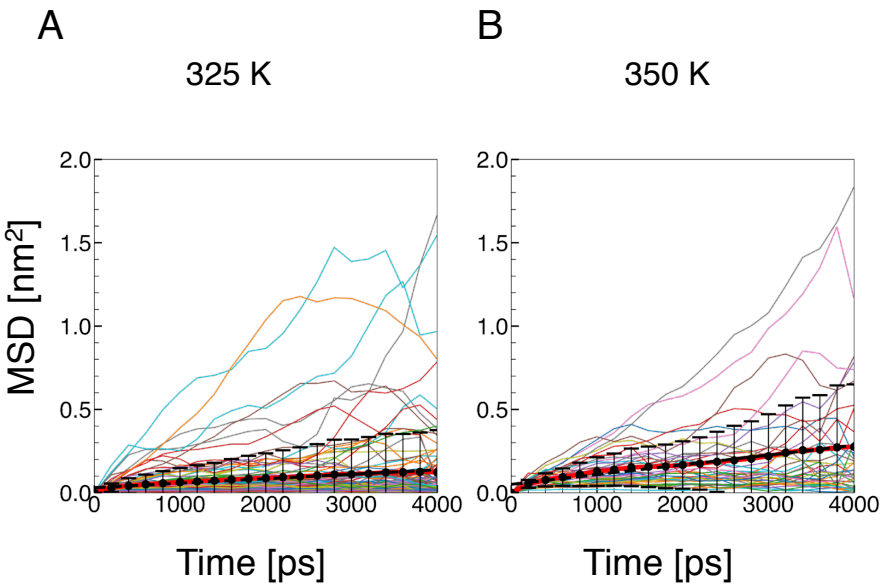

Figure 3.16 Mean square displacement of the COM of the peptide on the fibril surface for long fibril at A) 325 K, and B) 350 K. The mean MSD is shown in red and the error bars denote the standard deviation. The linear fit of the average MSD is represents using black dashed lines.

in Figure 3.17B),$A_{surface}$ is the area of the fibril edge (i.e., $2\times 2l_{\mathrm{b}} \times t$), and C is the peptide concentration, i.e., $\left(\frac{1}{V_{cylinder}-V_{fibril}}\right) nm^{-3}$. Estimates of k_{b} computed from our trajectories at 298 K, 325 K, and 350 K are provided in Figure 3.10.

Estimation of residence time The average time between consecutive binding and unbinding events to the fibril surface accounts for τ_{off}, i.e., the residence time. The average value of τ_{off} over all trajectories is shown in Figure 3.10A.

3.2.2 Comparison with Molecular Dynamics simulations

To further bridge the understanding between the continuum and atomic models, the relevant physical quantities used in the continuum model are estimated from MD trajectories to identify the growth mechanism. Simulations for peptide-fibril interactions are performed for pre-formed fibrils with three aspect ratios, namely $\epsilon = 1.79$, 3.86 and 5.29. We also study how the change in temperature affects the growth of fibrils by collecting data at 289, 325 and 350 K, respectively. The

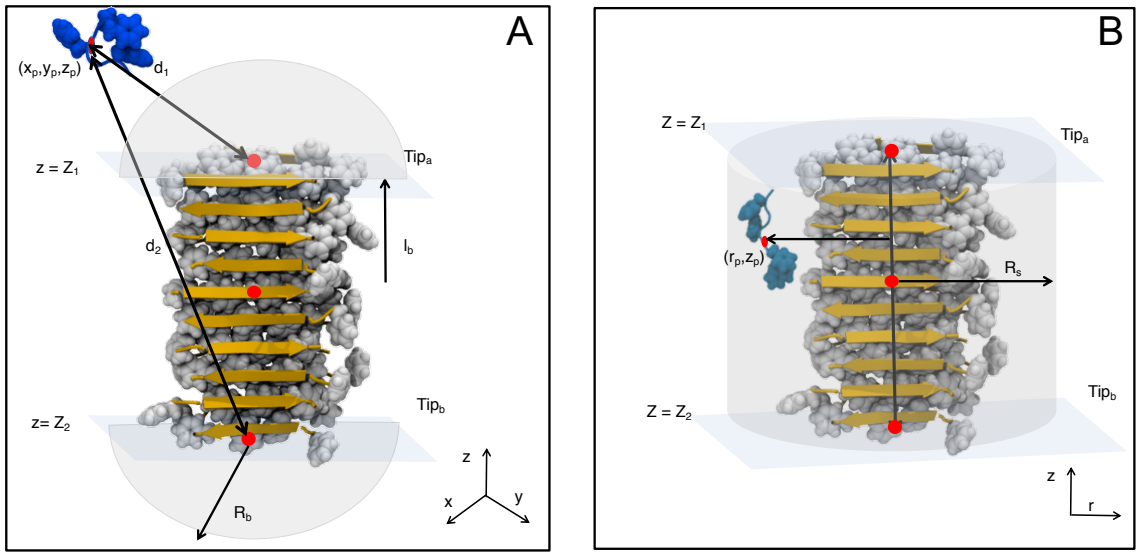

Figure 3.17 A) Schematic representation of the fibril, the peptide, and the relevant bulk volume (radius of R_b=2) encompassing both tips. B) Schematic representation of a fibril, peptide, and a cylindrical contour around the surface from fibril axis.

results for $\epsilon = 3.86$ are summarized in Figure 3.10A. We observe that D_{b}, D_{s}, k_{b}, k^{b}_{on}, and k^{s}_{on} increase with increasing temperature whereas τ_{off} is lower at higher temperature. These expected dependencies on temperature are, however, does not lead to a monotonically increasing or decreasing behaviors of Δ, ζ_b or ζ_s at higher temperatures.

More insights into this dependence can be inferred from an analysis of the state of the peptide in MD simulations. In particular, the percentage of trajectories in which the peptide ends up locked onto the fibril tip decreases from 100% at 350 K to 60% at 325 K. This trend is observed for fibrils of all lengths at 298 K, wherein only one out of the five trajectories (i.e., 20%) shows fibril growth. In the other trajectories, the peptide is found on the fibril surface suggesting that, not only the tip, but also the fibril surface can behave as a reservoir, adsorbing peptides as temperature decreases. This result is consistent with experimental data on the temperature dependence of secondary nucleation [148]. The latter phenomenon is found more frequently at lower temperatures, suggesting that the fibril surface enhances the attraction of peptides at lower temperature. One may, therefore, speculate that Δ increases with decreasing

temperature to account for a higher concentration of peptides at the fibril surface, which would enable enhanced secondary nucleation rates.

The interplay between attachment kinetics and diffusive transport is reflected in the estimated values of ζ_b and ζ_s. At 325 K, the estimated values shows $\zeta_s \sim O(1)$ and $\zeta_b \gg 1$, suggesting the fibril growth from the bulk peptides is attachment rate-limited, whereas the surface-mediated growth is neither attachment rate-limited nor diffusion-limited. They hereby focus on the limits of $\zeta_b \to \infty$ and $\zeta_s = 5.96$, which corresponds to the the boundary conditions in the steady-state equations, i.e. $\partial\tilde{C}/\partial\tilde{z}\,|_{\tilde{r}<1,\tilde{z}=\pm\epsilon/2} = 0$ and $\tilde{n} = \mp 5.96\,\frac{\partial\tilde{n}}{\partial\tilde{z}}\big|_{\tilde{z}=\pm\frac{\epsilon}{2}}$. Using $\Delta = 0.46$, the contour plots of steady-state bulk density for fibrils with $\epsilon = 5$, 10 and 20 are shown in Figure 3.10B, reflecting how the bulk density changes during fibril growth for this particular molecular system. The variations in bulk density are smaller than that of diffusion-limited case due to the absence of sinks. This results in an higher average bulk density at the vicinity of the fibril. Similar boundary layer effects are observed, as the fibril elongates, the boundary layers at the tips start to decouple from one another, resembling the transition behavior in Figures 3.5 and 3.8. The elevated bulk density can also be confirmed by the steady-state surface density profiles (Figure 3.10C), as $\tilde{n}_{ss}$ gradually converges to 1 away from the tips when ϵ increases from 2 to 50.

When plotting the dimensional bulk and surface flow rates, $J_b = k_{\text{on}}^b C_0 R^2 \tilde{J}_b$ and $J_s = R D_b C_0 \tilde{J}_s$ in Figure 3.10D, they observe that J_b is always two times greater than J_s for each fibril length. This suggests that the bulk peptides contribute more to the fibril growth than surface peptides in this particular system with the specific set of physical parameters. Moreover, both flow rates increase at low fibril lengths, and become constant for $L \gtrsim 15$ nm. They note that due to the limited number of elongation events observed in MD simulations, the estimated values of k_{on}^b and k_{on}^s for this system are subject to significant errors. Running repeated simulations under

the same settings will produce more accurate estimations of the physical parameters used in the continuum model.

3.3 Discussion

Amyloid fibrils, the insoluble and mechanically stable β-sheet structures in human cells, are found to be associated with the pathology of many fatal diseases. Despite the progress made in determining the molecular structures of the fibrils, the biophysics of nucleation, growth, and proliferation remains insufficiently characterized. To address this gap in knowledge, we and our collaborators combine all-atom molecular dynamics simulations with theory to study the growth kinetics of a single amyloid fibril in bulk solution. We identify that besides the classical dock-and-lock mechanism, peptides frequently interact with the fibril surface and bind to the tips via surface diffusion, revealing an important role of the surface in the overall growth kinetics. A continuum model that incorporates various phenomena observed in MD simulations is constructed to facilitate the analysis of this multi-scale problem. The physical parameters that affect the fibril growth are summarized using four dimensionless parameters, ϵ, Δ, ζ_b and ζ_s, which collectively capture the state-state behavior of a growing fibril.

Our collaborators note that more accurate geometrical approximations of a single proto-fibril can be deployed rather than a cylinder in the current continuum model, which has an overestimated surface area for binding. For example, the tips may be approximated by rectangles/ellipses, and the corresponding binding surfaces by rectangles/segments of a curved cylindrical surface, such that the overall geometry can be viewed as a cuboid or an elliptic cylinder with reduced amenable surface area for peptide binding. This will lead to a quantitative change in the results, as the total surface binding area may get five times smaller than an entire curved cylindrical surface. However, they do not expect the qualitative results to differ from the current

analysis. The cylindrical approximation, in fact, displays an advantage over other methods when one considers the probable formation of higher-order structures, i.e. fibril bundles of two or more proto-fibrils with helical structure [149, 150]. Due to the more circular geometry and uniformly distributed surface binding sites, this continuum model will be more accurate in interpreting the growth kinetics of fibril bundles.

Since there is no firm understanding on whether the growth of amyloid fibrils is attachment rate-limited or diffusion-limited at physiological concentrations in the existing literature [151, 152, 153], their continuum model incorporates both effects. During diffusion-limited growth ($\zeta_b \to 0$ and $\zeta_s \to 0$), the elongation at the fibril tips is supplied by the flux of peptides from the bulk and the surface. The continuum model predicts that for any finite Δ, there exists a boundary layer width around which surface density changes from 0 to 1. This leads to a critical fibril length above which it takes infinite amount of time to transport surface peptides to the tips via diffusion, thus the growth of fibrils exceeding this length will be bulk diffusion-dominated, and thus elongating with constant velocity. The generalized formulation also enables us to explore the reaction-limited growth or any regime in between the two limits. For instance, they also discuss the case where growth by bulk peptides is attachment rate-limited ($\zeta_b \to \infty$) while growth by surface peptides is diffusion-limited ($\zeta_s \to 0$), which means the conformational changes of free peptides at tips before permanently binding are much slower than rate of diffusive transport in the bulk but much faster than diffusion on the surface. Moreover, it is also possible that both pathways are attachment rate-limited ($\zeta_b \to \infty$ and $\zeta_s \to \infty$), which a system will develop uniform bulk density over the surface at steady state. The total flow rate to the tips is then $J_{\text{total}} = k_{\text{eff}} C_0$, where $k_{\text{eff}} = 2\pi R^2 k_{\text{on}}^b + 2k_{\text{on}}^s/\mu$. This expression implies that there will be no length dependence of the fibril growth rate, which has been assumed in the existing kinetic models.

Our contribution results also indicate that, as temperature increases, the peptide diffuses faster both on fibril surface and in the bulk to reach the tips. As temperature decreases, the peptide spends more time on the fibril surface with a lower diffusion rate. To the best of our knowledge, the results for the temperature dependency of the role of the surface and elongation pathway at atomic level with unbiased simulations were revealed for the first time. We and our collaborators observe that the binding rate from bulk to surface, k_b, is approximately proportional to the bulk diffusion coefficient D_b during the mass transport process under different temperatures, which can be replaced by a constant in calculating Δ, thus the product of $D_s(T)$ and $\tau_{\text{off}}(T)$ in the denominator causes the weak temperature dependence in this particular system. τ_{off} is proportional to the Arrhenius factor of the binding free energy E_1 of the peptides, i.e. $\tau_{\text{off}} = A_1 \exp(\frac{E_1}{k_{\text{B}}T})$, where A_1 is a prefactor and $k_{\text{B}}T$ denotes the thermal energy at temperature T [154]. Similarly, the surface diffusion coefficient can be expressed as $D_s = A_2 \exp(-\frac{E_2}{k_{\text{B}}T})$, where A_2 is another prefactor and E_2 is the activation energy for a peptide to undergo surface diffusion. Therefore, $\Delta = A_3 \exp(\frac{-E_1+E_2}{k_{\text{B}}T})$, where A_3 is a constant. This expression suggests that, for $|-E_1 + E_2| \ll k_{\text{B}}T$, the system will show weak temperature dependence of Δ.

This provides insights into a better understanding of the temperature dependency of secondary nucleation. Our MD results are consistent with the previous experimental studies showing that fibril elongation increases at higher temperatures, whereas secondary nucleation decreases at higher temperatures [123, 155]. Experimental studies also have shown that perturbing the binding of the peptide to the fibril surface can be a pathway to inhibit secondary nucleation [156, 123]. Our collaborators then speculate from the continuum model that both higher binding free energy (E_1) and lower temperatures can increase the residence time of peptides on fibril surface once they bind. At the same time, large E_2 and lower temperature can hinder peptides from diffusing to the fibril ends for

elongation. By assuming that the rate of secondary nucleation is proportional to the probability of two surface peptides to interact, i.e. $\propto n^2(z,t)$, the continuum model suggests that longer fibril lengths and higher Δ values in general lead to higher surface peptide density, which could potentially create sufficient conditions for secondary nucleation to occur.

Overall, this chapter introduces a framework for interpreting the growth of amyloid-like fibrils using atomistic and continuum models at the same time. Methodologically, the MD simulations provides valuable insights of molecular interactions at atomic resolution while being limited by the computational costs in simulating large and complex systems that also require much statistical significance. The mesoscale continuum model, on the other hand, elevates the length and time scale of the problem at a lower computational cost. More importantly, it benefits from the physically significant inputs from MD simulations for a specific system. They have shown that the interplay among various physical parameters defined by a specific molecular system determines the underlying mechanism of fibril elongation. Both bulk and surface diffusion, and attachment kinetics can be key factors in the process. By formulating essential microscopic physical quantities involved in fibril growth into a continuum model, it may help us find optimized routes between bulk and surface pathways based on the goal of either increasing/decreasing fibril growth rate or inhibiting secondary nucleation in various systems.

3.4 Methodology

3.4.1 System design and MD simulations

All-atom molecular dynamics simulations in explicit solvent are performed in $10.1 \times 10.1 \times 10.1$ nm^3 cubic boxes containing a pre-formed fibril and a peptide. The box was then solvated with TIP3P water molecules, and the energy of the system was minimized followed by a 4 ns equilibration in the NVT ensemble. MD simulations were

performed with the Amber99sb-ILDN force field [61] in the isothermal-isobaric (NPT) ensemble. The leapfrog algorithm was used to integrate the equations of motion with a 2 fs time-step [55]. To maintain the pressure at 1 bar, the Parrinello-Rahman barostat ($\tau_p = 2.0$ ps) was employed [80]. Temperature was controlled by coupling protein and solvent separately to the velocity-rescale thermostat ($\tau_t = 0.1$ ps). The cut-off for short range van der Waals and electrostatic interactions was 1.0 nm. The smooth Particle Mesh Ewald algorithm was used to compute long range electrostatic interactions [81]. For all systems, the production run started with a 100 ns simulation in the NPT ensemble using GROMACS [82].

3.4.2 Numerical methods for solving steady-state equations

The non-dimensionalized equations (Equations (3.7) and (3.8) were solved using the Forward Time Centered Space (FTCS) method on a 2D uniform grid with spacing $d\tilde{r} = d\tilde{z} = 0.01$. $\tilde{C}(\tilde{r}, \tilde{z}, \tau)$ was solved for $\tilde{z} > \epsilon/2$ and $\tilde{r} > 1$; $\tilde{n}(\tilde{z}, \tau)$ was solved for $\tilde{r} = 1$ and $0 < \tilde{z} < \epsilon/2$. The full peptide bulk density profiles were obtained by mirroring with respect to both $\tilde{r} = 0$ and $\tilde{z} = 0$. The first and second derivatives are both evaluated to second order accuracy to minimize error long the fibril surface. Our collaborators also note that due to the limit of numerical grid size, extreme values such as $\Delta > 1000$ and $\Delta < 0.001$ might not retain the same accuracy as the tested cases. To reduce the boundary effects for different aspect ratios of the fibril, the grid size adapts with different aspect ratios: 1000×1000 for $\epsilon = 5$, and 1000×10000 for $\epsilon = 100$. A small time step $dt = 2 \times 10^{-5}$ is chosen to ensure numerical stability. The steady-state solutions in the parametric study with $\epsilon < 200$ were obtained in less than 5×10^7 time steps, while the case with $\epsilon = 200$ reaches steady state in 2×10^8 time steps.

CHAPTER 4

NUCLEATION AND GROWTH OF AMYLOID FIBRILS

Jalali, S., Zhang, R., Hattaja M. P., Dias, C. L., *Nucleation and growth of amyloid fibrils*, ready for submission.

The formation of amyloid fibrils is a complex phenomenon that remains poorly understood at the atomic scale. In Chapter 3 of this dissertation, we discussed the fibril growth kinetics and pathways involved in fibril elongation. In this chapter, we focus on nucleation via primary and secondary mechanisms and provide additional insights into the fibril growth that was studied in Chapter 3.

We find that primary nucleation takes place via the formation of an intermediate state made of two laminated β-sheets oriented perpendicularly to each other. The amyloid fibril spine emerges from the rotation of these β-sheets to account for β-strands that are parallel to each other and perpendicular to the fibril axis. Growth of this spine takes place via a dock-and-lock mechanism. Consistent with simulations performed in Chapter 3, we show that peptides dock onto the fibril tip either from bulk solution or after diffusing on the fibril surface. The latter docking pathway contributes significantly to populate the fibril tip with peptides.

Moreover, we show that side chain interactions drive the motion of peptides in the lock-phase during growth, enabling them to adopt the structure dictated by the fibril tip with atomic fidelity. Conversely, docked peptide gets trapped in a local minimum when docked-conformations are sampled randomly. Our simulations also highlight the role played by non-polar patches on the fibril surface in catalyzing and orienting the formation of small cross-β structures. Thus, our simulations are providing critical new insights into the pathways and interactions accounting for primary and secondary nucleation as well as fibril growth.

4.1 Introduction

The molecular mechanisms accounting for the aggregation of amyloid peptides into oligomers and fibrils is a topic of intensive research interest [121, 113, 114, 120, 157]. This is motivated by the importance of these aggregates in diseases such as Alzheimer's and Parkinson's as well as by the use of fibrils in various biomedical applications [40, 41, 42, 43, 35, 44, 45, 46]. Three processes have been shown to be critical for the formation of amyloid aggregates, which are the nucleation of fibril seeds via primary and secondary mechanisms, and the growth of these seeds into micrometer-long fibrils [123, 118]. Targeting these processes independently of each other may be required to treat diseases wherein toxic amyloid nuclei need to be inhibited without dissolving fibrils/plaques [158, 159]. This level of control requires an atomic understanding of the interactions, pathways, and intermediate structures involved in seed formation and growth, which remains mostly unknown.

The experimental characterization of fibril formation at the molecular level is challenging due to the dynamic nature and short timescales involved in seed formation and growth [114, 160]. Similarly, the large number of atoms that needs to be tracked for a considerable number of time-steps has made aggregation a difficult phenomena to simulate computationally [161, 162, 163, 164]. Many of the theoretical insights into fibril formation have, therefore, been obtained using coarse grained models [165, 166, 167, 168, 169, 170, 171] or enhanced sampling simulations [172, 173, 174, 128, 175, 176, 177]. These studies are providing insights into the structure of the nucleus, which for Aβ can be made of four or twelve peptides [178, 179]. Insights into the pathways accounting for primary nucleation have also been obtained for short peptides. For example, the aggregation of the Aβ_{16-21} peptide was shown to emerged in two steps where a disordered nucleus is formed first followed by its structural rearrangement into a cross-β structure [177]. Most of the fibril nuclei emerging in experiments were shown to be catalyzed at the fibril surface (i.e., via *secondary nucleation*) [117, 180]

with a possible exception reported for the Aβ_{16-22} peptide [181]. This catalytic effect of the fibril surface may be related to an increased concentration of peptides in its vicinity and/or to the ability of the surface to align peptides in a 2D plane. In umbrella sampling simulations, the association of Aβ_{9-40} peptides with the fibril surface was shown to be driven by the release of a large number of hydration water molecules and the formation of contacts between peptides and the fibril surface [175].

The *growth/elongation* of a fibril proceeds via the incorporation of peptides to both of its ends one peptide at a time [119, 182, 183]. It is often described as a *dock-and-lock* mechanism in which peptides bind promptly to the fibril ends (i.e., dock phase) where they slowly sample different conformations (i.e., lock phase) [120, 128, 184, 185]. The latter sampling is arrested when the incoming peptide aligns itself with fibril-end peptides forming parallel or anti-parallel β-sheets. Since more than 2,000 peptides are incorporated in a micrometer-long fibril (each time reproducing the fibril-end structure with atomic fidelity), the molecular pathways accounting for the lock phase have to be highly robust. Two such pathways have been proposed wherein conformational changes take place either randomly, subjected only by steric constraints (i.e., *steric templating* pathway), or driven by side chain interactions between incoming peptides and fibril-end peptides (i.e., *direct templating* pathway) [186, 187]. In addition to the dock-and-lock mechanism, fibril growth can also emerge via a fast-deposition mechanism where peptides adhere to fibril-ends in an activated state that enables them to promptly adopt the structure of the fibril without the slow locking phase [188, 189]. In all these studies, peptides are assumed to dock directly onto the fibril ends from bulk. However, peptides deposited on the fibril surface are also able to promptly diffuse to the fibril tip where they can contribute to growth [190].

Here, we use unbiased all-atom simulations in explicit solvent to provide a more complete and accurate picture of the aggregation process. We show that fibril

seeds from amphipathic Ac-$(FKFE)_2$-NH_2 peptides emerge spontaneously via primary nucleation, forming a cross-β pattern where the constituent β-sheets are initially oriented perpendicular to each other. This enables the efficient burial of non-polar residues away from the solvent. However, the growth of these seeds requires β-sheets to rotate and become aligned with each other, accounting for the amyloid fibril spine. The growth of an existing fibril in our simulations emerged spontaneously through a dock-and-lock mechanism where peptides landed (or docked) onto the fibril tip from bulk solution or after binding and diffusion on the fibril surface. At 325 K, electrostatic interactions between charged side chains of docked peptide and fibril drive the locking process in our simulations wherein the structure established by the fibril tip is reproduced with atomic fidelity. At 350 K, docked peptides get trapped in local energy minima while sampling their conformation randomly without ever adopting the structure of the fibril tip. Secondary nucleation is also simulated by adding peptides consecutively to a large simulation box containing a pre-formed fibril. The role of non-polar patches on the fibril surface in catalyzing small aggregates into cross-β structures is highlighted in these simulations.

4.2 Results and Discussion

4.2.1 Primary nucleation

Simulation Setup. To provide insights into the formation of a fibril nucleus in bulk solution, 1.5-μs long simulations were performed with 8, 10, 15, and 20 peptides embedded randomly in large solvated boxes of dimension 13 $\times$ 13 $\times$ 13 nm^3. This accounts for 6.0, 7.5, 11.3, and 15.1 mM peptide concentrations. Except at the lowest concentration, a stable cluster containing most of the peptides is formed before the end of the simulation. These clusters exhibit the cross-β pattern that is characteristic of amyloid fibrils wherein non-polar residues of two β-sheets are buried against each other. In simulations performed at the highest concentrations (i.e., 11.3 mM and

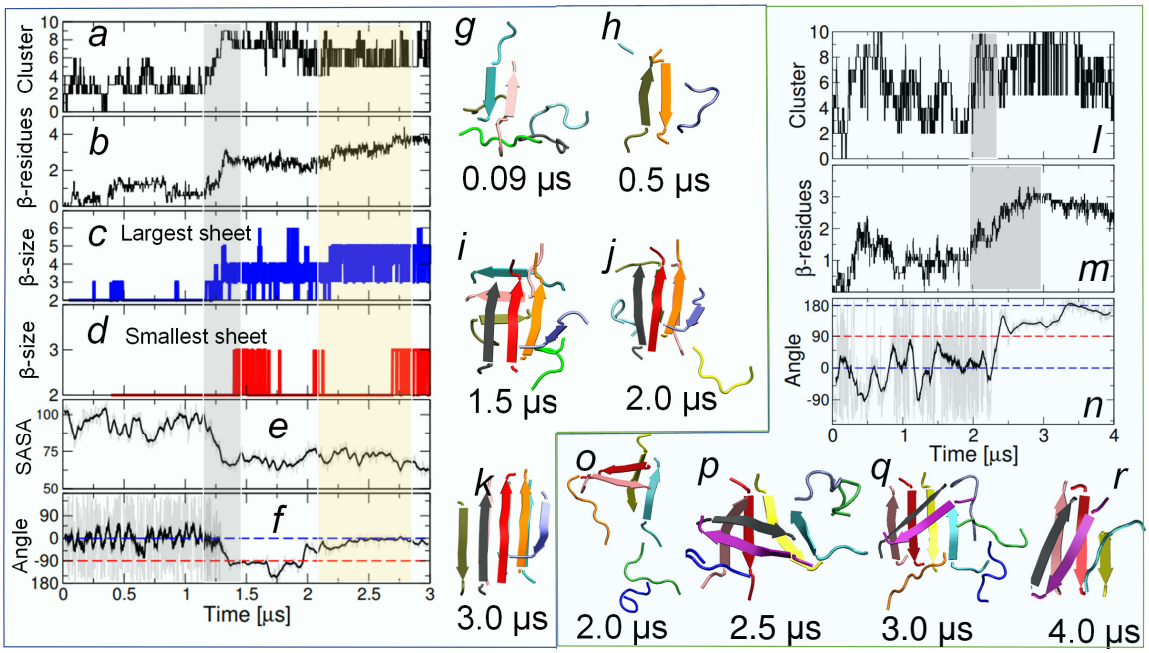

Figure 4.1 Primary nucleation of two independent trajectories. The time dependence of different quantities are computed to characterize the spontaneous formation of cross-β structures. These quantities are (a and l) the largest cluster size in the simulation box, (b and m) the number of residues per peptide in a β-structure, the number of peptides comprising (c) largest and (d) second largest β-sheet in the simulation box, (e) solvent accessible surface area (SASA) of non-polar residues, and (f and n) dihedral angle between peptides of largest and second largest β-sheets. The formation of a stable oligomer and its structural rearrangement are highlighted by gray and orange rectangles in panels a-f and l-n. Conformations of the largest cluster at different instances of time are shown in panels g-k, and o-r for the two independent trajectories. A different color is used for each peptide.

15.1 mM), these clusters emerged promptly within 0.25–0.5 μs making it difficult to identify the sequence of events leading to their formation–see Figures [?, ?]. Therefore, we focused on two simulations performed at 7.5 mM, which were extended beyond 1.5 μs.

Nucleus Formation. Figures 4.1*a*-*b* and 4.1*l*-*m* depict the size of the largest cluster and the number of residues making up β-sheet structures in two independent simulations performed at 7.5 mM. Clusters form and dissociate within the first 1 μs and 2 μs of the first and second trajectories. These intermittent clusters are mostly

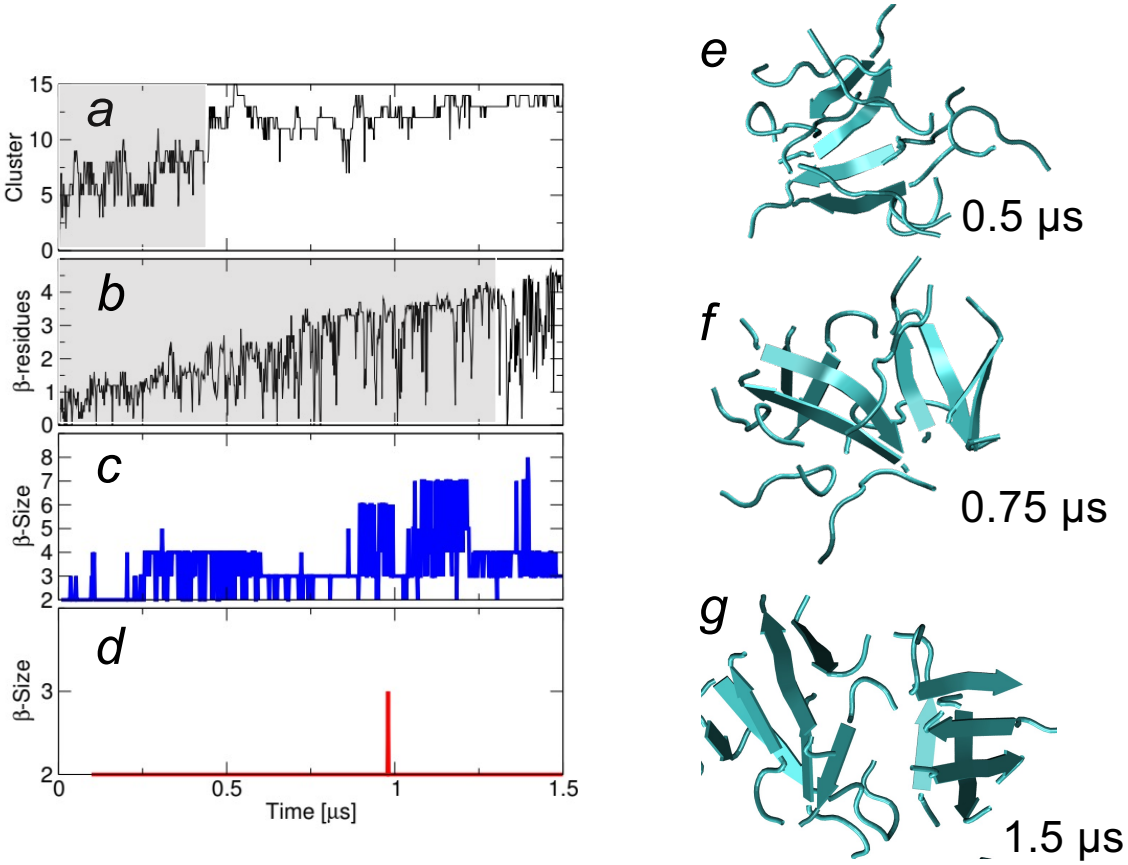

Figure 4.2 Primary nucleation of trajectory with 15 peptides. The time dependence of different quantities are computed to characterize the spontaneous formation of cross-β structures. These quantities are (a) the largest cluster size in the simulation box, (b) the number of residues per peptide in a β-structure, and the number of peptides comprising (c) the largest and (d) the second largest β-sheet in the simulation box. Visual representation of the largest aggregate at different instants of time is shown in panels e-g.

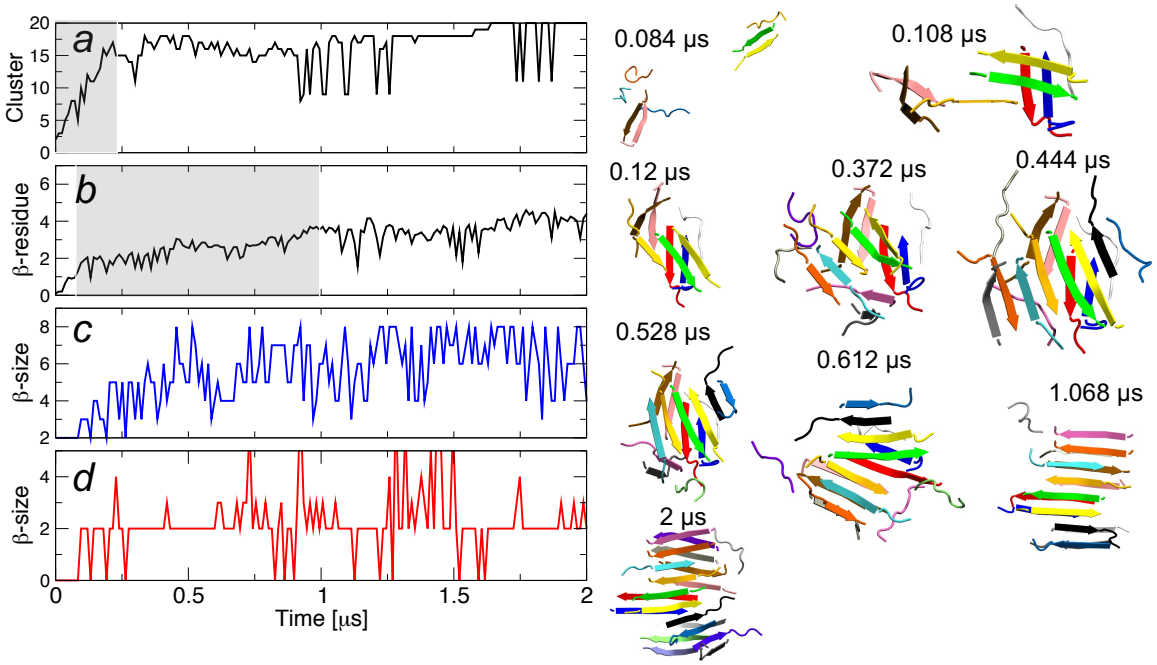

Figure 4.3 Primary nucleation of trajectory with 20 peptides. The time dependence of different quantities are computed to characterize the spontaneous formation of cross-β structures. These quantities are (a) the largest cluster size in the simulation box, (b) the number of residues per peptide in a β-structure, and the number of peptides comprising (c) the largest and (d) the second largest β-sheet in the simulation box. Visual representation of the largest aggregate at different instants of time is shown on the right-hand side. A different color is used for each peptide.

dimers and trimers in the first trajectory (see panels g and h) but also heptamers and tetramers in the second trajectory.

In the first simulation, a stable nucleus comprising 6-8 peptides emerges abruptly at 1.25 μs when the cluster size (panel a) and the number of β-residues (panel b) increase simultaneously–see the gray shade. This characterizes a one-step nucleation process in which the nucleus is formed in an orderly manner [191]. In the second simulation, a stable nucleus comprising 6-8 peptides forms after 2.0 μs. In the latter process, the cluster size increases within a short time-window of 0.2 μs (see panel l) while the number of β-residues (see panel m) increases slowly over $\sim$1 μs–see gray shades. This characterizes a two-step nucleation process wherein aggregation takes place with a significant amount of disorder requiring subsequent conformational changes. The existence of different timescales for aggregation and conformational ordering of peptides is also observed in our high-concentration simulations (i.e., 11.3 nm and 15.1 mM). In the latter, the number of β-residues increases long after the cluster size has saturated. These results are consistent with a recent study showing that the Aβ_{16-21} peptide undergoes a one-step nucleation process at low concentration and a two-step process at high concentration [177].

Perpendicular and Parallel Cross-β Structures. To characterize the structure of the nucleus, panels c and d depict the size of the two largest β-sheets in the system in the one-step nucleation process. Also, panel e depicts the solvent accessible surface area of non-polar residues, i.e., $\mathrm{SASA_{NP}}$. These panels show that the two β-sheets increase in size during/after the formation of a nucleus (i.e., the gray shaded area), and this coincides with an abrupt decrease in SASA as non-polar residues of the two β-sheets become buried away from the solvent. This characterizes the cross-β pattern of amyloid fibrils for which a representative structure is depicted in panel i. In the two-step nucleation process, the early aggregate, which formed at $\sim$ 2 μs, also exhibits two β-sheets with non-polar residues buried against each other

and with disordered peptides around them–see panel o. These disordered peptides become incorporated into the two β-sheets within time 2 μs and 3 μs–see panels p-q.

Clusters formed via one-step (panel i) and two-step (panel o-q) processes exhibit two β-sheets that are initially oriented perpendicularly to each other. They remain in that configuration for more than 0.5 μs before reorienting themselves to become aligned with each other—see panels j,k, and r. This process is quantified in panels f and n, which show the time dependence of the dihedral angle between peptides on opposing β-sheets. Initially, in the trajectory, the dihedral angle can take any value from -180^{o} to 180^{o} as peptides move freely in the simulation box-see light gray line. As the early nucleus is formed, the dihedral angle adopts values close to -90^{o} or 90^{o}, which is indicative of perpendicular cross-β structures. Panel f takes place between 1.25-2 μs. Subsequently, the dihedral angle changes to $\sim 0^{o}$ as β-sheets become parallel to each other. Similarly, for panel n, the dihedral angle adopts values close to 90^{o} between time 2.5-3.25 μs. This is followed by an increase in the dihedral to 180^{o} characterizing parallel β-sheets–see panel r.

Note that average SASA (panel f) of perpendicular and parallel nuclei are very similar in magnitude despite β-sheets being made of more peptides in the latter. This suggests that non-polar residues can bury themselves more efficiently in perpendicular cross-β structures, which could be the force driving the formation of these structures. However, perpendicular cross-β structures need to rotate for the early nucleus to grow as peptides cannot be incorporated indefinitely into β-sheets that are perpendicular to each other while shielding their non-polar residues from water.

4.2.2 Fibril growth

Simulation Setup. To investigate the mechanisms accounting for fibril growth, all-atom simulations were performed in a solvated box of size 10.1 $\times$ 10.1 $\times$ 10.1 nm^3 containing a pre-formed fibril and a peptide. The fibril is constructed by packing

non-polar faces of two antiparallel β-sheets made from ten Ac-$(FKFE)_2$-NH_2 peptides against each other–see Figure 4.12. This corresponds to class 5 of the amyloid spines classification scheme by Eisenberg and Sawaya [69]. The solvated peptide is initially deposited randomly at a distance larger than 2 nm from the pre-formed fibril, and simulations are performed at 298 K, 325 K, and 350 K.

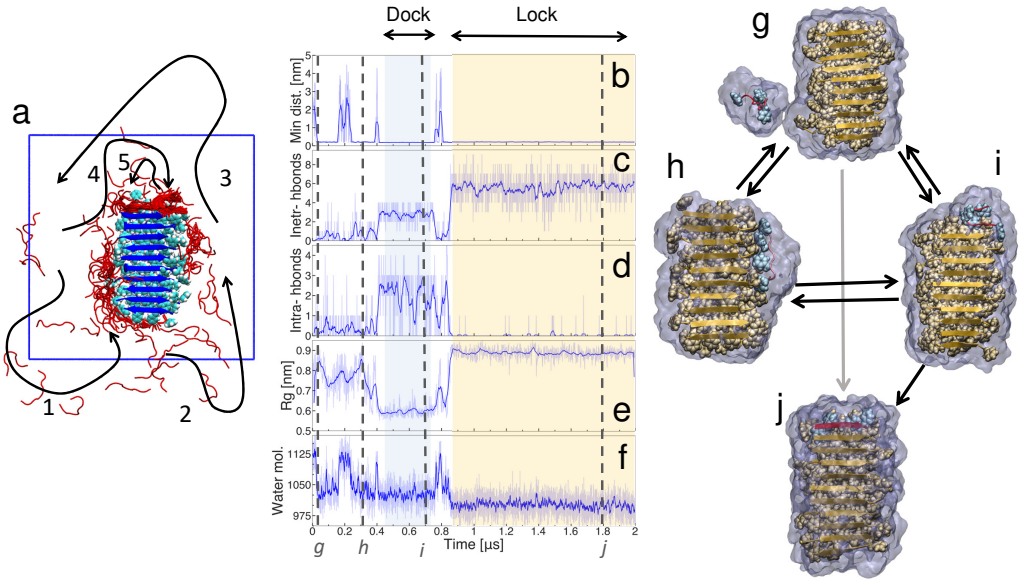

Figure 4.4 Unbiased pathway accounting for fibril elongation. (a) The trajectory of the peptide as it interacts with the fibril before docking to its tip is shown. The conformations of the peptide (in red) is depicted at every 20 ns. Numbered arrows show the progression of the peptide in the simulation. The fibril is depicted using a cartoon representation in blue and a van der Waals representation for phenylalanine side chains in cyan. The time dependence of five quantities are computed to characterize the peptide-fibril complex: (b) minimum distance between atoms of the fibril and the peptide, (c) inter- and (d) intra-backbone hydrogen bonds, (e) radius of gyration of the peptide, and (f) number of water molecules around peptide and fibril. Sample configurations of the peptide-fibril complex when the peptide is (g) fully solvated, (h) bound to the fibril surface, (i) docked and (j) locked onto the fibril tip. Arrows highlight possible transitions between these different states.

Addition of Peptides to Fibrils. Figure 4.4a depicts the trajectory of the free-peptide as it binds to and unbinds from the pre-formed fibril in one of our 350 K simulations. Backbone conformations of the free-peptide (in red) are shown at every 20 ns and numbered arrows depict the sequence of events in the simulation. The peptide explores several of the non-polar binding sites at edges and tips of the

fibril but it rarely binds to the charged faces of the fibril. To quantify these binding and unbinding events, panel b shows the time dependence of the minimum distance ξ between atoms of the peptide and the fibril. The peptide, which is initially in the solution (i.e., $\xi > 2$ nm), is attracted to the fibril in less than 0.025 μs where it binds ($\xi \leq 0.2$ nm) and remains bound for approximately 0.125 μs. The peptide then detaches itself to become fully solvated. It undergoes three other of these binding-unbinding events until time ~ 0.8 μs when it locks onto the fibril tip. It remains locked until the end of the simulations, i.e., for more than 1.2 μs.

To further characterize the state of the system, panels c-d depict numbers of inter- and intra-backbone hydrogen bonds of the peptide. When it is solvated (i.e., ξ is large than 0.2 nm) or bonded to sides/edges of the fibril, the number of inter-peptide hydrogen bonds is mostly negligible. This quantity is non-negligible only when the peptide binds to the fibril tip as highlighted by blue and yellow shades. The number of intra-peptide hydrogen bonds is non-negligible only when the peptide adopts a folded conformation. In the blue shaded are in Figure 4.4, the peptide adopts a "hairpin"-like conformation while docked onto the fibril tip. This binding event lasts for approximately 0.3 μs after which the peptide detaches itself from the fibril tip while retaining its hairpin-like conformation. The radius of gyration, which quantifies the compactness of the peptide, is shown in panel e. This quantity is maximum when the peptide is locked into the fibril tip (see yellow shade) and it is minimum when the peptide is folded into a hairpin-like conformation–see blue shade. While fully solvated or on the fibril surface the radius of gyration adopts intermediate values.

Panel f shows the number N_{shell} of water molecules within a distance of 0.4 nm from either the peptide or the fibril. The number of shell-water is a maximum when the free-peptide is fully solvated. As it interacts with the fibril, desolvation takes place as some shell-water molecules are released into the bulk, accounting for a reduction in N_{shell}. The number of shell-water in panel f is minimal when the free-peptide locks

onto the fibril tip–see the yellow shade. Note that when the fibril grows by one layer, the structure of the fibril end is reproduced with atomic fidelity, and the number of shell water around the end does not change significantly. Thus, the reduction in N_{shell} when the peptide locks onto the fibril end must be due to shell-water molecules around the free-peptide released into the bulk. The release of shell-water into the bulk is a highly favorable entropic process around non-polar residues [192, 193, 194, 195, 196] contributing to the energetics of elongation [128, 174, 173, 172].

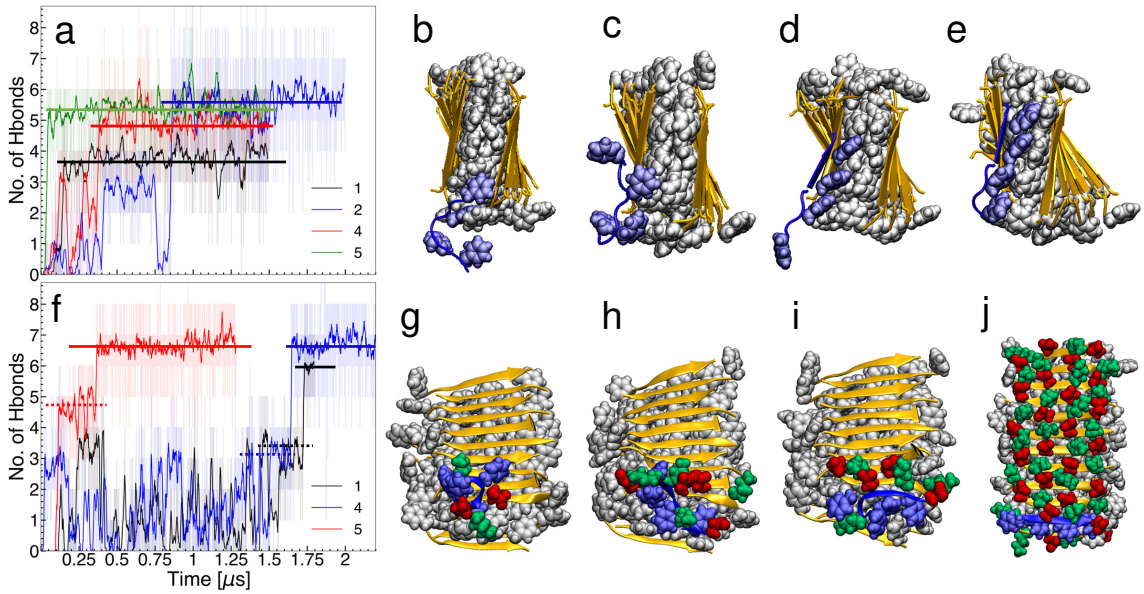

Figure 4.5 Locking of the peptide to the fibril tip. The time dependence of the number of inter-backbone hydrogen bonds between peptide and fibril at (a) 350 K and (f) 325 K. The structure of the peptide-fibril system in trajectory number 4 at 350 K is represented at time (b) 0.16 μs, (c) 0.37 μs, d) 0.57 μs, and (e) 0.90 μs. The structure of the peptide-fibril system of trajectory number 5 at 325 K is shown at time (g) 0.09 μs, (h) 0.11 μs, (i) 0.2 μs, and (j) 1.01 μs. A van der Waals representation is used for non-polar residues of the fibril (white) and peptide (blue). Negatively charged glutamic acid and positively charged lysine are represented in red and green, respectively.

Transitions between different peptide-fibril binding modes. The quantities depicted in Figure 4.4b-f highlight the different states of the peptide in which it can be fully solvated, bound to the fibril edge as well as docked and locked to the fibril tip–see panel g. Six additional simulations (i.e., seven in total) were

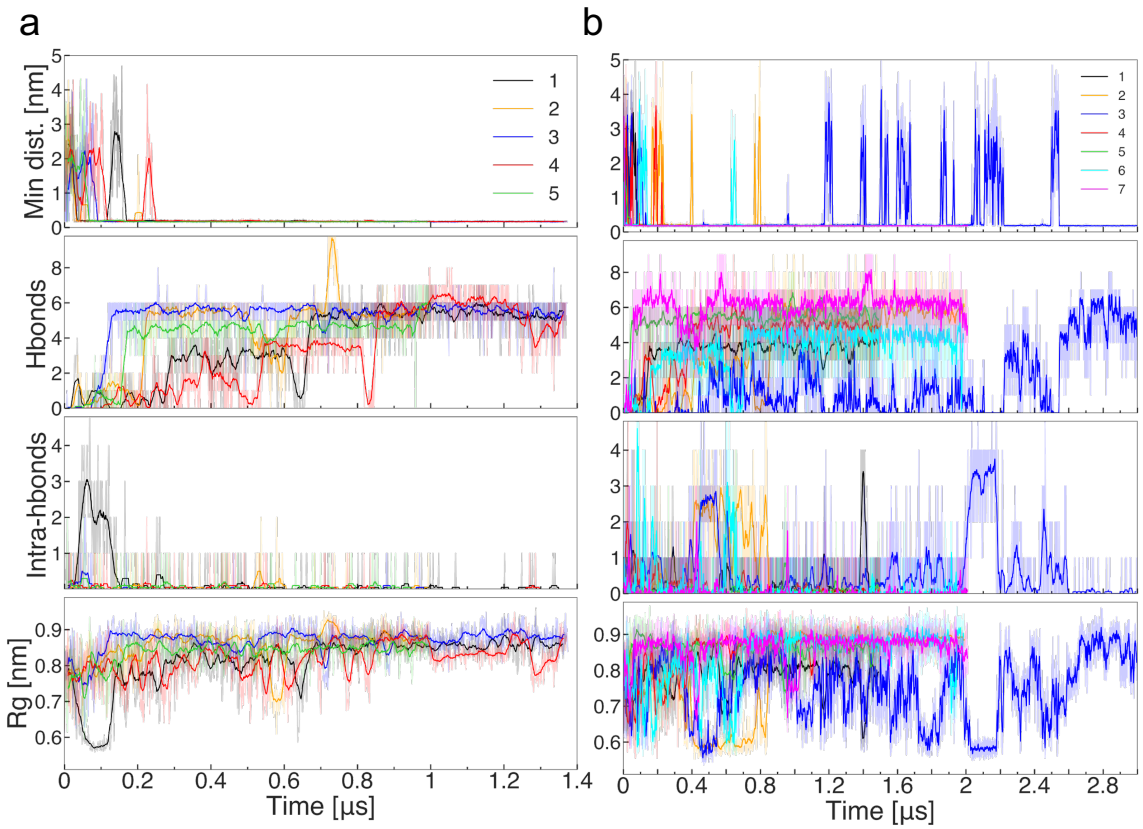

Figure 4.6 Schematic representation of the four quantities used to characterize binding of the peptide to the fibril in simulations performed using (a) CHARMM36m and (b) Amber99sb-ILDN force fields at 350 K. Fist row shows the minimal atomic distance between the fibril and the peptide. Second and third rows show inter- and intra-molecular hydrogen bonds. The last row shows the radius of gyration.

performed at 350 K to provide insights into the allowed transitions between these different states. In all simulations, the peptide end-up locked onto the fibril tip where it remained until the end of the simulation, i.e., for more than 0.5 μs. In two and five of these simulations, the peptide formed anti-parallel and parallel β-sheets with the fibril, respectively. Moreover, the quantities shown in Figure 4.4b-e were computed for all simulations and the state of the peptide was determined at any given time–see Figure 4.6b.

In three of the seven simulations, the peptide became incorporated onto the fibril tip in less than 0.15 μs. In these simulations, the peptide diffused in bulk solution before docking onto the tip. This was followed by the peptide promptly (in less than

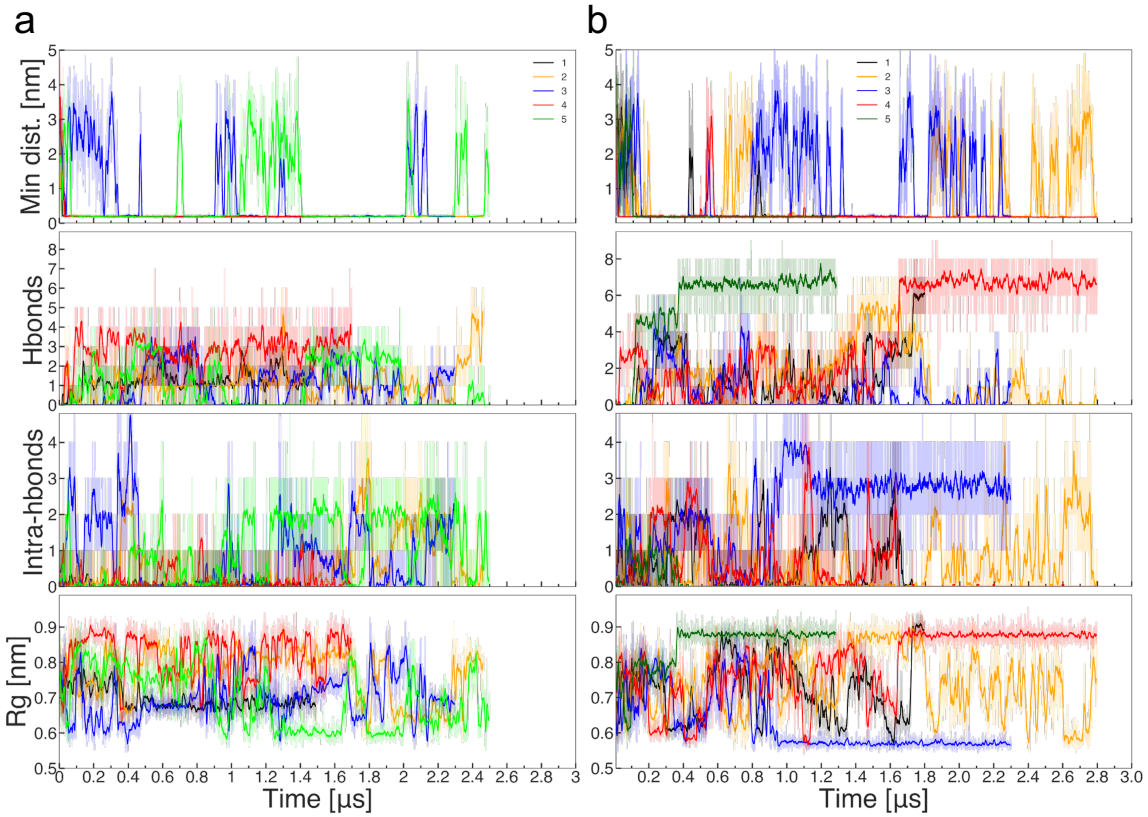

Figure 4.7 Schematic representation of the four quantities used to characterize binding of the peptide to the fibril in simulations performed using at (a) 298 K and (b) 325 K. Fist row shows the minimal atomic distance between the fibril and the peptide. Second and third rows show inter- and intra-molecular hydrogen bonds. The last row shows the radius of gyration.

0.01 μs) changing its conformation to lock into the fibril tip. This characterizes a "fast-deposition" process in which the peptide is deposited at the tip in an activated state that requires little conformational change to reproduce the template provided by fibril tip [189, 188]. This process is symbolized in Figure 4.4g by a gray arrow. In the other four simulations, the peptide is also found to lock itself onto the fibril tip within less than 2 μs. This took place after the peptide reached the tip either from the solution or after diffusing on the fibril surface. At the tip, the docked peptide can detach itself to become solvated, diffuse back to the fibril edge, or lock itself onto the fibril tip. These observed transitions in our simulations highlight the diversity of pathways by which a peptide can lock itself onto the fibril tip and they are shown by arrows in Figure 4.4g. An estimate of the transition rate between these states and how they can be used to build continuum models of fibril growth is provided in another publication.

Effects of Temperature. To provide insights into effects of temperature on the dock-and-lock mechanism, five simulations were also performed at both 298 K and 325 K–see Figure 4.7a, Figure 4.7b . In three of the five simulations at 325 K, the peptide ended up locked in an anti-parallel β-sheet conformation forming $\sim$7 inter-backbone hydrogen bonds with the tip.

At 298 K, some of the five simulations were extended up to 4 μs and in only one of them did the peptide lock onto the fibril tip. Thus, at lower temperature (both 325 K and 298 K), most of the simulation time is spent with the peptide on the fibril surface and much longer simulations are required to enable locking. This shows that the fibril surface plays an important role in the kinetics of growth by adsorbing peptides onto it.

Locking into the fibril tip. Figure 4.5 illustrates the process by which the peptide samples different structures before locking into the fibril tip at 350 K (i.e., upper panels) and at 325 K (lower panels). Panel a shows the number N_{HB} of hydrogen

bonds between peptide-fibril backbone atoms in four trajectories at 350 K. In most trajectories, N_{HB} increases abruptly after the peptide lands onto the fibril tip. In this process, at least one of its phenylalanine side chain remains in contact with the fibril tip at all time while the other non-polar side chains are free to move and probe different interaction sites at the tip–see panels b-e. These events are enabled by the high temperature of the simulations, which provides a more random component to the motion of the peptide. The latter is arrested when enough bonds are formed between the peptide and the fibril without necessarily accounting for the proper alignment. Accordingly, in two trajectories the peptide formed parallel (instead of an anti-parallel) β-sheets at the tip. Moreover, within the time-frame of the simulation (i.e., at least 1.5 μs), N_{HB} does not change significantly after 4-6 hydrogen bonds have formed (see panel a) whereas a perfect alignment of the peptide with the fibril requires the formation of at least 7 hydrogen bonds. Accordingly, the atomic structure of the tip is never reproduced by the peptide in any of the seven simulations performed at 350 K.

Panel *f* depicts N_{HB} for the three simulations in which the peptide locks onto the fibril tip at 325 K. At this temperature, the locking process takes place in two steps highlighted by dashed and full lines. An increase in N_{HB} from zero to 3-5 (dashed lines) accounts for the first step, which lasts for 0.1-0.3 μs. The second step emerges from another increase in N_{HB} to approximately 7 hydrogen bonds. The latter gives rise to configurations in which the peptide is aligned with the fibril forming anti-parallel β-sheets in all three simulations. To show how the peptide becomes aligned with the fibril, characteristic configurations during the lock phase is shown in panels g-j for trajectory number 5, i.e., red line in Figure 4.5f. Panel g shows that the peptide lands on the tip in a random conformation with some of its non-polar side chains buried away from the solvent. Conformations highlighting the first step of the lock-phase are depicted in panel *h-i*. They are characterized by the alignment of the

C-terminal of the peptide with the fibril wherein charged side chains of the peptide interact with oppositely charged side chains of the fibril. The peptide remains in this configuration for more than 0.2 μs until charged side chains at the N-terminal of the peptide become aligned with charged side chains of the fibril–see panel j. This type of step wise alignment of the peptide contrasts with the random sampling at high temperature.

Our simulations give rise to results that at first sight appear counter-intuitive: peptides docked onto the fibril tip are more likely to find the global minimum at low temperature than at high temperature where they get trapped in local minima. This emerges because electrostatic interactions between charged side chains are disrupted by thermal fluctuations at high temperature and cannot drive the alignment of the peptide. Thus, a random conformational search takes place until a significant number of peptide-fibril bonds are formed trapping the peptide at the tip without necessarily accounting for the proper alignment. At low temperature, the peptide becomes aligned with the fibril in a step wise manner wherein charged side chains at one extremity of the peptide are aligned first followed by the other extremity. The latter process enables the structure of the fibril to be reproduced with atomic fidelity.

4.2.3 Secondary nucleation

Simulation Setup. Secondary nucleation starts with the attraction of peptides to the fibril surface enabling the local peptide concentration to reach critical values required to form a stable nucleus. The adsorption of peptides onto the fibril edge in our simulations (see Figure 4.4) hints to the possibility of secondary nucleation being a mechanism of fibril formation for the Ac-$(FKFE)_2$-NH_2 peptide. However, the formation of a nucleus requires more than one peptide to be present in the simulation box. To investigate this mechanism, we have therefore performed six simulations with 6 peptides in $13 \times 13 \times 13$ nm^3 boxes containing one pre-formed fibril at 350 K.

These peptides are placed randomly in the simulation box at a distance larger than 2 nm from the pre-formed fibril.

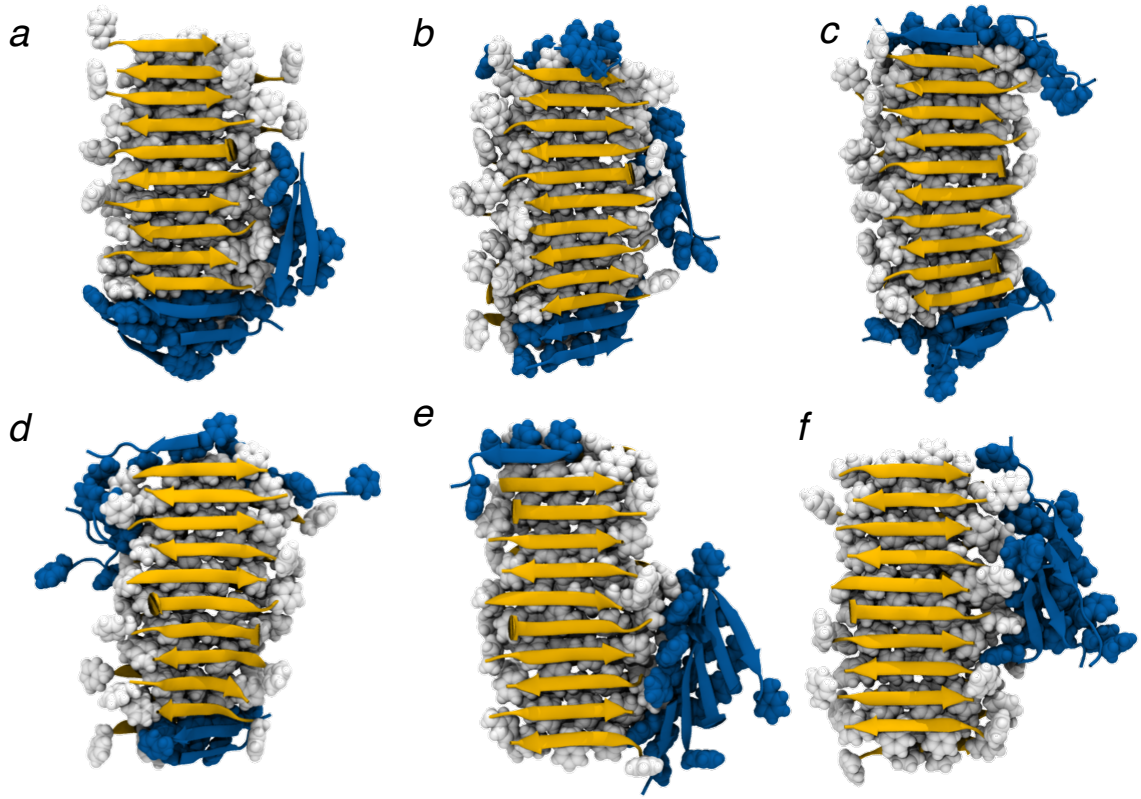

Figure 4.8 Final conformations of 2-μs simulations where six peptides randomly located in the simulation box are allowed to interact with a preformed fibril. A van der Waals representation is used for non-polar residues of the fibril (white) and peptide (blue). A cartoon representation is used for the backbone of the fibril (orange) and peptide (blue).

Seed Formation and Growth. Final conformations of six 2-μs simulations are shown in Figure 4.8. In four of these simulations (panels a-d), most of the six peptides contributed to the elongation of the fibril by locking onto its tip. In two of the simulations (panels e-f), most of the peptides formed oligomeric structures at the fibril edge. In particular, a single β-sheet and a cross-β structure became adsorbed onto the fibril edge in panels e and f, respectively. In these two simulations, the sequence of events leading to the formation of oligomeric structures is illustrated in Figure 4.9. In both cases shown in panels a and b, two or three peptides are attracted towards each other at the edge of the fibril where they form small aggregates. Non-polar

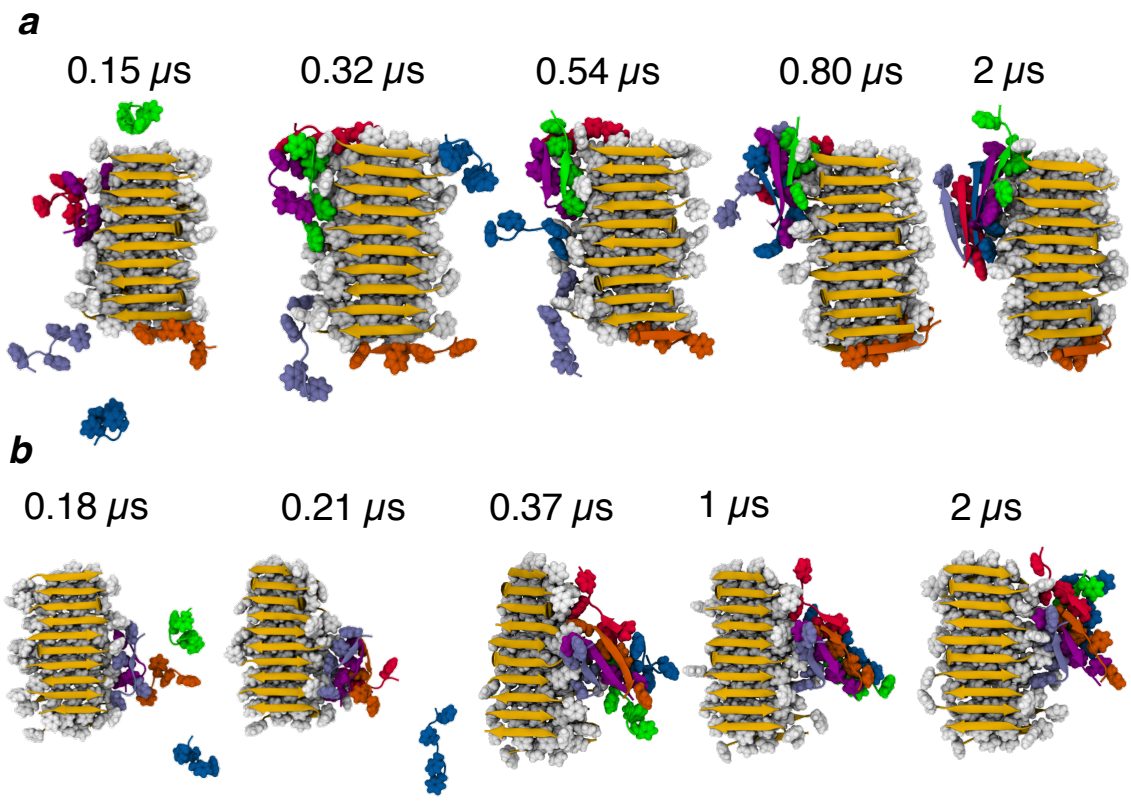

Figure 4.9 Sequence of events leading to the formation of a nucleus on the surface of a preformed fibril (in orange and white) from six peptides deposited randomly in the simulation box. a) Events leading to the formation of the structures in Figure 4.8e. b) Events leading to the structure in Figure 4.8f. Each peptide is shown using a different color.

residues of these aggregates reduce their exposure to the solvent by facing the edge of the fibril and/or by facing non-polar residues of nearby peptides. This leads to the formation of a small β-sheet made from two peptides at time 0.54 μs in panel a, which elongates into a pentamer at the end of the simulation. In panel b, a small cross-β structure formed early in the simulation (i.e., time 0.37 μs) and it remained stable until the end.

To study the growth of stable seeds on the fibril surface, we added six free-peptides to the solvated box containing the configuration shown in Figure 4.8f. These free-peptides are at an initial distance of at least 2 nm from the fibril-seed complex. A 0.5 μs simulation of this system was carried at 350 K and its final configuration was used as the starting point of a new simulation with six free-peptides added to

the box. This process of adding six solvated peptides to the simulation box was repeated another three times such that the final box comprises 36 "free-peptides" and a pre-formed fibril made of 20 peptides. Final configurations after each of these steps are depicted in Figure 4.10 showing the growth of both the pre-formed fibril and the seed. Whereas one would expect a growth rate twice as large for the pre-formed fibril that has two tips exposed to the solvent, Figure 4.10e shows that a similar number of peptides are incorporated onto the seed and the fibril. One may speculate that the larger exposure of non-polar side chains around the seed's tip enables it to adsorb peptides more promptly than each of the fibril's tip. Interestingly, the non-polar edge of the pre-formed fibril located on the opposite side of the nucleus is mostly depleted of free-peptides at the end of the simulation–see panel e. This accumulation of peptides on just one of the non-polar faces of fibrils was also observed in Discrete Molecular Dynamics (DMD) simulations [171].

Recent cryo-EM studies have shown that Ac-$(FKFE)_2$-NH_2 peptides form nanotubes made with four or six amyloid fibrils with main axis pointing in the same direction, and which are are concentrically distributed around the surface of a cylinder. The formation of these supramolecular structures can start with the independent nucleation of different fibrils in solution, which would subsequently come together to form nanotubes. Whereas this scenario for nanotube formation is possible, primary nucleation takes place at a much slower rate than secondary nucleation for most amyloid peptides. Thus, a more plausible scenario is that one fibril is formed via primary nucleation and the other fibrils accounting for the nanotube are catalyzed at its surface. Our simulations are showing that these catalyzed fibrils emerge perpendicularly (not parallel) to the parent fibril. Accordingly, parent and daughter fibrils have to rotate in order to become aligned with each other, which could be driven by hydrophobic interactions between non-polar edges of emergent and parent fibrils. Thus, nanotube formation may emerge from nucleation events

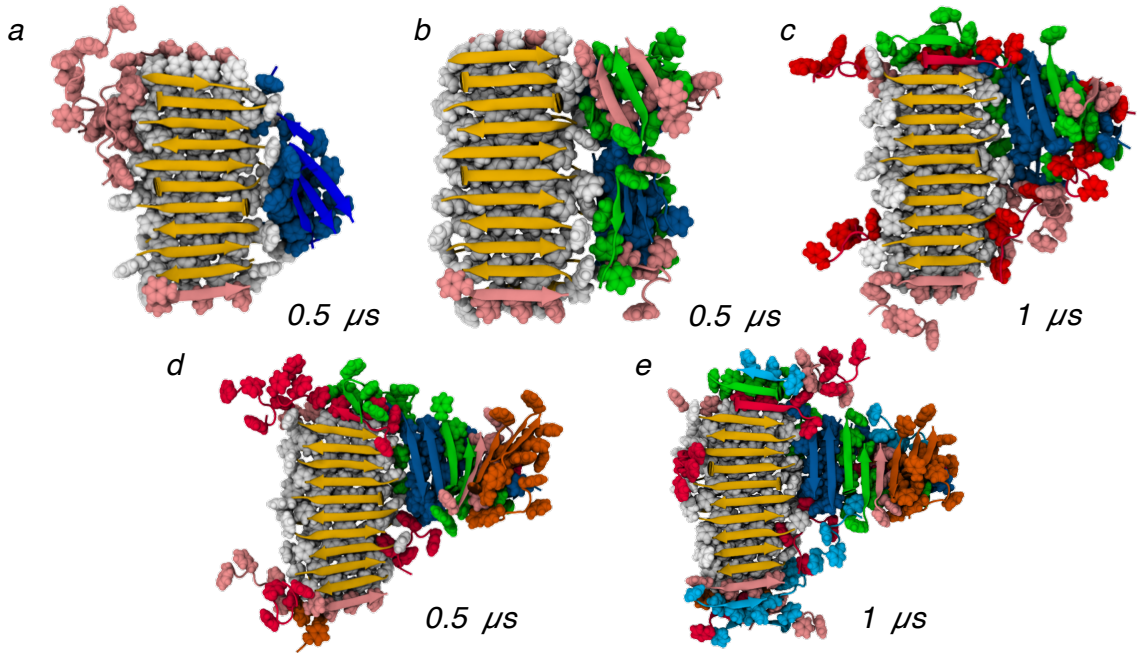

Figure 4.10 Growth of a new nucleus (blue) on the surface of a preformed fibril (white and orange) through the consecutive addition of six peptides to the simulation box. Peptides are colored in pink, green, red, orange/yellow, and cyan according to the order in which they are added to the simulation box. After each addition of six peptides, a 0.5 μs or a 1 μs simulation (as indicated in the figure) is performed to allow peptides to bind to the fibril. Final configurations are shown with the backbone of the preformed fibril illustrate in orange using a cartoon representation. A van der Waals representation is used for non-polar residues.

at the surface of parent and daughter fibrils followed by rotation. Although, this proposed mechanism of nanotube formation is speculative its initial steps including the orientations of daughter fibrils with respect to parent fibril is supported by our simulations.

4.3 Conclusions

In summary, the unbiased nature of our simulations allowed us to provide new insights into the pathways accounting for nucleation and growth of amyloid fibrils from a short amphipathic peptide. In particular, we identified a new intermediate state (i.e., the perpendicular cross-β pattern), which may be used as a target for small molecules to inhibit primary nucleation–see Figure 4.11. If this intermediate state is found to be a general metastable state for a broad class of peptides, this result could have

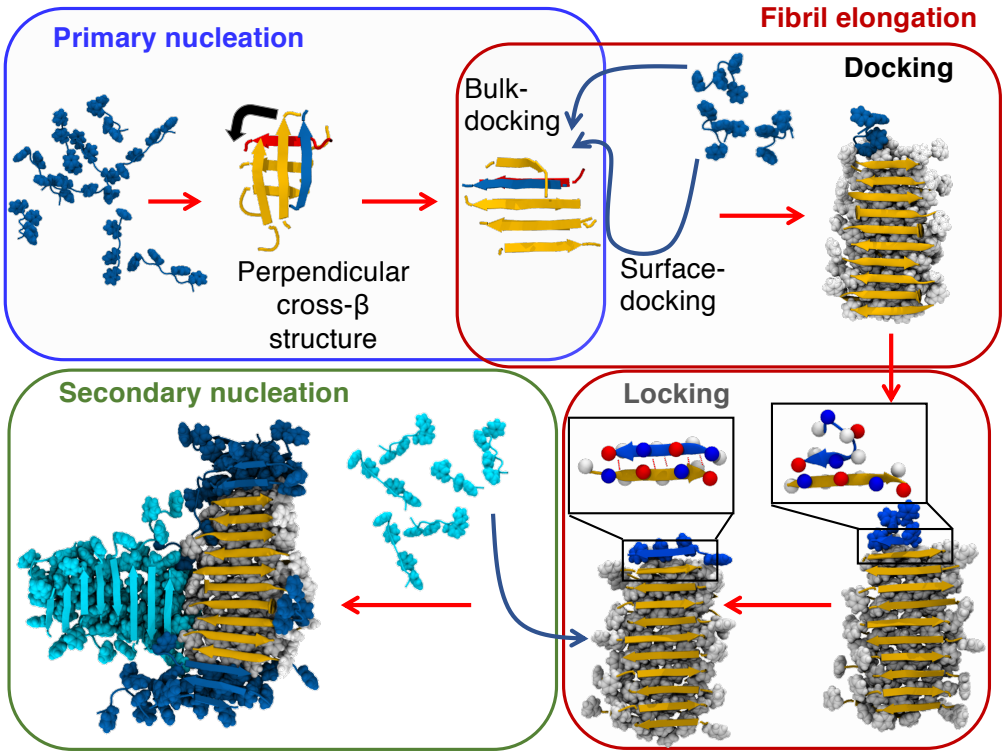

Figure 4.11 Schematic representation of the intermediate states and pathways accounting for fibril formation of Ac-$(FKFE)_2$-NH_2 peptides in our simulations. BLUE: primary nucleation proceeds via the formation of perpendicular cross-β structures. Rotation of β-sheets in the latter leads to the emergence of the amyloid spine. RED (Upper): docking proceeds with peptides diffusing in solution or on the fibril edge to land on the tip. RED (Bottom): step-wise-locking proceeds with the alignment of side chains at different extremities of the peptide with the fibril. Positively charged residues (K) and negatively charged residues (E) are shown in blue and red, respectively. GREEN: peptides (light blue) aggregate at the non-polar edge of the fibril where new fibrils are nucleated.

important implications for reducing amyloid toxicity in amyloid diseases. In addition, we observed a new docking mechanism by which peptides reach the fibril tip by diffusing along its surface–see Figure 4.11. Our simulations suggest that this pathway contributes significantly to populate the fibril tip with peptides. Our simulations are also contributing to the debate of how peptides lock onto the fibril tip. In particular, we found that peptides are not able to align themselves with the template provided by the fibril tip by randomly sampling over different conformations. This alignment was, however, reproduced with atomic fidelity when the conformational change of the

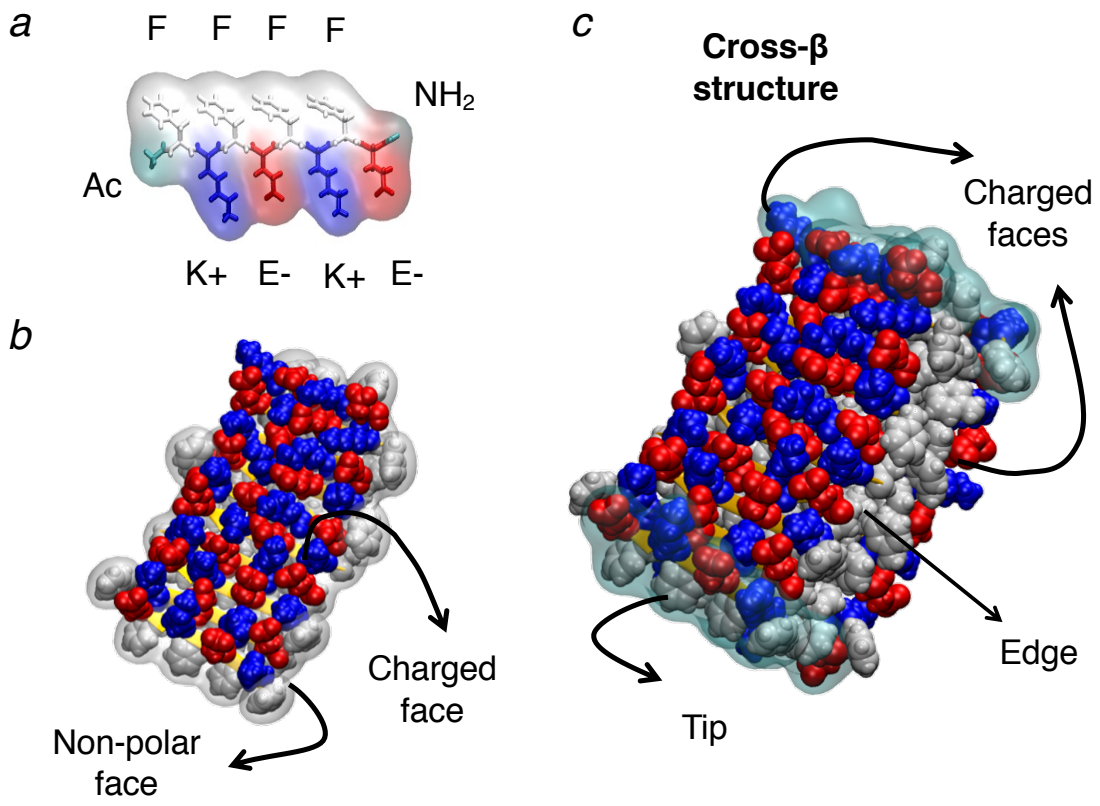

Figure 4.12 Amino acid sequence, β-sheet, and amyloid fibril from an amphipathic peptide. (a) Non-polar phenylalanine (F), positively charged lysine (K), and negatively charged glutamic acid (E) are the three amino acids used to account for the amphipathic Ac-$(FKFE)_2$-NH_2 peptide. (b) Non-polar and charged residues are segregated to different faces of anti-parallel β-sheet. (c) packing of non-polar faces of two β-sheets against each other accounts for the cross-β structure of amyloid fibrils. Non-polar edges and tips are highlighted in the figure.

docked peptide was driven by side chain interactions between charged residues–see Figure 4.11. Thus, we anticipate that screen electrostatic interactions by adding salt to the solution may have a strong effect on the lock process of our amphipathic peptide. Our simulations also provided insights into aggregation of peptides on the fibril surface (see Figure 4.11), which may be associated with the formation of supramolecular structures from many fibrils.

The novel insights brought up by this study required tracking a large number of atoms (more than $200,000$ atoms to account for peptide concentrations of $\sim$10 mM) for a long time (> 2 μs) [197, 198, 161]. The high computational cost associated with

these calculations were previously not easily accessible to the scientific community. Accordingly, previous unbiased all-atom simulations in explicit solvent were mostly performed in boxes containing a small number (< 10) of short peptides and for a timescale that is too short to allow for the formation of cross-β structures or to track docking via surface diffusion. Therefore, these studies only provided limited insights into the existence of intermediate states and mostly ignore the surface-docking pathway. In the same vein, the timescale associated with locking onto the fibril tip is beyond reach of all-atom simulations for full-length amyloid peptides. Thus, previous computational studies have focused on the dissociation of peptide from the tip and insights into the locking-phase were obtained using coarse grain models.

It is important to highlight that simulations in this chapter were performed at high temperature, i.e., 325 K or 350 K. Previously[162], the latter temperatures were shown to speed up the aggregation process allowing us in this current study to investigate fibril formation in a reasonable time-frame. The anticipated increase in the number-crunching power of supercomputers will make it possible to test the validity of the mechanisms put forward by our simulations at ambient and body temperature. It will also be relevant to test the scope of our results for other peptide sequences. Are perpendicular cross-β structures intermediate states for a broad class of peptides? Which peptide sequences populate the fibril tip via a combination of bulk- and surface-docking pathways? If full-length amyloid peptides fall within the same class of peptides as $(FKFE)_2$, we anticipate that the microscopic mechanisms proposed here will have important implications for reducing amyloid toxicity in diseases.

4.4 Methods

Peptide Chemistry. In this chapter, we study the self-assembly mechanisms of an amphipathic peptide made from eight-residues that alternate between non-polar and charged amino acids. Phenylalanine, represented by the one amino acid letter code **F**,

is used as the non-polar amino acid. Positive lysine (**K**) and negative glutamic acid (**E**) are used for charged amino acids. The peptide is capped with acetyl (Ac) and amide (NH_2) groups at N- and C-terminal, respectively, accounting for the neutral Ac-(**F**K**F**E)$_2$-NH_2 sequence –see Figure 4.12a.This peptide was shown to promptly self-assemble into amyloid-like fibrils both experimentally and in computer simulations [197, 199, 200, 201, 202]. Furthermore, recent cryo-em images revealed that the supramolecular assembly of these fibrils emerge from the concentric juxtaposition of four- and six-fibrils accounting for *thin* and *thick* nanotubes [203].

Force Field and System Equilibration. Molecular dynamics simulations were performed with the Amber99SB-ILDN force field [61] and the TIP3P water model using cubic boxes and periodic boundary conditions in the isothermal-isobaric (NPT) ensemble. The Parrinello-Rahman barostat ($\tau_p = 2.0$ ps) was used to maintain the pressure of the system at 1 bar [80]. Temperature was controlled by coupling protein and solvent separately to a velocity-rescale thermostat ($\tau_t = 0.1$ ps). The equations of motion were integrated using the leapfrog algorithm with a 2 fs time-step [55]. The cut-off for short range van der Waals and electrostatic interactions was 1.0 nm and the smooth Particle Mesh Ewald algorithm was used to compute long range electrostatic interactions [81]. Systems studied here were equilibrated in the NVT and NPT ensembles for 100 ps. All simulations were performed using the 2020 version of GROMACS [204]. A description of the different setups used to study primary and secondary nucleation as well as fibril elongation is provided in the result section.

Analysis. Various quantities were used to analyze the different trajectories using GROMACS toolkit. This includes the minimal distance between backbone atoms of all pairs of peptides, and the peptide secondary structure content computed using DSSP. An in-house code was used to compute the largest aggregate (or cluster) made from peptides with a minimal distance of less than 0.5 nm from each other. The

number of peptides within this cluster is used to determine the formation of stable nuclei during primary nucleation.

The geometry of hydrogen (H), donor (D), and acceptor (A) atoms is used to define the formation of hydrogen bonds. In particular, a hydrogen bond is formed if the donor-acceptor distance is less or equal to 0.35 nm, and the H-D-A angle is found to be less than 30^{o}. Using this default definition, peptides are considered to be part of a β-sheet if they formed at least four backbone hydrogen bonds with each other. This was used to determine the number of peptides forming each of the two β-sheets in the cross-β structure in primary nucleation.

CHAPTER 5

SUMMARY AND FUTURE WORK

5.1 Major Results of this Dissertation

Amyloid peptides are associated with various neuro-degenerative diseases including Alzheimer's and Parkinson's [205, 206]. These peptides self-assemble into highly ordered β-sheet assemblies known as amyloid fibrils. In this dissertation, we addressed the three microscopic mechanisms that account for the formation of these fibrils using all-atom molecular dynamics simulations in explicit solvent [207, 208]. These mechanisms are primary nucleation, fibril elongation, and secondary nucleation, which are studied in Chapters 2, 3 and 4 of this dissertation.

In Chapter 2, we studied the spontaneous aggregation of amphipathic peptides into fibril-like structures using large boxes containing many atoms and long-time simulations. Simulations were performed for various peptide sequences in solutions with and without NaCl and at different temperatures [209, 210]. The results show that increasing temperature increases the aggregation rate for amphipathic peptides made with highly hydrophobic amino acids. Since the strength of hydrophobic interactions is well known to increase with increasing temperature [91, 92, 93, 94, 95], this result suggests that hydrophobic interactions drive peptide aggregation. Moreover, effects of NaCl on aggregation was investigated for peptides made with non-polar residues that are weakly hydrophobic. In the absence of NaCl, these peptides interact mainly via electrostatic interactions. The addition of salt screens these electrostatic interactions increasing the peptide's propensity to aggregate. This result provides insights on how to promote fibril formation by adding salt to the solution, which is consistent with experimental studies [79]. Finally, we performed simulations with peptides made from the same amino acids located at different positions in the sequence. Our analysis

shows that sequences with a low propensity to form β-structures and inter-hydrogen bonds in our simulations did not form fibrils experimentally [70, 72]. This positive correlation between experiments and in silico studies provides proof of concept that MD simulation can be used to predict fibril formation and provide atomic level insights into this phenomena [197].

After confirming that our MD simulations provide consistent results with experiments, we investigated the mechanisms involved in fibril formation. In Chapter 3, we performed all-atom simulations in explicit solvent at 298 K, 325 K, and 350 K to provide insights into the mechanisms accounting for fibril elongation. These simulations are performed in large boxes ($10.1 \times 10.1 \times 10.1\ nm^3$) containing a preformed fibril and a solvated peptide. When simulations are performed for a very long time, the peptide spontaneously becomes incorporated into the fibril tip via a dock-and-lock mechanism [211, 212, 185, 189]. Analysis of the trajectories obtained from these simulations reveals two elongation pathways, and they allowed us to provide insights into how the peptide locks itself onto the fibril, reproducing the structure dictated by the tip with atomic fidelity. In the first pathway, the peptide binds to the tip directly from the bulk and elongates the fibril, i.e., bulk-docking. In the second pathway, the peptide binds to the surface of the fibril and reaches the tip by diffusing along it, i.e., surface-docking. To the best of our knowledge, the latter mechanism has not been discussed in the literature. Moreover, our unbiased simulations show that peptides spontaneously lock onto the fibril tip via the formation of hydrogen bonds. At 325 K, the peptide aligns itself with the fibril tip reproducing its structure with high fidelity. We show that this process is driven by side chain interactions. While at 350 K, the peptide moves more randomly on the fibril until forming enough hydrogen bonds with the tip to become locked. At the latter temperature, peptides rarely reproduced the structure of the tip with atomic fidelity.

In Chapter 4, we explored mechanisms accounting for the nucleation and growth of amyloid-like fibrils using long unbiased MD simulations. First, we studied the spontaneous nucleation of cross-β structures in solution, i.e., primary nucleation. The analysis of the simulations shows that small aggregates undergo a structural transition to form two laminated β-sheets that are oriented perpendicularly to each other. Growth of this aggregate emerges after these β-sheets rotate to become oriented parallel to each other. Second, we explored the secondary nucleation mechanism in which cross-β structures form on the fibril surface. Our results show that after peptides are attracted to the fibril surface, they can diffuse toward each other and aggregate on the hydrophobic patches of the surface, which leads to the formation of β-sheets. As the number of peptides on the surface increases, the likelihood of formation of the cross-β structures increases. In our simulations, the nucleus forms and grows on the surface with its main axis perpendicular to the fibril.

5.2 Limitations of this Dissertation

The findings in this dissertation can contribute significantly to the detailed understanding of the mechanisms involved in fibril formation. While several limitations need to be acknowledged. First, the simulations were performed in simplified conditions, either in pure water or in the presence of NaCl. However, the physiological environment exhibits greater complexity that are unknown for us. This limitation may be resolved by modeling the systems closer to the actual physiological condition in the presence of NaCl, $CaCl_2$, lipids, and other charged ions in the future [213]. Second, we employed short peptides to study the aggregation of the fibril and the mechanisms accounting for the fibril growth. More details can be obtained from longer protein sequences by accessing powerful computational resources. Third, the force field used in the simulations played an important role in the accuracy of the modeling [198]. We chose Amber99SB-ILDN, which shows a positive correlation with experimental

results. Despite the limitations, our results lay the groundwork for future studies with a broader range of solution conditions.

5.3 Foreseeable Future Work

Previous studies have provided valuable insights into the aggregation of disordered structures using all-atom simulations on short-time scales ($< 1\ \mu s$). However, these studies were not able to simulate the formation of long ordered cross-β structures, which requires tracking a large number of atoms ($>$ 200,000 atoms to account for peptide concentrations of 10 mM) for many time-steps ($> 2\ \mu$s) [160, 214, 215, 216, 164, 77].

In this dissertation, we showed that, with the performance of today's computers, MD simulations can be used to study the formation of ordered fibril-like structures for short peptide sequences. We used these simulations to provide new insights into the mechanisms of fibril formation. Specifically, these insights may contribute to develop new strategies to treat diseases, e.g., to rationally design the drugs that can target intermediate states on the pathway to fibril formation. They may also enable the development of novel sequence-structure predictive tools, which may be used to design new biomaterials.

We anticipate that interesting new insights to understand amyloid diseases will be obtained by expanding the work of this dissertation to different peptide sequences. In particular, it will be interesting to explore secondary nucleation when the amino acid sequence of the parent fibril and nucleus differ from each other, i.e., cross-seeding. This type of co-assembly was shown to be relevant in Alzheimer's diseases where amyloid fibril catalyzes the formation of toxic oligomers [217, 218, 219, 220]. We also anticipate that exploring the effects of different solvent conditions (e.g., the presence of lipid bilayers and pH) on aggregation will provide insights into fibril growth under more realistic conditions in the brain.

REFERENCES

[1] F. Vella, *Biochemistry. by J. Stenesh.* New York, NY, United States: Plenum Press, 1999.

[2] O. M. Becker, A. D. MacKerell Jr, B. Roux, and M. Watanabe, *Computational biochemistry and biophysics.* Boca Raton, FL, United States: Crc Press, 2001.

[3] M. Wiltgen, "Algorithms for structure comparison and analysis: homology modelling of proteins," *Encyclopedia of Bioinformatics and Computational Biology; Ranganathan, S., Gribskov, M., Nakai, K., Schönbach, C., Eds*, pp. 38–61, 2018.

[4] S. Ranganathan, K. Nakai, and C. Schonbach, *Encyclopedia of Bioinformatics and Computational Biology: ABC of Bioinformatics.* Amsterdam, Netherlands: Elsevier, 2018.

[5] F. Chiti and C. M. Dobson, "Protein misfolding, amyloid formation, and human disease: a summary of progress over the last decade," *Annual Review of Biochemistry*, vol. 86, pp. 27–68, 2017.

[6] O. S. Makin and L. C. Serpell, "Structures for amyloid fibrils," *The Federation of European Biochemical Societies Journal*, vol. 272, no. 23, pp. 5950–5961, 2005.

[7] M. Sunde and C. Blake, "The structure of amyloid fibrils by electron microscopy and x-ray diffraction," *Advances in Protein Chemistry*, vol. 50, pp. 123–159, 1997.

[8] Z. L. Almeida and R. M. Brito, "Structure and aggregation mechanisms in amyloids," *Molecules*, vol. 25, no. 5, p. 1195, 2020.

[9] P. Braun and A.-C. Gingras, "History of protein–protein interactions: From egg-white to complex networks," *Proteomics*, vol. 12, no. 10, pp. 1478–1498, 2012.

[10] A. D. Cunningham, N. Qvit, and D. Mochly-Rosen, "Peptides and peptidomimetics as regulators of protein–protein interactions," *Current Opinion in Structural Biology*, vol. 44, pp. 59–66, 2017.

[11] M. J. Lopez and S. S. Mohiuddin, *Biochemistry, essential amino acids.* Treasure Island, FL, United States: StatPearls Publishing, 2021.

[12] S. Maloy and K. Hughes, *Brenner's encyclopedia of genetics.* Amsterdam, Netherlands: Academic Press, 2013.

[13] C. I. Branden and J. Tooze, *Introduction to protein structure.* New York, NY, United States: Garland Science, 2012.

[14] M. M. Gromiha, *Protein bioinformatics: from sequence to function.* Kalkaji, New Delhi, India: Academic Press, 2010.

[15] N. Kandhari and S. Sinha, "Complex network analysis of thermostable mutants of bacillus subtilis lipase a," *Applied Network Science*, vol. 2, pp. 1–16, 2017.

[16] J. M. Berg, J. L. Tymoczko, and L. Stryer, *Biochemistry.* New York, NY, United States: W. H. Freeman and Company, 2006.

[17] K. Wendler, J. Thar, S. Zahn, and B. Kirchner, "Estimating the hydrogen bond energy," *The Journal of Physical Chemistry A*, vol. 114, no. 35, pp. 9529–9536, 2010.

[18] V. Brázdová and D. R. Bowler, *Atomistic Computer Simulations: A Practical Guide.* Weinheim, Germany: WILEY-VCH Verlag GmbH and Co. KG aA, 2013.

[19] T. D. Pollard, W. C. Earnshaw, J. Lippincott-Schwartz, and G. Johnson, "Chapter 4-biophysical principles," *Cell Biology (Third Edition)*, pp. 53–62, 2017.

[20] C. S. Tsai, *An introduction to computational biochemistry.* New York, NY, United States: John Wiley & Sons, 2003.

[21] D. Eisenberg and M. Jucker, "The amyloid state of proteins in human diseases," *Cell*, vol. 148, no. 6, pp. 1188–1203, 2012.

[22] R. Nelson, M. R. Sawaya, M. Balbirnie, A. Ø. Madsen, C. Riekel, R. Grothe, and D. Eisenberg, "Structure of the cross-β spine of amyloid-like fibrils," *Nature*, vol. 435, no. 7043, pp. 773–778, 2005.

[23] W. T. Astbury, S. Dickinson, and K. Bailey, "The x-ray interpretation of denaturation and the structure of the seed globulins," *Biochemical Journal*, vol. 29, no. 10, p. 2351, 1935.

[24] R. Riek, "The three-dimensional structures of amyloids," *Cold Spring Harbor Perspectives in Biology*, vol. 9, no. 2, p. a023572, 2017.

[25] L. Pauling and R. B. Corey, "The pleated sheet, a new layer configuration of polypeptide chains," *Proceedings of the National Academy of Sciences of the United States of America*, vol. 37, no. 5, p. 251, 1951.

[26] E. Eanes and G. Glenner, "X-ray diffraction studies on amyloid filaments," *Journal of Histochemistry & Cytochemistry*, vol. 16, no. 11, pp. 673–677, 1968.

[27] T. L. Benzinger, D. M. Gregory, T. S. Burkoth, H. Miller-Auer, D. G. Lynn, R. E. Botto, and S. C. Meredith, "Propagating structure of alzheimer's β-amyloid (10–35) is parallel β-sheet with residues in exact register," *Proceedings of the National Academy of Sciences*, vol. 95, no. 23, pp. 13 407–13 412, 1998.

[28] R. Nelson, M. R. Sawaya, M. Balbirnie, A. Ø. Madsen, C. Riekel, R. Grothe, and D. Eisenberg, "Structure of the cross-β spine of amyloid-like fibrils," *Nature*, vol. 435, no. 7043, pp. 773–778, 2005.

[29] J. L. Jimenez, J. I. Guijarro, E. Orlova, J. Zurdo, C. M. Dobson, M. Sunde, and H. R. Saibil, "Cryo-electron microscopy structure of an sh3 amyloid fibril and model of the molecular packing," *The European Molecular Biology Organization Journal*, vol. 18, no. 4, pp. 815–821, 1999.

[30] H. Van Melckebeke, C. Wasmer, A. Lange, E. Ab, A. Loquet, A. Böckmann, and B. H. Meier, "Atomic-resolution three-dimensional structure of het-s (218-289) amyloid fibrils by solid-state nmr spectroscopy," *Journal of the American Chemical Society*, vol. 132, no. 39, pp. 13 765–13 775, 2010.

[31] M. R. Sawaya, S. Sambashivan, R. Nelson, M. I. Ivanova, S. A. Sievers, M. I. Apostol, M. J. Thompson, M. Balbirnie, J. J. Wiltzius, H. T. McFarlane *et al.*, "Atomic structures of amyloid cross-β spines reveal varied steric zippers," *Nature*, vol. 447, no. 7143, pp. 453–457, 2007.

[32] Y.-r. Huang and R.-t. Liu, "The toxicity and polymorphism of β-amyloid oligomers," *International Journal of Molecular Sciences*, vol. 21, no. 12, p. 4477, 2020.

[33] E. Chatani and N. Yamamoto, "Recent progress on understanding the mechanisms of amyloid nucleation," *Biophysical Reviews*, vol. 10, no. 2, pp. 527–534, 2018.

[34] J. D. Sipe and A. S. Cohen, "History of the amyloid fibril," *Journal of Structural Biology*, vol. 130, no. 2-3, pp. 88–98, 2000.

[35] K. E. Marshall, D. M. Vadukul, L. Dahal, A. Theisen, M. W. Fowler, Y. Al-Hilaly, L. Ford, G. Kemenes, I. J. Day, K. Staras *et al.*, "A critical role for the self-assembly of amyloid-β1-42 in neurodegeneration," *Scientific Reports*, vol. 6, no. 1, pp. 1–13, 2016.

[36] M. I. Sulatsky, O. V. Stepanenko, O. V. Stepanenko, E. V. Mikhailova, I. M. Kuznetsova, K. K. Turoverov, and A. I. Sulatskaya, "Amyloid fibrils degradation: the pathway to recovery or aggravation of the disease?" *Frontiers in Molecular Biosciences*, vol. 10, p. 1208059, 2023.

[37] A. G. Cheetham, P. Zhang, Y.-a. Lin, L. L. Lock, and H. Cui, "Supramolecular nanostructures formed by anticancer drug assembly," *Journal of the American Chemical Society*, vol. 135, no. 8, pp. 2907–2910, 2013.

[38] R. S. Jacob, E. George, P. K. Singh, S. Salot, A. Anoop, N. N. Jha, S. Sen, and S. K. Maji, "Cell adhesion on amyloid fibrils lacking integrin recognition motif," *Journal of Biological Chemistry*, vol. 291, no. 10, pp. 5278–5298, 2016.

[39] S. L. Gras, A. K. Tickler, A. M. Squires, G. L. Devlin, M. A. Horton, C. M. Dobson, and C. E. MacPhee, "Functionalised amyloid fibrils for roles in cell adhesion," *Biomaterials*, vol. 29, no. 11, pp. 1553–1562, 2008.

[40] X. Zottig, M. Côté-Cyr, D. Arpin, D. Archambault, and S. Bourgault, "Protein supramolecular structures: From self-assembly to nanovaccine design," *Nanomaterials*, vol. 10, no. 5, p. 1008, 2020.

[41] A. M. Kushner and Z. Guan, "Modular design in natural and biomimetic soft materials," *Angewandte Chemie International Edition*, vol. 50, no. 39, pp. 9026–9057, 2011.

[42] C. J. Edwards-Gayle and I. W. Hamley, "Self-assembly of bioactive peptides, peptide conjugates, and peptide mimetic materials," *Organic and Biomolecular Chemistry*, vol. 15, no. 28, pp. 5867–5876, 2017.

[43] A. Dehsorkhi, V. Castelletto, and I. W. Hamley, "Self-assembling amphiphilic peptides," *Journal of Peptide Science*, vol. 20, no. 7, pp. 453–467, 2014.

[44] L. Deng, P. Zhou, Y. Zhao, Y. Wang, and H. Xu, "Molecular origin of the self-assembled morphological difference caused by varying the order of charged residues in short peptides," *The Journal of Physical Chemistry B*, vol. 118, no. 43, pp. 12 501–12 510, 2014.

[45] G. M. Whitesides and M. Boncheva, "Beyond molecules: Self-assembly of mesoscopic and macroscopic components," *Proceedings of the National Academy of Sciences*, vol. 99, no. 8, pp. 4769–4774, 2002.

[46] S. Zhang, D. M. Marini, W. Hwang, and S. Santoso, "Design of nanostructured biological materials through self-assembly of peptides and proteins," *Current Opinion in Chemical Biology*, vol. 6, no. 6, pp. 865–871, 2002.

[47] A. Morriss-Andrews and J.-E. Shea, "Computational studies of protein aggregation: methods and applications," *Annual Review of Physical Chemistry*, vol. 66, pp. 643–666, 2015.

[48] B. Strodel, "Amyloid aggregation simulations: challenges, advances and perspectives," *Current Opinion in Structural Biology*, vol. 67, pp. 145–152, 2021.

[49] M. Abraham, D. Van Der Spoel, E. Lindahl, and B. Hess, "the gromacs development team," *GROMACS User Manual Version*, vol. 5, no. 2, pp. 1–298, 2014.

[50] A. Kukol *et al.*, *Molecular modeling of proteins*. Totowa, NJ, United States: Humana Press, 2008, vol. 443.

[51] F. Ercolessi, "A molecular dynamics primer," *Spring College in Computational Physics, ICTP, Trieste*, vol. 19, 1997.

[52] D. C. Rapaport and D. C. R. Rapaport, *The art of molecular dynamics simulation*. Cambridge, United Kingdom: Cambridge University Press, 2004.

[53] D. Frenkel and B. Smit, *Understanding molecular simulation: from algorithms to applications*. San Diego, CA, United States: Academic Press, 2001, vol. 1.

[54] W. C. Swope, H. C. Andersen, P. H. Berens, and K. R. Wilson, "A computer simulation method for the calculation of equilibrium constants for the formation of physical clusters of molecules: Application to small water clusters," *The Journal of Chemical Physics*, vol. 76, no. 1, pp. 637–649, 1982.

[55] M. P. Allen and D. J. Tildesley, *Computer simulation of liquids*, 2nd ed. London, England: Oxford University Press, May 2017.

[56] P. H. Hünenberger, "Thermostat algorithms for molecular dynamics simulations," *Advanced Computer Simulation: Approaches for Soft Matter Sciences I*, pp. 105–149, 2005.

[57] S. Sharma, *Molecular dynamics simulation of nanocomposites using BIOVIA materials studio, lammps and gromacs*. Amsterdam, Neatherlands: Elsevier, 2019.

[58] R. M. Betz and R. C. Walker, "Paramfit: Automated optimization of force field parameters for molecular dynamics simulations," *Journal of Computational Chemistry*, vol. 36, no. 2, pp. 79–87, 2015.

[59] S. Genheden, A. Reymer, P. Saenz-Méndez, and L. A. Eriksson, "Computational chemistry and molecular modelling basics," 2017.

[60] M. Bhandarkar, R. Brunner, C. Chipot, A. Dalke, S. Dixit, P. Grayson, J. Gullingsrud, A. Gursoy, D. Hardy, W. Humphrey *et al.*, "Namd user's guide (theoretical biophysics group, university of illinois at urbana-champaign and beckman institute, urbana)," 2003.

[61] K. Lindorff-Larsen, S. Piana, K. Palmo, P. Maragakis, J. L. Klepeis, R. O. Dror, and D. E. Shaw, "Improved side-chain torsion potentials for the amber ff99sb protein force field," *Proteins: Structure, Function, and Bioinformatics*, vol. 78, no. 8, pp. 1950–1958, 2010.

[62] F. Chiti and C. M. Dobson, "Protein misfolding, functional amyloid, and human disease," *Annual Review Biochemistry.*, vol. 75, pp. 333–366, 2006.

[63] T. P. Knowles, A. W. Fitzpatrick, S. Meehan, H. R. Mott, M. Vendruscolo, C. M. Dobson, and M. E. Welland, "Role of intermolecular forces in defining material properties of protein nanofibrils," *Science*, vol. 318, no. 5858, pp. 1900–1903, 2007.

[64] M. Carballo-Pacheco and B. Strodel, "Advances in the simulation of protein aggregation at the atomistic scale," *The Journal of Physical Chemistry B*, vol. 120, no. 12, pp. 2991–2999, 2016.

[65] C. J. Bowerman and B. L. Nilsson, "Review self-assembly of amphipathic β-sheet peptides: insights and applications," *Peptide Science*, vol. 98, no. 3, pp. 169–184, 2012.

[66] S. Cavalli, F. Albericio, and A. Kros, "Amphiphilic peptides and their cross-disciplinary role as building blocks for nanoscience," *Chemical Society Reviews*, vol. 39, no. 1, pp. 241–263, 2010.

[67] N. R. Lee, C. J. Bowerman, and B. L. Nilsson, "Effects of varied sequence pattern on the self-assembly of amphipathic peptides," *Biomacromolecules*, vol. 14, no. 9, pp. 3267–3277, 2013.

[68] M. R. Sawaya, S. Sambashivan, R. Nelson, M. I. Ivanova, S. A. Sievers, M. I. Apostol, M. J. Thompson, M. Balbirnie, J. J. Wiltzius, H. T. McFarlane *et al.*, "Atomic structures of amyloid cross-β spines reveal varied steric zippers," *Nature*, vol. 447, no. 7143, pp. 453–457, 2007.

[69] D. S. Eisenberg and M. R. Sawaya, "Structural studies of amyloid proteins at the molecular level," *Annual Review of Biochemistry*, vol. 86, pp. 69–95, 2017.

[70] C. J. Bowerman, D. M. Ryan, D. A. Nissan, and B. L. Nilsson, "The effect of increasing hydrophobicity on the self-assembly of amphipathic β-sheet peptides," *Molecular BioSystems*, vol. 5, no. 9, pp. 1058–1069, 2009.

[71] R. J. Betush, J. M. Urban, and B. L. Nilsson, "Balancing hydrophobicity and sequence pattern to influence self-assembly of amphipathic peptides," *Peptide Science*, vol. 110, no. 1, p. e23099, 2018.

[72] A. Saiani, A. Mohammed, H. Frielinghaus, R. Collins, N. Hodson, C. Kielty, M. Sherratt, and A. Miller, "Self-assembly and gelation properties of α-helix versus β-sheet forming peptides," *Soft Matter*, vol. 5, no. 1, pp. 193–202, 2009.

[73] S. Emamyari, F. Kargar, V. Sheikh-Hasani, S. Emadi, and H. Fazli, "Mechanisms of the self-assembly of eak16-family peptides into fibrillar and globular structures: molecular dynamics simulations from nano-to micro-seconds," *European Biophysics Journal*, vol. 44, no. 4, pp. 263–276, 2015.

[74] S. Samantray, F. Yin, B. Kav, and B. Strodel, "Different force fields give rise to different amyloid aggregation pathways in molecular dynamics simulations," *Journal of Chemical Information and Modeling*, vol. 60, no. 12, pp. 6462–6475, 2020.

[75] W. M. Berhanu and U. H. Hansmann, "Side-chain hydrophobicity and the stability of aβ16–22 aggregates," *Protein Science*, vol. 21, no. 12, pp. 1837–1848, 2012.

[76] U. Sengupta, M. Carballo-Pacheco, and B. Strodel, "Automated markov state models for molecular dynamics simulations of aggregation and self-assembly," *The Journal of Chemical Physics*, vol. 150, no. 11, p. 115101, 2019.

[77] D. M. Marini, W. Hwang, D. A. Lauffenburger, S. Zhang, and R. D. Kamm, "Left-handed helical ribbon intermediates in the self-assembly of a β-sheet peptide," *Nano Letters*, vol. 2, no. 4, pp. 295–299, Apr 2002.

[78] W. Hwang, D. M. Marini, R. D. Kamm, and S. Zhang, "Supramolecular structure of helical ribbons self-assembled from a β-sheet peptide," *The Journal of Chemical Physics*, vol. 118, no. 1, pp. 389–397, 2003.

[79] Y. Hong, L. S. Lau, R. L. Legge, and P. Chen, "Critical self-assembly concentration of an ionic-complementary peptide eak16-i," *The Journal of Adhesion*, vol. 80, no. 10-11, pp. 913–931, 2004.

[80] M. Parrinello and A. Rahman, "Polymorphic transitions in single crystals: A new molecular dynamics method," *Journal of Applied physics*, vol. 52, no. 12, pp. 7182–7190, 1981.

[81] P. Bjelkmar, P. Larsson, M. A. Cuendet, B. Hess, and E. Lindahl, "Implementation of the charmm force field in gromacs: analysis of protein stability effects from correction maps, virtual interaction sites, and water models," *Journal of Chemical Theory and Computation*, vol. 6, no. 2, pp. 459–466, 2010.

[82] M. J. Abraham, T. Murtola, R. Schulz, S. Páll, J. C. Smith, B. Hess, and E. Lindahl, "Gromacs: High performance molecular simulations through multi-level parallelism from laptops to supercomputers," *SoftwareX*, vol. 1, pp. 19–25, 2015.

[83] D. E. Shaw, J. Grossman, J. A. Bank, B. Batson, J. A. Butts, J. C. Chao, M. M. Deneroff, R. O. Dror, A. Even, C. H. Fenton *et al.*, "Anton 2: raising the bar for performance and programmability in a special-purpose molecular dynamics supercomputer," in *SC'14: Proceedings of the International Conference for High Performance Computing, Networking, Storage and Analysis*. IEEE, 2014, pp. 41–53.

[84] X. Hu, M. Liao, H. Gong, L. Zhang, H. Cox, T. A. Waigh, and J. R. Lu, "Recent advances in short peptide self-assembly: from rational design to novel applications," *Current Opinion in Colloid and Interface Science*, vol. 45, pp. 1–13, 2020.

[85] S. Samantray, W. Schumann, A.-M. Illig, M. Carballo-Pacheco, A. Paul, B. Barz, and B. Strodel, "Molecular dynamics simulations of protein aggregation: protocols for simulation setup and analysis with markov state models and transition networks," *BioRxiv*, 2020.

[86] R. J. Gowers, M. Linke, J. Barnoud, T. J. E. Reddy, M. N. Melo, S. L. Seyler, J. Domanski, D. L. Dotson, S. Buchoux, I. M. Kenney *et al.*, "Mdanalysis: a python package for the rapid analysis of molecular dynamics simulations," Los Alamos National Lab., Los Alamos, NM, Tech. Rep., 2019.

[87] N. Michaud-Agrawal, E. J. Denning, T. B. Woolf, and O. Beckstein, "Mdanalysis: a toolkit for the analysis of molecular dynamics simulations," *Journal of Computational Chemistry*, vol. 32, no. 10, pp. 2319–2327, 2011.

[88] R. T. McGibbon, K. A. Beauchamp, M. P. Harrigan, C. Klein, J. M. Swails, C. X. Hernández, C. R. Schwantes, L.-P. Wang, T. J. Lane, and V. S. Pande, "Mdtraj: a modern open library for the analysis of molecular dynamics trajectories," *Biophysical Journal*, vol. 109, no. 8, pp. 1528–1532, 2015.

[89] W. Kabsch and C. Sander, "Dictionary of protein secondary structure: pattern recognition of hydrogen-bonded and geometrical features," *Biopolymers: Original Research on Biomolecules*, vol. 22, no. 12, pp. 2577–2637, 1983.

[90] M. Cao, Y. Shen, Y. Wang, X. Wang, and D. Li, "Self-assembly of short elastin-like amphiphilic peptides: Effects of temperature, molecular hydrophobicity and charge distribution," *Molecules*, vol. 24, no. 1, p. 202, 2019.

[91] W. Kauzmann, "Some factors in the interpretation of protein denaturation," in *Advances in Protein Chemistry*. New York, NY, United States: Acadelic press, 1959, vol. 14, pp. 1–63.

[92] K. A. Dill, "Dominant forces in protein folding," *Biochemistry*, vol. 29, no. 31, pp. 7133–7155, 1990.

[93] C. L. Dias, T. Hynninen, T. Ala-Nissila, A. S. Foster, and M. Karttunen, "Hydrophobicity within the three-dimensional mercedes-benz model: Potential of mean force," *The Journal of Chemical Physics*, vol. 134, no. 6, p. 02B620, 2011.

[94] C. L. Dias, T. Ala-Nissila, J. Wong-ekkabut, I. Vattulainen, M. Grant, and M. Karttunen, "The hydrophobic effect and its role in cold denaturation," *Cryobiology*, vol. 60, no. 1, pp. 91–99, 2010.

[95] Z. Su and C. L. Dias, "Driving β-strands into fibrils," *The Journal of Physical Chemistry B*, vol. 118, no. 37, pp. 10 830–10 836, 2014.

[96] F. Mahmoudinobar, B. L. Nilsson, and C. L. Dias, "Effects of ions and small compounds on the structure of aβ42 monomers," *The Journal of Physical Chemistry B*, vol. 125, no. 4, pp. 1085–1097, 2021.

[97] R. Mishra and R. Winter, "Cold-and pressure-induced dissociation of protein aggregates and amyloid fibrils," *Angewandte Chemie International Edition*, vol. 47, no. 35, pp. 6518–6521, 2008.

[98] L. Ostermeier, G. A. de Oliveira, W. Dzwolak, J. L. Silva, and R. Winter, "Exploring the polymorphism, conformational dynamics and function of amyloidogenic peptides and proteins by temperature and pressure modulation," *Biophysical Chemistry*, vol. 268, p. 106506, 2021.

[99] J. an Gils, E. van Dijk, A. Peduzzo, A. Hofmann, N. Vettore, M. Schützmann, G. Groth, H. Mouhib, D. Otzen, A. Buell, and S. Abeln, "The hydrophobic effect characterises the thermodynamic signature of amyloid fibril growth," *Public Library of Science Computational Biology*, vol. 16, p. e1007767, 2020.

[100] S. Costantini, G. Colonna, and A. M. Facchiano, "Amino acid propensities for secondary structures are influenced by the protein structural class," *Biochemical and Biophysical Research Communications*, vol. 342, no. 2, pp. 441–451, 2006.

[101] S. Tsonchev, K. L. Niece, G. C. Schatz, M. A. Ratner, and S. I. Stupp, "Phase diagram for assembly of biologically-active peptide amphiphiles," *The Journal of Physical Chemistry B*, vol. 112, no. 2, pp. 441–447, 2008.

[102] Y. Hong, R. L. Legge, S. Zhang, and P. Chen, "Effect of amino acid sequence and ph on nanofiber formation of self-assembling peptides eak16-ii and eak16-iv," *Biomacromolecules*, vol. 4, no. 5, pp. 1433–1442, 2003.

[103] C. Narayanan and C. L. Dias, "Hydrophobic interactions and hydrogen bonds in β-sheet formation," *The Journal of Chemical Physics*, vol. 139, no. 11, p. 09B640_1, 2013.

[104] W. L. Jorgensen, "Interactions between amides in solution and the thermodynamics of weak binding," *Journal of the American Chemical Society*, vol. 111, no. 10, pp. 3770–3771, 1989.

[105] A. Abelein, J. Jarvet, A. Barth, A. Gräslund, and J. Danielsson, "Ionic strength modulation of the free energy landscape of aβ40 peptide fibril formation," *Journal of the American Chemical Society*, vol. 138, no. 21, pp. 6893–6902, 2016.

[106] A. Sharma, S. H. Behrens, Y. O. Chernoff, and A. S. Bommarius, "Modulation of the formation of aβ-and sup35nm-based amyloids by complex interplay of specific and nonspecific ion effects," *The Journal of Physical Chemistry B*, vol. 122, no. 19, pp. 4972–4981, 2018.

[107] K. Klement, K. Wieligmann, J. Meinhardt, P. Hortschansky, W. Richter, and M. Fändrich, "Effect of different salt ions on the propensity of aggregation and on the structure of alzheimer's aβ (1-40) amyloid fibrils," *Journal of Molecular Biology*, vol. 373, no. 5, pp. 1321–1333, 2007.

[108] F. Mahmoudinobar, J. M. Urban, Z. Su, B. L. Nilsson, and C. L. Dias, "Thermodynamic stability of polar and nonpolar amyloid fibrils," *Journal of Chemical Theory and Computation*, vol. 15, no. 6, pp. 3868–3874, 2019.

[109] B. P. Roland, R. Kodali, R. Mishra, and R. Wetzel, "A serendipitous survey of prediction algorithms for amyloidogenicity," *Peptide Science*, vol. 100, no. 6, pp. 780–789, 2013.

[110] T. D. Do, N. J. Economou, N. E. LaPointe, W. M. Kincannon, C. Bleiholder, S. C. Feinstein, D. B. Teplow, S. K. Buratto, and M. T. Bowers, "Factors that drive peptide assembly and fibril formation: experimental and theoretical analysis of sup35 nnqqny mutants," *The Journal of Physical Chemistry B*, vol. 117, no. 28, pp. 8436–8446, 2013.

[111] O. Conchillo-Solé, N. S. de Groot, F. X. Avilés, J. Vendrell, X. Daura, and S. Ventura, "Aggrescan: a server for the prediction and evaluation of" hot spots" of aggregation in polypeptides," *BioMed Central Bioinformatics*, vol. 8, no. 1, pp. 1–17, 2007.

[112] A. M. Fernandez-Escamilla, F. Rousseau, J. Schymkowitz, and L. Serrano, "Prediction of sequence-dependent and mutational effects on the aggregation of peptides and proteins," *Nature Biotechnology*, vol. 22, no. 10, pp. 1302–1306, 2004.

[113] P. H. Nguyen, A. Ramamoorthy, B. R. Sahoo, J. Zheng, P. Faller, J. E. Straub, L. Dominguez, J.-E. Shea, N. V. Dokholyan, A. De Simone *et al.*, "Amyloid oligomers: A joint experimental/computational perspective on alzheimer's disease, parkinson's disease, type ii diabetes, and amyotrophic lateral sclerosis," *Chemical Reviews*, vol. 121, no. 4, pp. 2545–2647, 2021.

[114] M. C. Owen, D. Gnutt, M. Gao, S. K. T. S. Wärmländer, J. Jarvet, A. Gräslund, R. Winter, S. Ebbinghaus, and B. Strodel, "Effects of in vivo conditions on amyloid aggregation," *Chemical Society Reviews*, vol. 48, no. 14, pp. 3946–3996, 2019.

[115] F. Chiti and C. M. Dobson, "Protein Misfolding, Functional Amyloid, and Human Disease," *Annual Review of Biochemistry*, vol. 75, no. 1, pp. 333–366, 2006.

[116] H. Hampel, J. Hardy, K. Blennow, C. Chen, G. Perry, S. H. Kim, V. L. Villemagne, P. Aisen, M. Vendruscolo, T. Iwatsubo, C. L. Masters, M. Cho, L. Lannfelt, J. L. Cummings, and A. Vergallo, "The Amyloid- Pathway in Alzheimer's Disease," *Molecular Psychiatry*, vol. 26, no. 10, pp. 5481–5503, 2021.

[117] S. I. A. Cohen, S. Linse, L. M. Luheshi, E. Hellstrand, D. A. White, L. Rajah, D. E. Otzen, M. Vendruscolo, C. M. Dobson, and T. P. J. Knowles, "Proliferation of amyloid-β42 aggregates occurs through a secondary nucleation mechanism," *Proceedings of the National Academy of Sciences*, vol. 110, no. 24, pp. 9758–9763, 2013.

[118] T. C. T. Michaels, A. Saric, S. Curk, K. Bernfur, P. Arosio, G. Meisl, A. J. Dear, S. I. A. Cohen, C. M. Dobson, M. Vendruscolo, S. Linse, and T. P. J. Knowles, "Dynamics of oligomer populations formed during the aggregation of Alzheimer's Aβ42 peptide," *Nature Chemistry*, vol. 12, no. 5, pp. 445–451, 2020.

[119] R. Wetzel, "Kinetics and Thermodynamics of Amyloid Fibril Assembly," *Accounts of Chemical Research*, vol. 39, no. 9, pp. 671–679, 2006.

[120] Y. Cao, X. Tang, M. Yuan, and W. Han, "Computational studies of protein aggregation mediated by amyloid: fibril elongation and secondary nucleation," *Progress in Molecular Biology and Translational Science*, vol. 170, pp. 461–504, 2020.

[121] I. M. Ilie and A. Caflisch, "Simulation Studies of Amyloidogenic Polypeptides and Their Aggregates," *Chemical Reviews*, vol. 119, no. 12, pp. 6956–6993, 2019.

[122] B. J. Williams-Noonan, A. Kamboukos, N. Todorova, and I. Yarovsky, "Self-assembling peptide biomaterials: Insights from spontaneous and enhanced sampling molecular dynamics simulations," *Chemical Physics Reviews*, vol. 4, no. 2, Jun. 2023.

[123] M. Törnquist, T. C. Michaels, K. Sanagavarapu, X. Yang, G. Meisl, S. I. Cohen, T. P. Knowles, and S. Linse, "Secondary nucleation in amyloid formation," *Chemical Communications*, vol. 54, no. 63, pp. 8667–8684, 2018.

[124] J. D. Schmit, "Kinetic theory of amyloid fibril templating," *The Journal of Chemical Physics*, vol. 138, no. 18, p. 185102, 2013.

[125] Z. Jia, J. D. Schmit, and J. Chen, "Amyloid assembly is dominated by misregistered kinetic traps on an unbiased energy landscape." *Proceedings of the National Academy of Sciences of the United States of America*, vol. 117, no. 19, pp. 10 322–10 328, May 2020.

[126] E. P. O'Brien, Y. Okamoto, J. E. Straub, B. R. Brooks, and D. Thirumalai, "Thermodynamic Perspective on the DockLock Growth Mechanism of Amyloid Fibrils," *The Journal of Physical Chemistry B*, vol. 113, no. 43, pp. 14 421–14 430, 2009.

[127] W. Han and K. Schulten, "Fibril elongation by aβ17-42: Kinetic network analysis of hybrid-resolution molecular dynamics simulations," *Journal of the American Chemical Society*, vol. 136, no. 35, pp. 12 450–12 460, 09 2014.

[128] N. Schwierz, C. V. Frost, P. L. Geissler, and M. Zacharias, "Dynamics of Seeded Aβ40-Fibril Growth from Atomistic Molecular Dynamics Simulations: Kinetic Trapping and Reduced Water Mobility in the Locking Step," *Journal of the American Chemical Society*, vol. 138, no. 2, pp. 527–539, 2016.

[129] S. Sasmal, N. Schwierz, and T. Head-Gordon, "Mechanism of nucleation and growth of Aβ40 fibrils from all-atom and coarse-grained simulations," *The Journal of Physical Chemistry B*, vol. 120, no. 47, pp. 12 088–12 097, Dec. 2016.

[130] Y.-W. Ma, T.-Y. Lin, and M.-Y. Tsai, "Fibril surface-dependent amyloid precursors revealed by coarse-grained molecular dynamics simulation," *Frontiers in Molecular Biosciences*, vol. 8, 2021.

[131] B. Barz and B. Strodel, "Understanding amyloid-β oligomerization at the molecular level: The role of the fibril surface," *Chemistry - A European Journal*, vol. 22, no. 26, pp. 8768–8772, 2016.

[132] J. S. Schreck and J.-M. Yuan, "A kinetic study of amyloid formation: Fibril growth and length distributions," *The Journal of Physical Chemistry B*, vol. 117, no. 21, pp. 6574–6583, 2013.

[133] T. C. T. Michaels, A. **v**Sarić, J. Habchi, S. Chia, G. Meisl, M. Vendruscolo, C. M. Dobson, and T. P. J. Knowles, "Chemical kinetics for bridging molecular mechanisms and macroscopic measurements of amyloid fibril formation," *Annual Review of Physical Chemistry*, vol. 69, no. 1, pp. 273–298, Apr. 2018.

[134] A. K. Buell, "The growth of amyloid fibrils: rates and mechanisms," *Biochemical Journal*, vol. 476, no. 19, pp. 2677–2703, 10 2019.

[135] A. V. Chechkin, I. M. Zaid, M. A. Lomholt, I. M. Sokolov, and R. Metzler, "Effective surface motion on a reactive cylinder of particles that perform intermittent bulk diffusion," *The Journal of Chemical Physics*, vol. 134, no. 20, p. 204116, 2011.

[136] A. V. Chechkin, I. M. Zaid, M. A. Lomholt, I. M. Sokolov, and Metzler, "Bulk-mediated diffusion on a planar surface: Full solution," *Physical Review E*, vol. 86, no. 4, p. 041101, 2012.

[137] O. G. Berg and C. Blomberg, "Association kinetics with coupled diffusional flows: Special application to the lac repressor-operator system," *Biophysical Chemistry*, vol. 4, no. 4, pp. 367–381, 1976.

[138] M. Bauer and R. Metzler, "Generalized facilitated diffusion model for dna-binding proteins with search and recognition states," *Biophysical Journal*, vol. 102, no. 10, pp. 2321–2330, 2012.

[139] D. Wang, S.-Y. Gou, and D. Axelrod, "Reaction rate enhancement by surface diffusion of adsorbates," *Biophysical Chemistry*, vol. 43, no. 2, pp. 117–137, 1992.

[140] Y. Xu, M. S. Safari, W. Ma, N. P. Schafer, P. G. Wolynes, and P. G. Vekilov, "Steady, symmetric, and reversible growth and dissolution of individual amyloid-β fibrils," *American Chemical Society Chemical Neuroscince*, vol. 10, no. 6, pp. 2967–2976, Jun. 2019.

[141] N. Rezaei-Ghaleh, G. Parigi, and M. Zweckstetter, "Reorientational dynamics of amyloid-β from NMR spin relaxation and molecular simulation," *Journal of Physical Chemistry Letters*, vol. 10, no. 12, pp. 3369–3375, Jun. 2019.

[142] S. Luca, W.-M. Yau, R. Leapman, and R. Tycko, "Peptide conformation and supramolecular organization in amylin fibrils: constraints from solid-state NMR," *Biochemistry*, vol. 46, no. 47, pp. 13 505–13 522, Nov. 2007.

[143] E. A. de Eulate, S. O'Sullivan, S. Fletcher, P. Newsholme, and D. W. M. Arrigan, "Ion-transfer electrochemistry of rat amylin at the water-organogel microinterface array and its selective detection in a protein mixture," *Chemistry: An Asian Journal*, vol. 8, no. 9, pp. 2096–2101, Sep. 2013.

[144] R. Kayed, "Common structure of soluble amyloid oligomers implies common mechanism of pathogenesis," *Science*, vol. 300, no. 5618, pp. 486–489, Apr 2003.

[145] C. Haass and D. J. Selkoe, "Soluble protein oligomers in neurodegeneration: lessons from the alzheimer's amyloid β-peptide," *Nature Reviews Molecular Cell Biology*, vol. 8, no. 2, pp. 101–112, Feb 2007.

[146] D. Ernst and J. Köhler, "Measuring a diffusion coefficient by single-particle tracking: statistical analysis of experimental mean squared displacement curves," *Physical Chemistry Chemical Physics*, vol. 15, no. 3, pp. 845–849, 2013.

[147] I. Poudyal and N. P. Adhikari, "Temperature dependence of diffusion coefficient of carbon monoxide in water: A molecular dynamics study," *Journal of Molecular Liquids*, vol. 194, pp. 77–84, 2014.

[148] S. I. A. Cohen, R. Cukalevski, T. C. T. Michaels, A. **v**Sarić, M. Törnquist, M. Vendruscolo, C. M. Dobson, A. K. Buell, T. P. J. Knowles, and S. Linse, "Distinct thermodynamic signatures of oligomer generation in the aggregation of the amyloid-β peptide," *Nature Chemistry*, vol. 10, no. 5, pp. 523–531, 2018.

[149] N. Rubin, E. Perugia, M. Goldschmidt, M. Fridkin, and L. Addadi, "Chirality of amyloid suprastructures," *Journal of the American Chemical Society*, vol. 130, no. 14, pp. 4602–4603, 2008.

[150] M. Kollmer, W. Close, L. Funk, J. Rasmussen, A. Bsoul, A. Schierhorn, M. Schmidt, C. J. Sigurdson, M. Jucker, and M. Fändrich, "Cryo-EM structure and polymorphism of Aβ amyloid fibrils purified from alzheimer's brain tissue," *Nature Communications*, vol. 10, no. 1, p. 4760, Oct. 2019.

[151] B. P. Tseng, W. P. Esler, C. B. Clish, E. R. Stimson, J. R. Ghilardi, H. V. Vinters, P. W. Mantyh, J. P. Lee, and J. E. Maggio, "Deposition of monomeric, not oligomeric, abeta mediates growth of alzheimer's disease amyloid plaques in human brain preparations," *Biochemistry*, vol. 38, no. 32, pp. 10 424–10 431, Aug. 1999.

[152] M. Hoshino, "Fibril formation from the amyloid-β peptide is governed by a dynamic equilibrium involving association and dissociation of the monomer," *Biophysical Reviews*, vol. 9, no. 1, pp. 9–16, Feb. 2017.

[153] Y. Xu, K. Knapp, K. N. Le, N. P. Schafer, M. S. Safari, A. Davtyan, P. G. Wolynes, and P. G. Vekilov, "Frustrated peptide chains at the fibril tip control the kinetics of growth of amyloid-β fibrils." *Proceedings of the National Academy of Sciences of the*, vol. 118, 2021.

[154] G. A. Somorjai and Y. Li, *Introduction to surface chemistry and catalysis*, 2nd ed. Hoboken, NJ, United States: Wiley-Blackwell, May 2010.

[155] Y. Kusumoto, A. Lomakin, D. B. Teplow, and G. B. Benedek, "Temperature dependence of amyloid β-protein fibrillization," *Proceedings of the National Academy of Sciences*, vol. 95, no. 21, pp. 12 277–12 282, 1998.

[156] S. I. Cohen, P. Arosio, J. Presto, F. R. Kurudenkandy, H. Biverstål, L. Dolfe, C. Dunning, X. Yang, B. Frohm, M. Vendruscolo *et al.*, "A molecular chaperone breaks the catalytic cycle that generates toxic aβ oligomers," *Nature Structural & Molecular Biology*, vol. 22, no. 3, pp. 207–213, 2015.

[157] A. Morriss-Andrews and J.-E. Shea, "Simulations of Protein Aggregation: Insights from Atomistic and Coarse-Grained Models," *The Journal of Physical Chemistry Letters*, vol. 5, no. 11, pp. 1899–1908, 2014.

[158] S. Linse, T. Scheidt, K. Bernfur, M. Vendruscolo, C. M. Dobson, S. I. A. Cohen, E. Sileikis, M. Lundqvist, F. Qian, T. O'Malley, T. Bussiere, P. H. Weinreb, C. K. Xu, G. Meisl, S. R. A. Devenish, T. P. J. Knowles, and O. Hansson, "Kinetic fingerprints differentiate the mechanisms of action of anti-A antibodies," *Nature Structural and Molecular Biology*, vol. 27, no. 12, pp. 1125–1133, 2020.

[159] M. I. Sulatsky, O. V. Stepanenko, O. V. Stepanenko, E. V. Mikhailova, I. M. Kuznetsova, K. K. Turoverov, and A. I. Sulatskaya, "Amyloid fibrils degradation: The pathway to recovery or aggravation of the disease?" *Frontiers in Molecular Biosciences*, vol. 10, 2023.

[160] B. Strodel, "Amyloid aggregation simulations: Challenges, advances and perspectives," *Current Opinion in Structural Biology*, vol. 67, pp. 145–152, 2021.

[161] B. J. Williams-Noonan, A. Kamboukos, N. Todorova, and I. Yarovsky, "Self-assembling peptide biomaterials: Insights from spontaneous and enhanced sampling molecular dynamics simulations," *Chemical Physics Reviews*, vol. 4, no. 2, p. 021304, 2023.

[162] S. Jalali, Y. Yang, F. Mahmoudinobar, S. M. Singh, B. L. Nilsson, and C. Dias, "Using all-atom simulations in explicit solvent to study aggregation of amphipathic peptides into amyloid-like fibrils," *Journal of Molecular Liquids*, vol. 347, p. 118283, 2022.

[163] M. Carballo-Pacheco and B. Strodel, "Advances in the Simulation of Protein Aggregation at the Atomistic Scale," *The Journal of Physical Chemistry B*, vol. 120, no. 12, pp. 2991–2999, 2016.

[164] S. Samantray, F. Yin, B. Kav, and B. Strodel, "Different Force Fields Give Rise to Different Amyloid Aggregation Pathways in Molecular Dynamics

Simulations," *Journal of Chemical Information and Modeling*, vol. 60, no. 12, pp. 6462–6475, 2020.

[165] R. Pellarin, E. Guarnera, and A. Caflisch, "Pathways and Intermediates of Amyloid Fibril Formation," *Journal of Molecular Biology*, vol. 374, no. 4, pp. 917–924, 2007.

[166] R. Pellarin and A. Caflisch, "Interpreting the Aggregation Kinetics of Amyloid Peptides," *Journal of Molecular Biology*, vol. 360, no. 4, pp. 882–892, 2006.

[167] W. Han and K. Schulten, "Fibril Elongation by Aβ17–42: Kinetic Network Analysis of Hybrid-Resolution Molecular Dynamics Simulations," *Journal of the American Chemical Society*, vol. 136, no. 35, pp. 12 450–12 460, 2014.

[168] T. Urbic, S. Najem, and C. L. Dias, "Thermodynamic properties of amyloid fibrils in equilibrium," *Biophysical Chemistry*, vol. 231, pp. 155–160, 2017.

[169] A. Saric, T. C. T. Michaels, A. Zaccone, T. P. J. Knowles, and D. Frenkel, "Kinetics of spontaneous filament nucleation via oligomers: Insights from theory and simulation," *The Journal of Chemical Physics*, vol. 145, no. 21, p. 211926, 2016.

[170] Y. Wang, S. J. Bunce, S. E. Radford, A. J. Wilson, S. Auer, and C. K. Hall, "Thermodynamic phase diagram of amyloid-β (16–22) peptide," *Proceedings of the National Academy of Sciences*, vol. 116, no. 6, pp. 2091–2096, 2019.

[171] S. J. Bunce, Y. Wang, K. L. Stewart, A. E. Ashcroft, S. E. Radford, C. K. Hall, and A. J. Wilson, "Molecular insights into the surface-catalyzed secondary nucleation of amyloid-β40 (Aβ40) by the peptide fragment Aβ16–22," *Science Advances*, vol. 5, no. 6, p. eaav8216, 2019.

[172] F. Mahmoudinobar, J. M. Urban, Z. Su, B. L. Nilsson, and C. L. Dias, "Thermodynamic Stability of Polar and Nonpolar Amyloid Fibrils," *Journal of Chemical Theory and Computation*, vol. 15, no. 6, pp. 3868–3874, 2019.

[173] Z. Su and C. L. Dias, "Driving β-Strands into Fibrils," *The Journal of Physical Chemistry B*, vol. 118, no. 37, pp. 10 830–10 836, 2014.

[174] C. Narayanan and C. L. Dias, "Hydrophobic interactions and hydrogen bonds in β-sheet formation," *The Journal of Chemical Physics*, vol. 139, no. 11, p. 115103, 2013.

[175] N. Schwierz, C. V. Frost, P. L. Geissler, and M. Zacharias, "From Aβ Filament to Fibril: Molecular Mechanism of Surface-Activated Secondary Nucleation from All-Atom MD Simulations," *The Journal of Physical Chemistry B*, vol. 121, no. 4, pp. 671–682, 2017.

[176] J. A. Lemkul and D. R. Bevan, "Assessing the Stability of Alzheimer's Amyloid Protofibrils Using Molecular Dynamics," *The Journal of Physical Chemistry B*, vol. 114, no. 4, pp. 1652–1660, 2010.

[177] X. Tang and W. Han, "Multiscale Exploration of Concentration-Dependent Amyloid-β(16-21) Amyloid Nucleation," *The Journal of Physical Chemistry Letters*, vol. 13, no. 22, pp. 5009–5016, 2022.

[178] B. Barz, Q. Liao, and B. Strodel, "Pathways of Amyloid-β Aggregation Depend on Oligomer Shape," *Journal of the American Chemical Society*, vol. 140, no. 1, pp. 319–327, 2018.

[179] S. L. Bernstein, N. F. Dupuis, N. D. Lazo, T. Wyttenbach, M. M. Condron, G. Bitan, D. B. Teplow, J.-E. Shea, B. T. Ruotolo, C. V. Robinson, and M. T. Bowers, "Amyloid-β protein oligomerization and the importance of tetramers and dodecamers in the aetiology of Alzheimer's disease," *Nature Chemistry*, vol. 1, no. 4, pp. 326–331, 2009.

[180] M. Törnquist, T. C. T. Michaels, K. Sanagavarapu, X. Yang, G. Meisl, S. I. A. Cohen, T. P. J. Knowles, and S. Linse, "Secondary nucleation in amyloid formation," *Chemical Communications*, vol. 54, no. 63, pp. 8667–8684, 2018.

[181] M. Yamazaki, K. Ikeda, T. Kameda, H. Nakao, and M. Nakano, "Kinetic Mechanism of Amyloid-β-(16–22) Peptide Fibrillation," *The Journal of Physical Chemistry Letters*, vol. 13, no. 26, pp. 6031–6036, 2022.

[182] L. J. Young, G. S. K. Schierle, and C. F. Kaminski, "Imaging A(1–42) fibril elongation reveals strongly polarised growth and growth incompetent states," *Physical Chemistry Chemical Physics*, vol. 19, no. 41, pp. 27 987–27 996, 2017.

[183] A. K. Buell, C. Galvagnion, R. Gaspar, E. Sparr, M. Vendruscolo, T. P. Knowles, S. Linse, and C. M. Dobson, "Solution conditions determine the relative importance of nucleation and growth processes in α-synuclein aggregation," *Proceedings of the National Academy of Sciences*, vol. 111, no. 21, pp. 7671–7676, 2014.

[184] W. Qiang, K. Kelley, and R. Tycko, "Polymorph-specific kinetics and thermodynamics of β-amyloid fibril growth," *Journal of the American Chemical Society*, vol. 135, no. 18, pp. 6860–6871, 2013.

[185] W. P. Esler, E. R. Stimson, J. M. Jennings, H. V. Vinters, J. R. Ghilardi, J. P. Lee, P. W. Mantyh, and J. E. Maggio, "Alzheimer's disease amyloid propagation by a template-dependent dock-lock mechanism," *Biochemistry*, vol. 39, no. 21, pp. 6288–6295, 2000.

[186] J. D. Schmit, "Kinetic theory of amyloid fibril templating," *The Journal of Chemical Physics*, vol. 138, no. 18, p. 185102, 2013.

[187] Z. Jia, J. D. Schmit, and J. Chen, "Amyloid assembly is dominated by misregistered kinetic traps on an unbiased energy landscape," *Proceedings of the National Academy of Sciences*, vol. 117, no. 19, pp. 10 322–10 328, 2020.

[188] F. Massi and J. E. Straub, "Energy landscape theory for alzheimer's amyloid β-peptide fibril elongation," *Proteins: Structure, Function, and Bioinformatics*, vol. 42, no. 2, pp. 217–229, 2001.

[189] J. E. Straub and D. Thirumalai, "Toward a molecular theory of early and late events in monomer to amyloid fibril formation," *Annual Review of Physical chemistry*, vol. 62, pp. 437–463, 2011.

[190] B. Barz and B. Strodel, "Understanding Amyloid-β Oligomerization at the Molecular Level: The Role of the Fibril Surface," *Chemistry – A European Journal*, vol. 22, no. 26, pp. 8768–8772, 2016.

[191] U. Sengupta, M. Carballo-Pacheco, and B. Strodel, "Automated markov state models for molecular dynamics simulations of aggregation and self-assembly," *The Journal of Chemical Physics*, vol. 150, no. 11, p. 115101, 2019.

[192] K. A. Dill, "Dominant forces in protein folding," *Biochemistry*, vol. 29, no. 31, pp. 7133–7155, 1990.

[193] W. Kauzmann, "Some factors in the interpretation of protein denaturation," N. L. Hjort, C. Holmes, P. Müller, and S. G. Walker, Eds. Elsevier, 1959, vol. 14, pp. 1–63.

[194] C. L. Dias, T. Ala-Nissila, J. Wong-ekkabut, I. Vattulainen, M. Grant, and M. Karttunen, "The hydrophobic effect and its role in cold denaturation," *Cryobiology*, vol. 60, no. 1, pp. 91–99, 2010.

[195] C. L. Dias, T. Hynninen, T. Ala-Nissila, A. S. Foster, and M. Karttunen, "Hydrophobicity within the three-dimensional Mercedes-Benz model: Potential of mean force," *The Journal of Chemical Physics*, vol. 134, no. 6, p. 065106, 2011.

[196] C. L. Dias, T. Ala-Nissila, M. Karttunen, I. Vattulainen, and M. Grant, "Microscopic Mechanism for Cold Denaturation," *Physical Review Letters*, vol. 100, no. 11, p. 118101, 2008.

[197] S. Jalali, Y. Yang, F. Mahmoudinobar, S. M. Singh, B. L. Nilsson, and C. Dias, "Using all-atom simulations in explicit solvent to study aggregation of amphipathic peptides into amyloid-like fibrils," *Journal of Molecular Liquids*, vol. 347, p. 118283, 2022.

[198] B. Strodel, "Amyloid aggregation simulations: Challenges, advances and perspectives," *Current Opinion in Structural Biology*, vol. 67, pp. 145–152, 2021.

[199] D. M. Marini, W. Hwang, D. A. Lauffenburger, S. Zhang, and R. D. Kamm, "Left-Handed Helical Ribbon Intermediates in the Self-Assembly of a β-Sheet Peptide," *Nano Letters*, vol. 2, no. 4, pp. 295–299, 2002.

[200] S. Zhang, D. M. Marini, W. Hwang, and S. Santoso, "Design of nanostructured biological materials through self-assembly of peptides and proteins," *Current Opinion in Chemical Biology*, vol. 6, no. 6, pp. 865–871, 2002.

[201] C. J. Bowerman, D. M. Ryan, D. A. Nissan, and B. L. Nilsson, "The effect of increasing hydrophobicity on the self-assembly of amphipathic β-sheet peptides," *Molecular BioSystems*, vol. 5, no. 9, pp. 1058–1069, 2009.

[202] C. J. Bowerman, W. Liyanage, A. J. Federation, and B. L. Nilsson, "Tuning β-Sheet Peptide Self-Assembly and Hydrogelation Behavior by Modification of Sequence Hydrophobicity and Aromaticity," *Biomacromolecules*, vol. 12, no. 7, pp. 2735–2745, 2011.

[203] F. Wang, O. Gnewou, S. Wang, T. Osinski, X. Zuo, E. H. Egelman, and V. P. Conticello, "Deterministic chaos in the self-assembly of β sheet nanotubes from an amphipathic oligopeptide," *Matter*, vol. 4, no. 10, pp. 3217–3231, 2021.

[204] M. J. Abraham, T. Murtola, R. Schulz, S. Páll, J. C. Smith, B. Hess, and E. Lindahl, "GROMACS: High performance molecular simulations through multi-level parallelism from laptops to supercomputers," *SoftwareX*, vol. 1–2, pp. 19–25, 2015.

[205] J. C. Sacchettini and J. W. Kelly, "Therapeutic strategies for human amyloid diseases," *Nature Reviews Drug Discovery*, vol. 1, no. 4, pp. 267–275, 2002.

[206] H. Hampel, J. Hardy, K. Blennow, C. Chen, G. Perry, S. H. Kim, V. L. Villemagne, P. Aisen, M. Vendruscolo, T. Iwatsubo *et al.*, "The amyloid-β pathway in alzheimer's disease," *Molecular Psychiatry*, vol. 26, no. 10, pp. 5481–5503, 2021.

[207] D. Thacker, K. Sanagavarapu, B. Frohm, G. Meisl, T. P. Knowles, and S. Linse, "The role of fibril structure and surface hydrophobicity in secondary nucleation of amyloid fibrils," *Proceedings of the National Academy of Sciences*, vol. 117, no. 41, pp. 25 272–25 283, 2020.

[208] P. Arosio, T. P. Knowles, and S. Linse, "On the lag phase in amyloid fibril formation," *Physical Chemistry Chemical Physics*, vol. 17, no. 12, pp. 7606–7618, 2015.

[209] C. J. Bowerman, W. Liyanage, A. J. Federation, and B. L. Nilsson, "Tuning β-sheet peptide self-assembly and hydrogelation behavior by modification of sequence hydrophobicity and aromaticity," *Biomacromolecules*, vol. 12, no. 7, pp. 2735–2745, 2011.

[210] I. M. Stanković, S. Niu, M. B. Hall, and S. D. Zarić, "Role of aromatic amino acids in amyloid self-assembly," *International Journal of Biological Macromolecules*, 2020.

[211] E. P. O'Brien, Y. Okamoto, J. E. Straub, B. R. Brooks, and D. Thirumalai, "Thermodynamic perspective on the dock- lock growth mechanism of amyloid fibrils," *The Journal of Physical Chemistry B*, vol. 113, no. 43, pp. 14 421–14 430, 2009.

[212] M. Bacci, J. Vymetal, M. Mihajlovic, A. Caflisch, and A. Vitalis, "Amyloid β fibril elongation by monomers involves disorder at the tip," *Journal of Chemical Theory and Computation*, vol. 13, no. 10, pp. 5117–5130, 2017.

[213] D. Bray, "Limits of computational biology," *In Silico Biology*, vol. 12, no. 1-2, pp. 1–7, 2012.

[214] M. Mompeán, R. Hervás, Y. Xu, T. H. Tran, C. Guarnaccia, E. Buratti, F. Baralle, L. Tong, M. Carrión-Vázquez, A. E. McDermott *et al.*, "Structural evidence of amyloid fibril formation in the putative aggregation domain of tdp-43," *The Journal of Physical Chemistry Letters*, vol. 6, no. 13, pp. 2608–2615, 2015.

[215] A. Srivastava and P. V. Balaji, "Molecular events during the early stages of aggregation of gnnqqny: An all atom md simulation study of randomly dispersed peptides," *Journal of Structural Biology*, vol. 192, no. 3, pp. 376–391, 2015.

[216] D. K. Klimov and D. Thirumalai, "Dissecting the assembly of aβ16–22 amyloid peptides into antiparallel β sheets," *Structure*, vol. 11, no. 3, pp. 295–307, 2003.

[217] S. Subedi, S. Sasidharan, N. Nag, P. Saudagar, and T. Tripathi, "Amyloid cross-seeding: Mechanism, implication, and inhibition," *Molecules*, vol. 27, no. 6, p. 1776, 2022.

[218] J. Stöhr, C. Condello, J. C. Watts, L. Bloch, A. Oehler, M. Nick, S. J. DeArmond, K. Giles, W. F. DeGrado, and S. B. Prusiner, "Distinct synthetic aβ prion strains producing different amyloid deposits in bigenic mice," *Proceedings of the National Academy of Sciences*, vol. 111, no. 28, pp. 10 329–10 334, 2014.

[219] K. Ono, R. Takahashi, T. Ikeda, and M. Yamada, "Cross-seeding effects of amyloid β-protein and α-synuclein," *Journal of Neurochemistry*, vol. 122, no. 5, pp. 883–890, 2012.

[220] C. Soto and S. Pritzkow, "Protein misfolding, aggregation, and conformational strains in neurodegenerative diseases," *Nature Neuroscience*, vol. 21, no. 10, pp. 1332–1340, 2018.